

1-1-2011

# Numerical and experimental investigations on vibration of simulated CANDU fuel bundles subjected to turbulent fluid flow

Xuan Zhang  
*Ryerson University*

Follow this and additional works at: <http://digitalcommons.ryerson.ca/dissertations>



Part of the [Mechanical Engineering Commons](#)

---

## Recommended Citation

Zhang, Xuan, "Numerical and experimental investigations on vibration of simulated CANDU fuel bundles subjected to turbulent fluid flow" (2011). *Theses and dissertations*. Paper 660.

NUMERICAL AND EXPERIMENTAL INVESTIGATIONS ON  
VIBRATION OF SIMULATED CANDU FUEL BUNDLES  
SUBJECTED TO TURBULENT FLUID FLOW

by

Xuan Zhang

Master of Applied Science

Beijing University of Technology, China, 2005

Bachelor of Engineering

Beijing University of Technology, China, 2002

A dissertation

presented to Ryerson University

in partial fulfillment of the

requirements for the degree of

Doctor of Philosophy

in the Program of

Mechanical Engineering

Toronto, Ontario, Canada, 2011

©Xuan Zhang 2011

*To my parents*

*for their endless love and care.*

*To Lan*

*for her inspiration and support.*

## **AUTHOR'S DECLARATION**

I hereby declare that I am the sole author of this thesis.

I authorize Ryerson University to lend this dissertation to other institutions or individuals for the purpose of scholarly research.

---

I further authorize Ryerson University to reproduce this dissertation by photocopying or by other means, in total or in part, at the request of other institutions or individuals for the purpose of scholarly research.

---

# NUMERICAL AND EXPERIMENTAL INVESTIGATIONS ON VIBRATION OF SIMULATED CANDU FUEL BUNDLES SUBJECTED TO TURBULENT FLUID FLOW

Xuan Zhang

Doctor of Philosophy, 2011

Program of Mechanical Engineering, Ryerson University

## **ABSTRACT**

Vibration of simulated CANDU fuel bundles induced by the coolant flow is investigated in this thesis through experiments and numerical simulations. Two simulated bundles and a hydraulic loop are built to mimic the situation of the fuel bundles located at the inlet of a fuel channel in a CANDU nuclear reactor. Fuel bundle vibration mechanism is investigated through experiments and numerical simulations. The three-dimensional turbulent flow that passes through the simulated bundles is modeled using the large eddy simulation (LES) and solved with parallel processing. The local cross flows induced by the presence of endplates at the inlet location and bundle interface location are investigated. The fluid forces are obtained as excitations for the fuel bundle vibration analysis. A finite element model of the fuel bundles is developed with the endplates modeled using the 3rd order thick plate theory. The response of the inlet fuel bundle to the fluid excitations is solved in the time and the frequency domain. The added mass and the fluid damping are approximated with the theory on the flow-induced vibration of slender bodies in a parallel flow. Measurements are obtained and used to validate the numerical prediction under various operating flow conditions.

## **ACKNOWLEDGEMENT**

I would like to express my sincere gratitude to my supervisor, Dr. Shudong Yu, for his invaluable guidance and patience throughout the course of my graduate study and this research. I would also like to thank other members of the dissertation committee, Dr. Seyed M. Hashem, Dr. David Naylor, Dr. Hua Lu, Dr. Don Oguamanam, Dr. Jeffrey Yokota, and Dr. Jean Zu for their efforts towards improving the quality of this dissertation. The financial support from NSERC, which made this dissertation possible, is gratefully acknowledged. Thanks are due to technical officers in the mechanical department, Andrew Heim and Joseph Amankrah, for their timely and patient support on the design and building of the experimental setup.

Further, I must express my sincere appreciation to my friends and colleagues, Alokendu Bhattacharya and Farzin Abbasian for their valuable discussions and suggestions on the flow simulation and experiments. Many thanks are due to Ravi Peri for sharing the load on the improvement of the experimental setup. Thanks are also due to Peter Bulski for providing advice on acoustic measurements and for dragging me to gym when it became necessary.

Last, but not least, I would express my deep gratitude towards my parents for their encouragement and support. Without their love, this achievement could not have been accomplished.

# TABLE OF CONTENTS

Author's Declaration.....	iii
Abstract.....	iv
Acknowledgement .....	v
Table of Contents.....	vi
List of Tables .....	ix
List of Figures.....	x
Nomenclature.....	xv
CHAPTER 1 Introduction.....	1
1.1 Background.....	1
1.1.1 CANDU Reactor and Fuel Bundles.....	1
1.1.2 Pressure Tube Fretting and Fuel Bundle Vibration .....	4
1.2 Objectives and Methodology of the Research .....	8
1.3 Literature Review.....	10
1.3.1 Flow-Induced Vibration of Fuel Bundles .....	10
1.3.2 Computational Fluid Dynamics and Fuel Flow Simulation .....	12
1.3.3 Wall Pressure Measurement .....	14
1.3.4 Structural Modeling of Fuel Bundles.....	15
CHAPTER 2 Flow Simulation and Experimental Validation.....	17
2.1 Large Eddy Simulation .....	17
2.1.1 Filtering.....	17
2.1.2 Filtered Navier-Stokes Equations .....	18
2.1.3 Spatial Discretization .....	20
2.1.4 Solution of the Time Marching Problem .....	23
2.2 Computational Model .....	24
2.2.1 Definitions.....	24
2.2.2 Flow Model Parameters .....	26
2.2.3 Grid Quality and Convergence .....	30
2.3 Simulation Results .....	34
2.3.1 Entrance Flow and Bundle Interface Flow .....	34

2.3.2	Flow Development.....	40
2.3.3	Fluid Forces .....	45
2.4	Experimental Validation .....	56
2.4.1	Experimental Setup.....	56
2.4.2	Wall Pressure Measurement for Pipe Flow .....	57
2.4.3	Wall Pressure Measurement for Bundle Flow .....	57
2.5	Summary of the Chapter .....	60
CHAPTER 3	Structural Model .....	61
3.1	Fuel Elements.....	61
3.2	Endplates.....	64
3.3	Joint of Beam Element and Plate Element.....	71
3.4	Fuel Bundle.....	74
3.5	Summary of the Chapter .....	77
CHAPTER 4	Vibration of the Inlet Bundle Subjected to Turbulent Flow .....	78
4.1	Experiments for the Fuel Bundle Vibration.....	78
4.1.1	Experimental Setup and Procedures .....	78
4.1.2	Free Vibration of the Inlet Bundle in Still Fluid.....	80
4.1.3	Vibration of the Inlet Bundle Induced by Flow .....	82
4.2	Solid-Fluid Interaction .....	84
4.2.1	Solid-Fluid Coupling .....	84
4.2.2	Added Mass, Added Stiffness and Fluid Damping.....	86
4.2.3	P-Delta Effect.....	90
4.2.4	Discretization of the Fluid Excitations .....	91
4.3	Equations of Motion .....	92
4.3.1	Equations of Motion .....	92
4.3.2	Modal Analysis.....	92
4.4	Solution Methods for Decoupled Equations.....	94
4.4.1	Response in Time Domain.....	94
4.4.2	Response in Frequency Domain .....	95
4.5	Numerical Results.....	98
4.5.1	Modal Excitations .....	98

4.5.2	Solution in Time Domain.....	99
4.5.3	Solution in Frequency Domain.....	102
4.5.4	Computer Code Efficiency.....	105
4.6	Summary of the Chapter.....	106
CHAPTER 5	Conclusions and Future Work.....	107
5.1	Conclusions.....	107
5.2	List of Contributions.....	109
5.3	Future Work.....	110
5.3.1	Limitations in the Current Work.....	110
5.3.2	Suggestions for Future Work.....	111
References	.....	113
Appendix	.....	121

## **LIST OF TABLES**

Table 2.1 Mesh parameters.

Table 2.2 Result inspection locations.

Table 2.3 Segment length.

Table 3.1 Endplate specification.

Table 3.2 Meshing parameters for two simulation endplates

Table 3.3 Load definition of the test cases.

Table 3.4 Geometric parameters and material properties of the bundle model

Table 3.5 Natural frequencies of the bundle.

Table 3.6 Validation on the current finite element model against ANSYS ED 8.0

Table 4.1 Damping factor for the first 20 modes.

## LIST OF FIGURES

Figure 1.1 Schematic diagram of the pressurized heavy water cooled version of a CANDU (CANada Deuterium-Uranium) nuclear reactor. (Courtesy to Emoscopes at <http://wikipedia.org>, published on 10 February 2006)

Figure 1.2 Classification of flow regions in a 12-bundle CANDU fuel channel.

Figure 1.3 Illustration of a CANFLEX 43-element fuel bundle.

Figure 1.4 Four fuel bundle designs: (a) Gentilly-1 bundle; (b) Pickering 28-element bundle; (c) Bruce 37-element bundle; (d) Gentilly-2 prototype bundle. (Courtesy to CANTEACH at <http://canteach.candu.org>)

Figure 1.5 The simulated bundle used in the current research.

Figure 2.1 A finite volume element.

Figure 2.2 Definition of the bundle components.

Figure 2.3 Definition of the flow channels: (a) endplate flow; (b) bundle flow.

Figure 2.4 The flow regions.

Figure 2.5 The axial discretization of the flow regions in the upstream pipe.

Figure 2.6 The axial discretization of the flow regions in a bundle and its endplates.

Figure 2.7 The cross-sectional discretization in a bundles and an endplates.

Figure 2.8 History of the residuals in the continuity equation (top) and the momentum equations (bottom) within a time step.

Figure 2.9 History of the residuals at the last iteration in each time step over 100 time steps.

Figure 2.10 In-plane velocity vectors (15x scale) at location L1 of the inlet bundle ( $t=0.16$  s).

Figure 2.11 Velocity magnitude contour in the Y-Z plane at the entrance ( $t=0.16$  s).

Figure 2.12 Velocity magnitude contour at location L1 of the inlet bundle ( $t=0.16$  s).

Figure 2.13 Static pressure contour at location L1 of the inlet bundle ( $t=0.16$  s).

Figure 2.14 . Pathlines behind the endplate rib in the BD2-1 subchannel in the inlet bundle at different moments: (a)  $t=0.16$  s; (b)  $t=0.20$  s; (c)  $t=0.24$  s; (d)  $t=0.28$  s.

Figure 2.15 In-plane velocity vectors (15x scale) at location L1 of the second bundle ( $t=0.16$  s).

Figure 2.16 Velocity magnitude contour in the Y-Z plane at the bundle interface( $t=0.16$  s).

Figure 2.17 In-plane velocity vectors (15x scale) at different locations in the inlet bundle ( $t=0.16$  s).

Figure 2.18 In-plane velocity vectors (15x scale) at different locations in the second bundle ( $t=0.16$  s).

Figure 2.19 X-velocity (left) and its Z-derivative (right) on the centerline of three subchannels ( $t=0.16$  s).

Figure 2.20 Y-velocity (left) and its Z-derivative (right) on the centerline of three subchannels ( $t=0.16$  s).

Figure 2.21 Z-velocity (left) and its Z-derivative (right) on the centerline of three subchannels ( $t=0.16$  s).

Figure 2.22 Static pressure on the centerline of three subchannels ( $t=0.16$  s).

Figure 2.23 Time history and PSD of the overall X-force on all fuel elements of the inlet bundle.

Figure 2.24 Time history and PSD of the overall Y-force on all fuel elements of the inlet bundle.

Figure 2.25 Distributed Y-force on all fuel elements of the inlet bundle.

Figure 2.26 Distributed Y-force on all fuel elements of the inlet bundle.

Figure 2.27 Time history and PSD of the overall Z-moment on all fuel elements of the inlet bundle.

Figure 2.28 Distributed Z-moment on all fuel elements of the inlet bundle.

Figure 2.29 Time history and PSD of distributed Z-moment on segment 1 on selected fuel elements of the inlet bundle.

Figure 2.30 Time history and PSD of distributed Z-moment on segment 5 on selected fuel elements of the inlet bundle.

Figure 2.31 Time history and PSD of distributed Z-moment on segment 10 on selected fuel elements of the inlet bundle.

Figure 2.32 Time history and PSD of the X-force on the upstream (left) and downstream (right) endplates of the inlet bundle.

Figure 2.33 Time history and PSD of the Y-force on the upstream (left) and downstream (right) endplates of the inlet bundle.

Figure 2.34 Time history and PSD of the Z-moment on the upstream (left) and downstream (right) endplates of the inlet bundle.

Figure 2.35 Experimental setup.

Figure 2.36 Wall pressure of the pipe flow without simulated bundle: (a) time domain signal; and (b) the smoothed normalized PSD.

Figure 2.37 Five measurements of wall pressure fluctuations and their PSDs.

Figure 2.38 Comparison of the smoothed wall pressure PSD between experiment and simulation.

Figure 3.1 The three-node Euler-Bernoulli beam element.

Figure 3.2 Front view of the endplate in the test fuel bundle.

Figure 3.3 Mesh of the endplate model using the nine-node thick plate element.

Figure 3.4 Node numbering schemes for the ring (a) and the rib (b).

Figure 3.5 Super-element of the endplate.

Figure 3.6 Endplate model discretized using Hexa20 elements.

Figure 3.7 Displacements at the nodes in the mid-plane of the intermediate ring at Radius=30 mm for load case 1.

Figure 3.8 Displacements at the nodes in the mid-plane of the intermediate ring at Radius=30 mm for load case 2.

Figure 3.9 Joint nodes on an endplate ring.

Figure 3.10 Finite element model of a simulated bundle.

Figure 3.11 Nodes and constrained locations on the bottom fuel elements.

Figure 3.12 Mode shapes for four modes.

Figure 4.1 Experimental setup for the flow-induced vibration of the inlet bundle.

Figure 4.2 Illustration of the sensor location.

Figure 4.3 Time history and PSD of the relative displacement between the sensor and the monitored fuel element in the free vibration without water.

Figure 4.4 Time history and PSD of the relative displacement between the sensor and the monitored fuel element in the free vibration within water.

Figure 4.5 Time history and PSD of the relative displacement between the sensor and the monitored fuel element obtained in the flow-induced vibration experiments.

Figure 4.6 Cylinder in parallel flow.

Figure 4.7 An element of a beam with distributed longitudinal force.

Figure 4.8 Discretized fluid forces on selected fuel elements.

Figure 4.9 Comparison of normalized modal forces between different modes.

Figure 4.10 Illustration on the sensor location.

Figure 4.11 Time history and power spectral density of the relative displacement between the sensor and the monitored fuel element obtained in simulation for 0.5 s record.

Figure 4.12 Time history and power spectral density of the relative displacement between the sensor and the monitored fuel element obtained in experiment for 0.5 s record.

Figure 4.13 Comparison of power spectral densities of the relative displacement obtained in simulation (left) and experiment (right) in logarithmic scale.

Figure 4.14 Phase plot of the  $x$ - (left) and  $y$ - (right) displacement of the monitored node.

Figure 4.15 Power spectral densities for  $x$ -displacement (left) and  $y$ -displacement (right) of the monitored node obtained from the random vibration solution.

Figure 4.16 Motion range of the monitored node with trajectory.

Figure 4.17 Scaled (200x) standard deviation of  $x$ - and  $y$ -displacement on selected fuel elements at the midplane.

## NOMENCLATURE

$A$	area or cross-sectional area
$\mathbf{A}_b$	rotation matrix
$A_c$	boundary of control volume
$A_f$	cross-sectional area of the bundle flow
$a_i$	state variable for displacement for the $i$ -the mode
$\mathbf{B}_i$	coefficient matrix for the $i$ -the mode
$\mathbf{b}_i$	coefficient vector for the $i$ -the mode
$b_i$	state variable for velocity for the $i$ -the mode
$C_D$	viscous drag coefficient in quiescent flow
$\mathbf{C}^i$	constraint matrix
$\mathbf{C}_e$	damping matrix of a finite element
$\tilde{\mathbf{C}}_e^i$	symmetric damping matrix of a finite element
$\mathbf{C}_e^i$	damping matrix of a finite element from inviscid force
$\mathbf{C}_e^v$	damping matrix of a finite element from viscous force
$\mathbf{C}_i$	damping matrix from inviscid force
$C_N$	viscous drag coefficients in the lateral direction
$\mathbf{C}_{sys}$	system damping matrix
$C_T$	viscous drag coefficients in longitudinal direction
$\hat{C}_{ij}$	cross stresses
$C_S$	Smagorinsky SGS model parameter
$\mathbf{C}_v$	damping matrix from viscous force
$c_d$	dimensionless viscous drag coefficient in quiescent flow
$c_i$	modal damping coefficient of the $i$ -th mode
$D$	cylinder diameter
$D_{ch}$	average subchannel diameter
$D_h$	hydraulic diameter
$D_p$	pipe inner diameter
$D_r$	average cylinder diameter
$d_i$	value of the $i$ -th peak
$d_m$	mesh size
$E$	Young's modulus
$F_A^y, F_A^z$	distributed inviscid lift force in $y$ - and $z$ -direction
$F_L$	distributed viscous drag force
$F_N^y, F_N^z$	distributed viscous lift force in $y$ - and $z$ -direction
$\mathbf{F}$	global force vector
$\mathbf{F}_n^e$	concentrated force vector
$f$	frequency
$f_D$	Darcy–Weisbach friction factor
$G$	shear modulus

<b>G</b>	system transfer function matrix
$G_i$	transfer function for the $i$ -th mode
$G_F$	the filter function
$\bar{\mathbf{H}}_c^i, \bar{\mathbf{H}}_c^v$	damping parameter matrix
$\mathbf{H}_m, \bar{\mathbf{H}}_m, \bar{\mathbf{H}}_m^a$	mass parameter matrix and its area integrated version
$\mathbf{H}_k, \bar{\mathbf{H}}_k, \bar{\mathbf{H}}_k^{ai}, \bar{\mathbf{H}}_k^{av}$	stiffness parameter matrix and its area integrated version
$\bar{\mathbf{H}}_k^p$	stiffness parameter matrix due to $p$ -delta effect
<b>I</b>	identity matrix
$J$	polar moment of area
<b>K</b>	stiffness matrix
$\tilde{\mathbf{K}}$	modal stiffness matrix
$\mathbf{K}_e$	stiffness matrix of a finite element
$\mathbf{K}_e^a$	added stiffness matrix of a finite element
$\tilde{\mathbf{K}}_e^a$	symmetric added stiffness matrix of a finite element
$\mathbf{K}_e^{ai}$	added stiffness matrix of a finite element from inviscid force
$\mathbf{K}_e^{av}$	added stiffness matrix of a finite element from viscous force
$\mathbf{K}_{ep}$	endplate stiffness matrix
$\mathbf{K}_f$	added stiffness matrix
$\mathbf{K}_{ii}, \mathbf{K}_{ij}, \mathbf{K}_{ji}, \mathbf{K}_{jj}$	partitions of the stiffness matrix
$\mathbf{K}_s$	stiffness matrix after eliminating constrained DOF
$\mathbf{K}_{sys}$	system stiffness matrix
$k_E$	equivalent stiffness
$k_i$	modal stiffness of the $i$ -th mode
$k_r = \tau_{ii}^R / 2$	residual kinetic energy
$L$	length of a fuel element
$L_e$	entrance length
$\hat{L}_{ij}$	Leonard stresses
$l$	characteristic length
$l_e$	element length
<b>M</b>	mass matrix
$\tilde{\mathbf{M}}$	modal mass matrix
$\mathbf{M}_e$	mass matrix of a finite element
$\mathbf{M}_e^a$	added mass matrix of a finite element
$\mathbf{M}_f$	added mass matrix
$\mathbf{M}_s$	mass matrix after eliminating constrained DOF
$\mathbf{M}_{sys}$	system mass matrix
$M_y, M_z$	moment in $y$ - and $z$ -direction
$m_i$	modal mass of the $i$ -th mode
<b>N</b>	shape function
$N_m$	total number of modes retained in a modal analysis

$N_{elem}$	total number of beam elements
$N_{ep}$	total number of endplate super-elements
$N_y$	shape function for displacement $v$
$\mathbf{n}$	normal of a surface
$P$	longitudinal force
$P_c$	normal contact force
$P_i$	normalized modal force of the $i$ -th mode
$P_{wet}$	wetted perimeter
$p$	static pressure
$p^*$	guessed pressure
$\tilde{p}$	pressure deviation
$\bar{p}$	filtered static pressure
$\bar{p}_m$	discretized filtered static pressure
$\mathbf{Q}$	modal force vector
$Q_i$	modal force of the $i$ -th mode
$\mathbf{q}$	total nodal variables in the global coordinates
$\mathbf{q}_e$	beam element nodal variables in the global coordinates
$\mathbf{q}_{ep}$	endplate superelement interface variables
$q_e$	angle of an equiangular grid cell
$q_{max}$	maximum angle in an grid cell
$q_{min}$	minimum angle in an grid cell
Re	Reynolds number
$Re_x$	Reynolds number for boundary layer development
$\hat{R}_{ij}$	SGS Reynolds stresses
$R_{ij}$	crosscorrelation function between modal force of the $i$ -th mode and the $j$ -th mode
$r$	contact point radius
$\mathbf{r}^i$	position vector
$\bar{S}_{ij}$	filtered rate of strain
$S_{ij}^P$	cross spectral density between the $i$ -th and $j$ -th mode
$\mathbf{S}_P$	spectral density matrix of the normalized modal force
$S_t$	Strouhal number
$\mathbf{S}_u$	response spectral density matrix
$\mathbf{S}_\eta$	modal response spectral density matrix
$S_{\eta i}$	modal response spectral density for the $i$ -th mode
$\mathbf{T}$	coordinate transform matrix
$T$	total kinetic energy
$T_e$	kinetic energy of a finite element
$t$	time
$U$	mean flow velocity in the bundle
$U_c$	eddy convective velocity
$U_x, U_y, U_z$	$x$ -, $y$ - and $z$ -displacement in the mid-plane of an endplate
$u, u_o, u_{oi}, u^i$	displacement in $x$ -direction

$\tilde{u}$	turbulent velocity
$\mathbf{u}$	displacement vector
$\bar{\mathbf{u}}$	nodal displacement vector in the element coordinates
$u_c$	critical dimensionless velocity
$u_i$	flow velocity components ( $i=1,2,3$ )
$\bar{\mathbf{u}}_i$	nodal displacement vector of node $i$
$\bar{u}_i$	filtered flow velocity components ( $i=1,2,3$ )
$\mathcal{V}$	potential energy
$V$	volume
$V_c$	control volume
$V_e$	potential energy of a finite element
$v, v_o, v_{oi}, v^i$	displacement in $y$ -direction
$\bar{\mathbf{v}}$	filtered velocity vector
$\bar{\mathbf{v}}^*$	guessed filtered velocity field
$\bar{\mathbf{v}}^{\sim}$	filtered velocity deviation
$\bar{\mathbf{v}}_m, \bar{\mathbf{v}}_M, \bar{\mathbf{v}}_N$	discretized filtered velocity vector
$\bar{v}_s$	nodal displacement in $y$ -direction
$W$	work
$w, w_o, w_{oi}, w^i$	displacement in $z$ -direction
$\mathbf{x}, \mathbf{x}_E^{(b)}, \mathbf{x}^{(e)}$	distance vector
$y^+$	dimensionless wall distance
$\mathbf{y}_i$	state variable vector for the $i$ -the mode
$\alpha_p$ and $\alpha_i$	relaxation factors
$\gamma$	filter parameter
$\Delta$	filter size
$\Delta p$	pressure drop
$\Delta t$	time step size
$\Delta V$	discretized volume
$\delta$	boundary layer thickness
$\delta_j$	intermediate value to calculate $\zeta$ from measurement
$\delta W$	virtual work
$\zeta$	damping factor
$\zeta_i$	damping factor of the $i$ -th mode
$\eta$	turbulent length scale
$\eta_i$	modal coordinate of the $i$ -th mode
$\theta_x, \theta_y, \theta_z$	rotation angle in $x$ -, $y$ - and $z$ -direction
$\theta_{xi}, \theta_{yi}, \theta_{zi}$	rotation angle in $x$ -, $y$ - and $z$ -direction of node $i$
$\nu$	kinematic viscosity
$\nu_r$	eddy viscosity
$\xi$	local coordinate in a finite element
$\rho$	fluid density
$\rho_s$	structural material density
$\varsigma$	dummy integration variable
$\sigma_x, \sigma_y$	standard deviation of response in $x$ - and $y$ -direction

$\sigma_r$	standard deviation of relative distance
$\sigma_{\eta i}^2$	modal response variance of the $i$ -th mode
$\tau$	residual stress tensor
$\tau$	turbulent time scale
$\tau_{ij}$	residual-stress tensor ( $i=1,2,3$ )
$\tau_{ij}^r$	anisotropic residual stress tensor
$\nu$	Poisson's ratio
$\Phi$	mode shape matrix
$\phi$	scalar function
$\bar{\phi}$	filtered scalar function
$\phi_i$	modal vector of the $i$ -th mode
$\phi_x^i, \phi_y^i$	rotation at node $i$ in an thick plate element
$\chi$	added mass coefficient
$\Psi_i$	state transition matrix for the $i$ -th mode
$\omega$	angular velocity
$\omega_i$	natural frequency of the $i$ -th mode

#### Superscripts

*	guessed value
$t$	value at time step $t$

#### Subscripts

$i$	$i$ -th
$j$	$i$ -th
$m$	point $m$
$M$	point $M$
$N$	point $N$

#### Symbols

$\nabla \cdot a$	divergence of quantity $a$
$\nabla a$	gradient of quantity $a$
$\dot{a}$	first derivative of quantity $a$ with respect to time
$\ddot{a}$	second derivative of quantity $a$ with respect to time
$a'$	first derivative of quantity $a$ with respect to $\xi$
$a''$	second derivative of quantity $a$ with respect to $\xi$
$a^T$	transpose of quantity $a$

## CHAPTER 1 INTRODUCTION

This chapter gives an introduction to the flow-induced vibration of nuclear fuel bundles. The background information of the application and the significance of the proposed research are given in Section 1.1. The objectives and the methodology are described in Section 1.2. A literature study is given in Section 1.3.

### 1.1 Background

#### 1.1.1 CANDU Reactor and Fuel Bundles

CANDU<sup>®</sup> (CANada Deuterium Uranium) reactor is a pressurized heavy water reactor for electricity generation designed by Atomic Energy of Canada Ltd (AECL). A CANDU reactor unit consists of 13 sub-systems, as illustrated in Figure 1.1.

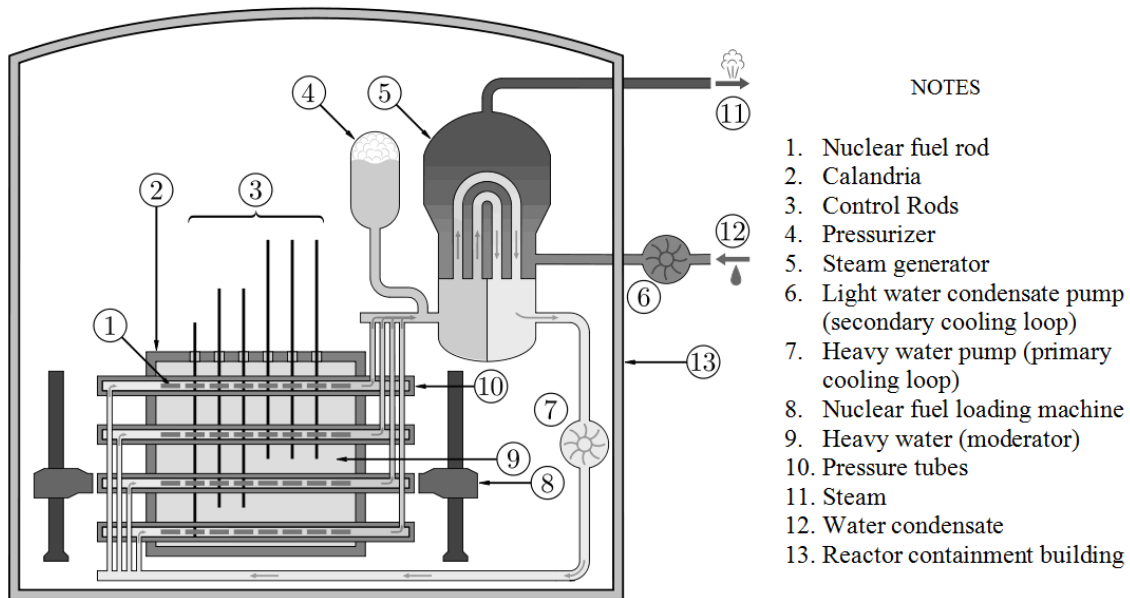


Figure 1.1 Schematic diagram of the pressurized heavy water cooled version of a CANDU (CANada Deuterium-Uranium) nuclear reactor. (Courtesy to Emoscopes at <http://wikipedia.org>, published on 10 February 2006)

<sup>®</sup> A registered trade mark of Atomic Energy of Canada Ltd (AECL).

Pressurized coolant (deuterium, or heavy water) is injected into the pressure tubes to bring out the heat generated by the fuel bundles. A pressure tube contains 12 or 13 horizontal fuel bundles. Shield plugs are installed at the downstream of the bundle string to hold all bundles at their designed positions. The flow that passes through the fuel string can be classified into four types according to the flow channel geometry: upstream pipe flow, flow passing endplates, flow inside bundle, and downstream pipe flow, as shown in Figure 1.2.

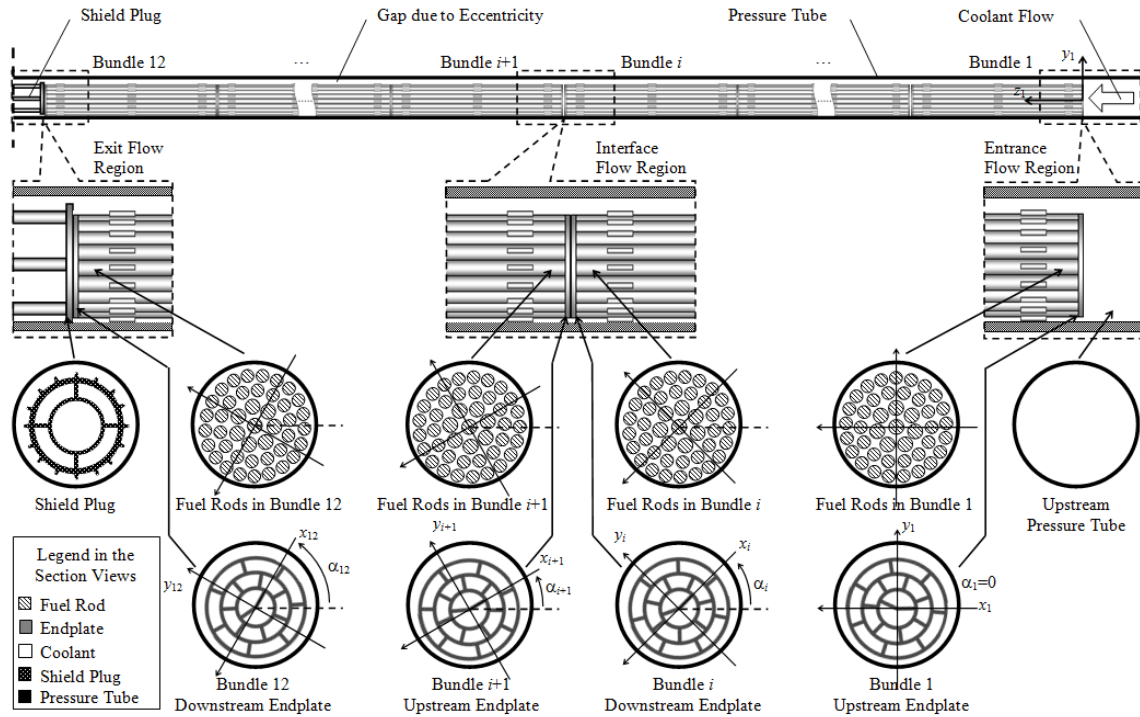


Figure 1.2 Classification of flow regions in a 12-bundle CANDU fuel channel.

A CANDU fuel bundle is designed to have a number of heat-generation fuel elements radially and circumferentially spaced in a few concentric rings. The fuel elements are welded to an endplate at each end. The two endplates hold the fuel elements and make the fuel bundle an integral structure. Bearing pads are welded onto the outermost ring of fuel elements to maintain a radial gap between a fuel bundle and the pressure tube, as shown in Figure 1.3. There are numerous designs of the fuel bundle. Figure 1.4 shows four types of fuel bundles. The fuel bundle design currently used in the main nuclear generating sites in Canada is the 37-element bundle as shown in Figure 1.4 (c), which consists of 37 fuel elements. Endplates are used to connect the fuel elements at both ends.

Each fuel element contains a number of fuel pellets made of natural uranium in the form of ceramic uranium-dioxide. Recently a new fuel bundle design, CANFLEX (CANDU FLEXible fuelling), was released, which contains 43 fuel elements, as shown in Figure 1.3. The newly designed bundles will be installed in two fuel channels in the Bruce NGS B reactors located in Ontario, Canada, as part of the planned Demonstration Irradiation Program, according to the announcement on the AECL website (<http://www.aecl.ca>).

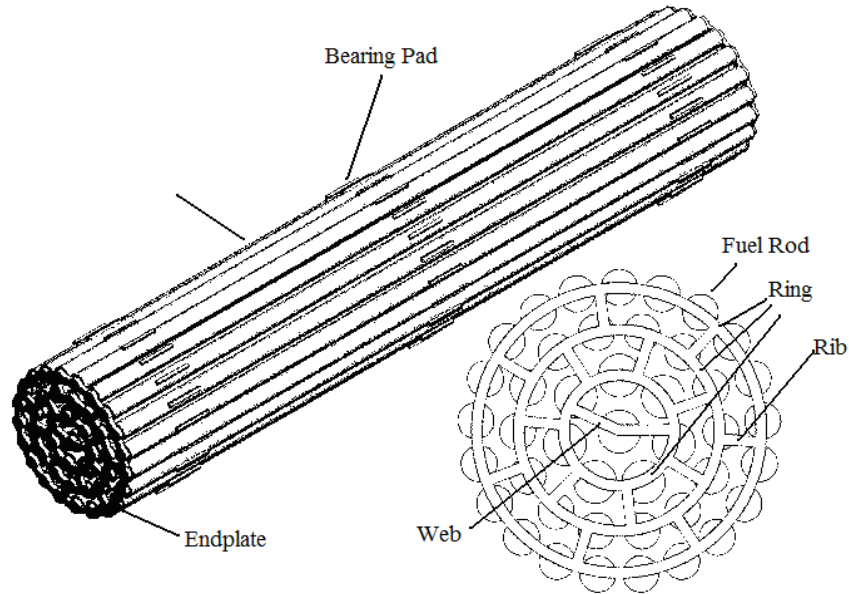


Figure 1.3 Illustration of a CANFLEX 43-element fuel bundle.

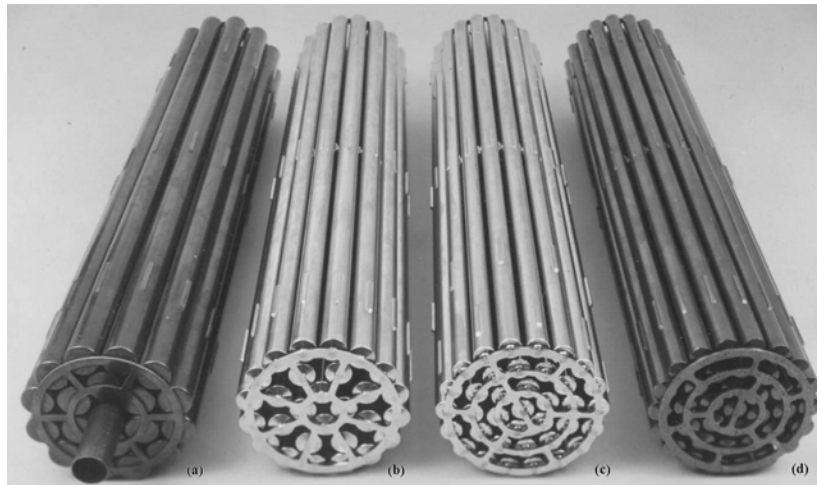


Figure 1.4 Four fuel bundle designs: (a) Gentilly-1 bundle; (b) Pickering 28-element bundle; (c) Bruce 37-element bundle; (d) Gentilly-2 prototype bundle. (Courtesy to CANTEACH at <http://canteach.candu.org>)

The simulated fuel bundles used in simulation and experiment in the current research are different from the actual bundles. The simulated bundle mimics the geometry of a 43-element CANFLEX bundle by including fuel elements, endplates and bearing pads, as shown in Figure 1.5. The fuel elements are solid circular beams made from stainless steel.

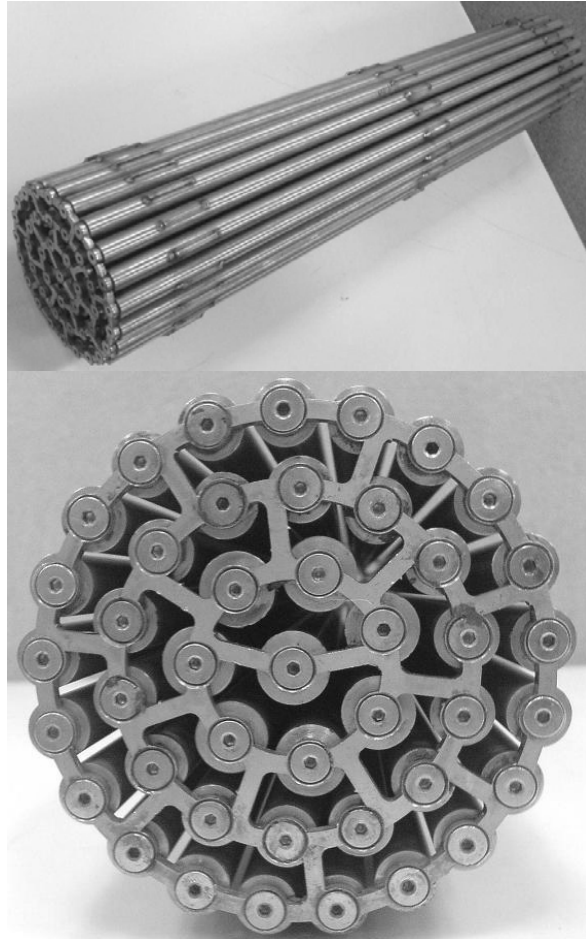


Figure 1.5 The simulated bundle used in the current research.

### *1.1.2 Pressure Tube Fretting and Fuel Bundle Vibration*

Flow-induced vibration of fuel bundles is an unavoidable phenomenon in the fuel channels since rapid coolant flow is always present. Vibration of the fuel bundles leads to impact and rubbing between the bearing pads and the pressure tube, which causes material removal from the pressure tubes. This is known as the fretting wear of the pressure tube. Although the vibration amplitude is small and the material removal rate is low, the pressure tubes are designed to serve for a very long period of time, e.g. 20 – 25 years, and the accumulated wear damage can be significant.

Inspections of the spent fuel bundles and the pressure tubes in Darlington and Bruce reactors showed that wearing of material on both the pressure tube and the fuel bundle happened commonly in all units (Norsworthy *et al.*, 1994). Fretting marks on the pressure tube were characterized and summarized (Judah, 1992; Norsworthy and Ditschun, 1995; Dennier *et al.*, 1995) as: i) fretting was worst on the inlet bundle and the severity decays quickly in the downstream; ii) the frets reached a depth limit of 0.3 mm in less than 70 days, which was considered a short period of time compared to the service life of pressure tube; iii) the fretting marks were caused by the bending of the fuel elements as well as the gross motion of the bundle, e.g. rocking. Severe damages in a few particular fuel channels were found and attributed to acoustic resonance between the fuel channel acoustic natural frequency and the pressure pulsation produced by the 5-vane primary pumps (Misra *et al.*, 1994), but intermediate and mild damages were found in the majority of fuel channels, which could not be explained by acoustic resonance. After the primary pumps were replaced by a 7-vane design, the acoustic resonance issue was solved, but this improvement did not apparently reduce the fretting wear that happened in the majority of the channels (Judah, 1992). The major cause of intermediate and mild level fretting wear was attributed to flow-induced vibration.

Looking from the structural point of view, the fuel bundles are prone to vibrate. The fuel elements are flexible slender structures loosely supported at both ends. They dwell on the bottom of the pressure tube near the 6 o'clock position. There is only a small number of bearing pads contacting with the pressure tube due to support the fuel bundles. The contact constraints on the bearing pads do not restrict the bundle from sliding or rolling. The bundle is also capable of vibrating vertically as a mass-spring system. These motions all contribute to the gross motion of the fuel bundles. These motions can be excited by the coolant flow under the preferred conditions.

It is obvious that the turbulent flow plays a significant role in producing excitations for the fuel bundle vibration. The average mass flow rate of the coolant is about 26 kg/s in normal operation. This flow carries tremendous kinetic energy. The energy is transferred to the bundles by the fluctuating form drag and the viscous force on the surfaces of the

fuel elements and endplates. However, the flow-induced vibration mechanism of the fuel bundles is not well understood in the following aspects:

- The excitation mechanism is not known. Possible cause of structural vibration induced by a flow can be classified into three categories: fluid-elastic instability, vortex shedding, and turbulent buffeting. It has been realized that the fluidelastic instability of slender structures in parallel flow is not a concern, since the nondimensionalized mean flow velocity in the bundle is far less than the critical value for instability to occur (Paidoussis, 2004). This is confirmed by the author through experiments (Zhang and Yu, 2008). Turbulence in parallel flows inside the bundle was regarded as the cause of vibration in the past; however it was proven that turbulence in the fully developed flow in a fuel bundle was insufficient to excite an individual fuel element to vibrate at the level that leads to the pressure tube fretting marks observed in the Darlington and Bruce reactors (Yetisir and Fisher, 1997). This indicates that an unknown stronger source of excitation must exist in the bundle flow. Vortex shedding happens in flow passing across a structure and is known to cause high level vibration of the structure when the vibration frequency coincides with the frequency of vortices shed from the structure. The flow inside the fuel bundle is largely parallel flow; however, local cross-flow happens at the endplates due to the presence of ribs and rings. The importance of this local cross-flow remains unknown.
- The bundle flow has not been solved. The lack of understanding of the fluid excitation mechanism is mainly due to insufficient knowledge of the bundle flow. Experimental investigations of bundle flows are very difficult due to the complex geometry and limited space. Analytical solution, even greatly simplified as potential flow, can hardly be obtained due to the presence of endplate. Computer simulation is a powerful tool for investigating fluid flow that experiments face difficulty, but the accuracy of modeling turbulence and the practical solution of large scale models were not achievable until large eddy simulation and parallel processing were combined and applied to fuel bundle flows recently (Abbasian *et al.*, 2009). Still,

there is a lack of a fluid model that covers the flow in multiple bundles. No information of the fluid force distribution on a fuel bundle was published.

- No structural dynamic model of fuel bundles has been developed. Studies of fuel bundle vibration are mainly conducted experimentally or based on simplified model of isolated beams. One of the major difficulties of modeling the fuel bundle is the endplate. Conventional plate theory leads to large error due to the large thickness-to-width ratio. Beam theory cannot handle the material overlapping between the rings and the ribs/webs. A proper endplate model needs to be developed for the fuel bundles.

## 1.2 Objectives and Methodology of the Research

The main objectives of the research reported in this thesis are:

1. To develop an accurate fluid model for the flow passing through a string of fuel bundles capable of capturing the dynamic properties of the flow;
2. To investigate the excitation mechanism of the fuel bundle vibration subjected to the coolant flow and obtain the fluid force acting on the fuel bundle;
3. To develop a reliable dynamic model for the fuel bundles, including an accurate and efficient endplate plate model;
4. To predict the fuel bundle vibration under the normal operating condition of the coolant flow and compare with experiments.

The current research aims at understanding the mechanism of the flow-induced vibration of the fuel bundles. The emphasis is put on the inlet bundle since the entrance flow is considered a significant source of unsteady force due to the abrupt change of the flow channel. Due to the fact that the displacement of the bundle is small (Zhang and Yu, 2008), the change of geometric configuration can be ignored. The vibration velocity is also significantly small compared to the mean flow velocity and the average turbulent velocity fluctuation estimated using the  $k$ - $\epsilon$  turbulent model (Tennekes and Lumley, 1972). Therefore, the structural vibration does not greatly affect the fluid flow, and the fluid solution can be decoupled from the structural response; however the structure response is greatly affected by the surrounding flow in the form of excitation, added mass, fluid damping and added stiffness. This one-way coupling between solid and fluid allows the above objectives to be achieved with the following strategy:

Firstly, the incompressible turbulent flow that enters and passes through an inlet 43-element simulated bundle and a half of the successive bundle is numerically solved using large eddy simulation and validated against out-reactor measurements. The fluid force distributed on the fuel bundle is obtained.

Secondly, the structural modeling of the fuel bundle is done using the finite element method. Higher order beam element and thick plate element is used to discretize the fuel elements and the endplates respectively.

Finally, the flow-induced vibration model of the inlet bundle is established by combining the structural model, the fluid excitation, and the added mass, added damping and added stiffness approximated from the slender body theory Chen (1975), Blevins (1977) and Paidoussis (2004). Bundle vibration is predicted using this model and compared to out-reactor measurements.

## 1.3 Literature Review

### 1.3.1 Flow-Induced Vibration of Fuel Bundles

Flow-induced vibration is usually related to three mechanisms. They are fluid-elastic instability, vortex shedding, and turbulent buffeting. For the vibration of fuel elements or fuel bundles in CANDU reactors, most researches conducted to date focused on the vibration induced by fluid-elastic instability and turbulence in parallel flows.

Fluid-elastic instability is the excitation mechanism with greatest potential to cause damage in a short period of time. A characteristic of the fluid-elastic instability is the presence of a critical velocity. When the flow velocity is lower than the critical velocity, the structure vibrates in very low amplitude which is mainly due to the turbulence and other weak excitations in the flow; when the flow velocity reaches and exceeds the critical velocity, the vibration amplitude increases dramatically and exhibits a high amplitude periodic motion with strong coupling between the solid and the fluid. For a beam in parallel flow, slender body theory (Lighthill, 1960; Karamcheti, 1966; Blevins, 1993) was used to obtain the fluid forces induced by the beam motion in a simplified potential flow. These forces were applied back to the beam in the form of added mass, fluid damping and extra stiffening terms. Viscous forces were superposed to the beam in virtue of the small motion and high Reynolds number. A model of the flow-induced vibration of a beam in parallel flow given by Paidoussis (1966) revealed that the fluid-elastic instability would occur for beams with supported ends. A dimensionless velocity was derived as  $u = UL\sqrt{\rho A/EI}$ , where  $L$ ,  $A$ ,  $E$ , and  $I$  are the length, the cross-sectional area, the Young's modulus and the cross-sectional moment of inertia of a fuel element;  $\rho$  is the fluid density;  $U$  is the mean flow velocity. Divergence in the first beam bending mode would occur when the dimensionless velocity exceeded 3.5. The study was later extended to multiple cylinders and fuel bundles. Chen (Chen and Wambsganss, 1972; Chen, 1975) developed analytical models for a cluster of cylinders in axial flow. The fluid coupling terms in the added mass was derived. Paidoussis and Suss (1977) developed a simplified model with inviscid and viscous inter-cylinder coupling and studied the fluidelastic instability problem. Paidoussis *et al.* (1983) investigated flexibly

interconnected cylinders in axial flow. Lin (1987) developed an analytical model to include the inertia and viscous coupling effects for arbitrary number of cylinders based on the Navier-Stokes equations for viscous and incompressible flow. The state of the art in parallel-flow-induced vibration and instability can be found in the book written by Paidoussis (2004).

Turbulence-induced fuel vibration received more attention since the flow velocity in the fuel bundle was usually subcritical. Compared to fluid-elastic instability, turbulence causes much smaller amplitude of vibration. However, turbulence-induced vibration is inevitable as long as the bundle flow exists. In fact, turbulence is often promoted in the fuel channels to facilitate heat exchange between the fuel and the coolant. The turbulence-induced vibration is usually sufficiently small and does not affect the flow; therefore the solid-fluid coupling is weak and the response is linear to the excitation force. Random vibration response of a fuel element in a turbulent parallel two-phase flow was modeled by Gorman (1971) with the measured statistical properties of the two-dimensional pressure field surrounding the fuel element. Yetisir and Fisher (1997) presented a similar model for an individual CANDU fuel element in a turbulent flow that represents the typical fully developed flow inside a fuel bundle. They found that turbulence cannot excite the fuel element vibration to the level that can produce the observed fretting marks. Paidoussis and Curling (1985) developed an analytical model for vibrations of a cluster of cylinders in turbulent parallel flow, and later the turbulent wall pressure was characterized experimentally (Curling and Paidoussis, 1992). In the experimental aspect, Au-Yang and Jordan (1980) measured the wall-pressure fluctuation around a fuel element in a laboratory reactor and a commercial reactor. D'Arcy and Schenk (1987) measured the axial velocity, turbulence and wall shear stress variation in a few subchannels in a 37-element CANDU 6 bundle. Pettigrew (1993) provided a comprehensive experimental investigation of flow-induced vibrations of nuclear fuel bundles under in-reactor conditions. He observed small amplitude vibration of fuel elements under the normal operating conditions in a research reactor. The vibration amplitude was generally less than 10  $\mu\text{m}$  root-mean-square (RMS). The predominant frequency varies between 35 to 65 Hz depending on the power. It was found that the predominant frequency increased dramatically with power due to the stiffening effect

induced by the thermal expansion of the fuel pellets. Besides power, the effect of other parameters, such as flow velocity and steam quality in two-phase flow, was also studied, but the excitation mechanism was not clearly explained. Smith and Derken (1998) measured the overall unsteady forces acting on a CANDU 6 inlet bundle. The investigation indicated that the bundle vibration mode was a mixture of rolling and bending motion, and the most concerned frequencies were those less than 30 Hz and characterized by almost rigid-body motion, including a low frequency motion as the bundle rocking from side to side in the pressure tube.

Vortex shedding is another mechanism that induces high level of vibration. The frequency of vortices shed from a structure is determined by the flow velocity, the characteristic length of the structure and a dimensionless coefficient, Strouhal number. The Strouhal number is defined as  $S_t = fl/U$ , where  $f$  is the vortex shedding frequency;  $l$  is the characteristic length; and  $U$  is the mean flow velocity. The value of the Strouhal number must be determined experimentally. When the shedding frequency is close to one of the structural natural frequencies, the shedding frequency is locked in the structural natural frequency, and the resonance between them induces high level amplitude vibration. Vibration induced by vortex shedding is a common phenomenon in heat exchanger where cross-flow is predominant. This phenomenon has been extensively studied by many researchers, such as Blevins (1993), Pettigrew (1993) and Weaver *et al.* (2000). The fuel bundle flow was always regarded as parallel flow; however, the endplate creates local cross-flows at the entrance of the inlet bundle and the interface between adjacent bundles. Unfortunately, no research has been done so far considering these cross-flows and their roles in causing the fuel bundle vibration.

### *1.3.2 Computational Fluid Dynamics and Fuel Flow Simulation*

In the traditional methods used in fuel bundle flow-induced vibration analysis, the flow was greatly simplified due to the difficulty for handling the true flow. The simplification is based on simple geometry of the flow channel and the immersed body. Entrance flow and flow near the endplates can hardly be handled in the same way. With the progress in computational fluid dynamics (CFD) and computer technology, large scale numerical solution for bundle flow is now possible. This brings about two benefits: i) the true three-

dimensional turbulent flow around the fuel elements, including the boundary layer, can be solved; ii) complex geometries can be handled. To obtain an accurate solution for the unsteady three-dimensional flow that enters and passes through the inlet bundle, a proper numerical turbulent model needs to be adopted.

A huge amount of literature was dedicated to CFD of turbulent flow. Excellent reviews and studies of turbulence theory were given by Tennekes and Lumley (1972) and Pope (2000). Discretization of the fluid governing equations is usually done by finite difference method (Anderson, 1995), finite volume method (Versteeg and Malalasekera, 1995) and finite element methods (Bathe, 1996). Numerical modeling of turbulence is also reviewed in the book by Pope (2000). Traditional turbulent models, such as the  $k$ - $\epsilon$  method and the  $k$ - $\omega$  method, solve the time-averaged Navier–Stokes equations and use a Reynolds stress term to close the governing equation. The Reynolds stress term is modeled based on the assumption of homogeneous turbulence and a turbulent viscosity solely dependent on the turbulent kinetic energy. These models can give satisfactory result for steady state flows, but are not suitable for unsteady flows. Due to the time-averaging of turbulent structure, the methods cannot capture the oscillatory fluid structure in the gap areas in a rod array (Lee and Jang, 1997). This oscillatory flow in the gap areas has been observed in experiments (e.g., Hooper, 1980). To solve the unsteady flow, time-dependent terms and a time-marching scheme are included in the equations that govern the mean flow. The Reynolds stress term can also be solved using the time-dependent Reynolds stress transport equations so that a better solution of the dynamic properties of the flow can be obtained. Using the unsteady Reynolds stress method, Chang and Tavoularis (2005 and 2007) successfully captured the oscillatory fluid structure in the gap area between a single cylinder and a wall, and in the gap areas between cylinders in a 37-element CANDU fuel bundle. The Reynolds stress method requires the modeling of the turbulent diffusion, pressure strain and dissipation terms in the transport equation for the Reynolds stress, which involves a number of empirical coefficients. These coefficients need to be chosen carefully for different applications since they vary considerably with Reynolds numbers.

An alternative approach to model turbulence is the large eddy simulation (LES) (Sagaut, 2006). The LES method uses mesh-based spatial filters to separate large scale and small scale eddies. Large scale eddies, which are responsible for the transport of most of the momentum and energy, are directly solved; and the small scale eddies, which are associated with turbulent energy dissipation, are modeled. The large eddies are geometry-dependent and unsteady in nature, and therefore the direct solution of the large eddies provides better accuracy in modeling the large scale fluid motion in a complex flow channel. Modeling of small scale eddies, known as subgrid-scale (SGS) modeling, allows less computational effort than the direct numerical simulation (DNS) of the Navier-Stokes equations. The Smagorinsky model based on the Boussinesq's approximation (Smagorinsky, 1963) is commonly used. An improvement on the Smagorinsky model is the dynamic subgrid-scale model (DSGS) proposed by Germano *et al.* (1991) and modified by Lilly (1992).

Hassan and Barsamian (1999) applied the Smagorinsky model and the DSGS model based on Lilly's modification to the flow crossing a 9-cylinder bundle. Their work demonstrated the applicability of LES in solving practical engineering problems. Kim and No (2004) conducted a numerical simulation of the flow passing over a spacer grid in a fuel element cluster using LES. Mayer *et al.* (2007) solved the flow in a subchannel of a triangular cylinders bundle in axial flow using LES and captured the large vortices near the cylinders and the secondary flow across the gaps between cylinders. Recently, Abbasian *et al.* (2009) solved the three-dimensional flow over a 43-element fuel bundle using large eddy simulation (LES). Their model included the upstream flow, the endplates and the downstream flow. The simulation results showed the existence of a secondary flow that rotated about the center of the bundle in the subchannels between the intermediate ring and inner ring of fuel elements, and yielded a significant unsteady moment about the bundle axis.

### *1.3.3 Wall Pressure Measurement*

An immersed object is coupled with the fluid through the pressure field on the surface of the object. Therefore, measurement of the wall pressure is an important method to study the flow and the flow-induced vibration. The power and cross spectral densities of the

pressure field obtained through measurements can be used as excitations to calculate the response of the random vibration of a structure in a turbulent flow. Pressure measurement also provides validation for numerical simulations when velocity measurement is difficult to conduct. Excellent reviews on the fluctuating wall pressure measurement in a turbulent flow have been given by Willmarth (1975) and Bull (1995).

Au-Yang and Jordan (1980) measured the wall-pressure fluctuation around fuel elements in a laboratory reactor and a commercial reactor, and showed that most turbulence energy of the axial bundle flow is in the low frequency range. Curling and Paidoussis (1991) measured the wall pressure fluctuations on the surfaces of an array of rods in parallel flow and developed equations for predicting the wall pressure cross spectral densities for Strouhal numbers greater than 0.2. For lower Strouhal numbers, Wilson and Jones (1983) found that the wall pressure PSD is flat down to a Strouhal number about 0.008. However, due to the space limit and high sensitivity requirement of a pressure sensor, no wall pressure measurement on the fuel element surface in a CANDU fuel bundle is available in the literature as far today.

#### *1.3.4 Structural Modeling of Fuel Bundles*

Modeling of the CANDU fuel bundle is usually done using the finite element method. A state-of-the-art review on the finite element method can be found in Bathe's book (1996). In the literature, finite element modeling of CANDU fuel bundles for dynamic analysis is rarely seen. Static models were presented by Cho *et al.* (2000) and Horhoianu *et al.* (2006). A fuel bundle model with contact constraints was given by Xu *et al.* (2005).

Modeling of the fuel element is complicated by the contact between the fuel pellets and the sheath, thermal effect of the heat generation and viscoelasticity of the sheath and pellet materials. A comprehensive model of the fuel elements was given by Tayal *et al.* (1992). The fuel element was modeled as a composite beam in their BEAM code, taking consideration of fuel pellet cracking, creep, coolant pressure and thermal effect. In structural analysis, the fuel element can be further simplified as beams, as presented in the models of Cho *et al.* (2000) and Horhoianu *et al.* (2006).

There are more varieties on the modeling of endplates. In the BEAM code (Tayal *et al.*, 1992) endplates were simplified as rings and modeled using the curved beam theory instead of the finite element method. A straight beam finite element model of the endplate was used in the code developed by Xu *et al.* (2005). Straight beam finite element is easy to implement, but the accuracy is not always satisfactory. This is mainly because that a straight beam finite element can not capture the natural curvature of the circular rings, as shown in Figure 1.3. When the mean radius of a ring is not significantly larger than its cross-sectional dimensions, error is inevitable regardless of the number of finite elements used to discretize the ring. The curved beam finite elements, presented by Rakowski and Litewka (2000), Yang and Sin (1995), Zhu and Meguid (2004), can be used to overcome the curvature issue for an isolated ring. When dealing with a CANDU fuel endplate consisting of several rings separated by short ribs, the material overlapping becomes an issue.

Plate finite element is a good choice for achieving a balance among accuracy, model size and consistence in assembly with the fuel elements. The conventional Kirchhoff-Love plate theory (Timoshenko and Woinowsky-Krieger, 1959) deals with thin plate and cannot be applied to the current endplate with a width-to-thickness ratio of 1.1, which is regarded as very thick. The shear deformable plate theory developed by Mindlin (1951) assumes constant shear stress components in the plate cross-sections and requires a shear correction factor to compensate for the total potential energy. However, the shear stress components in the cross-sections are parabolic due to the theory of elasticity. Reddy developed a third-order thick plate theory (Reddy, 1984 and 1996) to properly model the shear stress in a thick plate. This was applied in modeling the circular rings in a CANDU fuel endplate by Yu and Wen (2007).

## CHAPTER 2 FLOW SIMULATION AND EXPERIMENTAL VALIDATION

Solution of the complete CANDU fuel bundle flow is rarely seen due to the complex geometry of the fuel bundle. The only available simulation model in the literature to date that includes endplates is the work done by Abbasian *et al.* (2009). Abbasian's model includes an individual 43-element CANDU fuel bundle with upstream/downstream pipe flows. The downstream condition used in that model does not reflect the actual condition for an inlet fuel bundle in a bundle string. The downstream condition however may significantly affect the flow in the fuel bundle and the fluid force acting on the bundle. In addition, the distribution of the fluid force has never been revealed. An improved model is needed.

This chapter presents the modeling and solution procedures of the fuel bundle flow using the large eddy simulation. The model covers a portion of upstream pipe flow, the inlet bundle and a half of the second bundle. Flow pattern in the entrance region of the inlet bundle is discussed. Emphasis is put on the effect of the endplates and how the flow transform from the pipe flow to fully developed bundle flow. The fluid force is obtained as excitation for the vibration analysis in the subsequent chapters.

A brief review of computational fluid dynamics and the large eddy simulation theory is given in Section 2.1. The modeling procedure of the bundle flow is described in Section 2.2. The numerical results obtained from the bundle flow model are presented in Section 0. The measurement of wall pressure fluctuation on the pressure tube is discussed in Section 2.4.

### 2.1 Large Eddy Simulation

#### 2.1.1 Filtering

In the large eddy simulation, a spatial filter is applied to the pressure and velocity fields so that any fluid structures larger than the filter scale will be solved. The fluid structures

that are smaller than the filter scale must be modeled using subgrid scale models. The spatial filter is usually defined in the following form (Sagaut, 2006)

$$\bar{\phi}(x, t) = \int_{-\infty}^{+\infty} \phi(\zeta, t) G_F(x - \zeta) d\zeta. \quad (2.1)$$

where  $\bar{\phi}(x, t)$  is the filtered scalar function  $\phi(\xi, t)$ ;  $G$  is the filter function. The filter function determines how the subgrid scale quantities are separated from the large scale quantities. Three classic filter functions are shown below:

Top-hat filter  $G_F(x - \zeta) = \begin{cases} 1/\Delta & \text{if } |x - \zeta| \leq \Delta/2; \\ 0 & \text{otherwise} \end{cases};$

Gaussian filter  $G_F(x - \zeta) = \left( \frac{\gamma}{\pi \Delta^2} \right)^{1/2} e^{-\frac{\gamma |x - \zeta|^2}{\Delta^2}};$

Fourier filter  $G_F(x - \zeta) = \frac{\Delta \sin[\pi(x - \zeta)/\Delta]}{\pi(x - \zeta)}.$

In the above equations,  $\zeta$  is a dummy variable;  $\Delta$  is the filter size,  $\gamma$  is a filter parameter.

### 2.1.2 Filtered Navier-Stokes Equations

The governing equations for an incompressible Newtonian fluid are the Navier-Stokes equations

$$\begin{cases} \frac{\partial u_i}{\partial t} + \frac{\partial(u_i u_j)}{\partial x_j} = -\frac{1}{\rho} \frac{\partial p}{\partial x_i} + \nu \frac{\partial}{\partial x_j} \left( \frac{\partial u_i}{\partial x_j} + \frac{\partial u_j}{\partial x_i} \right) \\ \frac{\partial u_i}{\partial x_i} = 0 \end{cases} \quad (i = 1, 2, 3), \quad (2.2)$$

where  $u_i$  is the flow velocity components;  $p$  is the pressure;  $\rho$  is the density and  $\nu$  is the kinematic viscosity. The first set of equations in Eq. (2.2) is the momentum equations; the second equation is the continuity equation.

Applying the filter function to the governing equations, the following filtered Navier-Stokes equations may be obtained (Versteeg and Malalasekera, 1995)

$$\begin{cases} \frac{\partial \bar{u}_i}{\partial t} + \frac{\partial(\bar{u}_i \bar{u}_j)}{\partial x_j} = -\frac{1}{\rho} \frac{\partial \bar{p}}{\partial x_i} + \nu \frac{\partial}{\partial x_j} \left( \frac{\partial \bar{u}_i}{\partial x_j} + \frac{\partial \bar{u}_j}{\partial x_i} \right) - \frac{\partial \tau_{ij}}{\partial x_j} \\ \frac{\partial \bar{u}_i}{\partial x_i} = 0 \end{cases} \quad (i=1, 2, 3). \quad (2.3)$$

where the overbar denotes the filtered value of a quantity. The term  $\bar{u}_i \bar{u}_j$  comes from  $\overline{u_i u_j}$ , the filtered value of  $(u_i u_j)$ . It is preferable to replace  $\overline{u_i u_j}$  with  $\bar{u}_i \bar{u}_j$  in the consideration that the filtered equations should contain only filtered quantities. The difference between  $\overline{u_i u_j}$  and  $\bar{u}_i \bar{u}_j$  arise as  $\tau_{ij} = \overline{u_i u_j} - \bar{u}_i \bar{u}_j$ , known as the residual stress tensor.

There is a variety of decompositions. The classic decomposition is a three-term composition proposed by Leonard (1974) and leads to

$$\tau_{ij} = \hat{L}_{ij} + \hat{C}_{ij} + \hat{R}_{ij}, \quad (2.4)$$

where  $\hat{L}_{ij} = \overline{u_i u_j} - \bar{u}_i \bar{u}_j$ ;  $\hat{C}_{ij} = \overline{u_i u'_j} - \bar{u}_i \bar{u}'_j$ ;  $\hat{R}_{ij} = \overline{u'_i u'_j}$ ; and  $u'_i = u_i - \bar{u}_i$  ( $i=1, 2, 3$ ) denoting the high wavenumber spatial fluctuation of velocity. An improved decomposition is given by Germano (1986) in the same form as Eq. (2.4), but with  $\hat{L}_{ij} = \overline{u_i u_j} - \bar{u}_i \bar{u}_j$ ;  $\hat{C}_{ij} = \overline{u_i u'_j} + \overline{u'_i u_j} - \bar{u}_i \bar{u}'_j - \bar{u}'_i \bar{u}_j$ ;  $\hat{R}_{ij} = \overline{u'_i u'_j} - \bar{u}'_i \bar{u}'_j$ . In the second decomposition,  $\hat{L}_{ij}$  is called Leonard stresses and represents the interaction between the filtered velocities, or large scale motions.  $\hat{C}_{ij}$  is called cross stresses and represents the interaction between the large scale motions and the small scale motions.  $\hat{R}_{ij}$  is the SGS Reynolds stresses and represents the interaction between subgrid scale motions. The residual stress tensor can be expressed as the  $\tau_{ij} = \tau_{ij}^r + \frac{2}{3} k_r \delta_{ij}$ , where  $\tau_{ij}^r$  is the anisotropic residual tensor and  $k_r = \tau_{ii}^r / 2$  is defined as the residual kinetic energy.  $\tau_{ij}^r$  needs to be modeled.

In the Smagorinsky subgrid model, the anisotropic residual stress tensor is expressed as

$$\tau_{ij} = -2\nu_r \bar{S}_{ij}, \quad (2.5)$$

where  $\bar{S}_{ij} = (\partial \bar{u}_i / \partial x_j + \partial \bar{u}_j / \partial x_i) / 2$  is the filtered rate of strain, and  $\nu_r$  is the so-called eddy viscosity in analogy to viscosity that relates stress and rate of strain. The eddy viscosity is

defined as  $v_r = (C_S \Delta)(2\bar{S}_{ij}\bar{S}_{ij})^{1/2}$ , where  $C_S$  is a parameter with its typical value set to 0.1~0.25;  $\Delta$  is the filter width, usually the size of the computational grids.

### 2.1.3 Spatial Discretization

The fluid domain is discretized by the finite volume method (Versteeg and Malalasekera, 1995). First, Eq. (2.4) is written in the following vector form

$$\begin{aligned} \frac{\partial \bar{\mathbf{v}}}{\partial t} + \nabla \cdot (\bar{\mathbf{v}}\bar{\mathbf{v}}) &= -\frac{1}{\rho} \nabla \bar{p} + \nu \nabla \cdot \nabla \bar{\mathbf{v}} + \boldsymbol{\tau} \cdot \nabla ; \\ \nabla \cdot \bar{\mathbf{v}} &= \mathbf{0}, \end{aligned} \quad (2.6)$$

where  $\bar{\mathbf{v}}$  is the filtered velocity vector and  $\boldsymbol{\tau}$  is the residual stress tensor.

The above governing equations are integrated in a control volume,  $V_c$ .

$$\begin{aligned} \int_{V_c} \frac{\partial \bar{\mathbf{v}}}{\partial t} dV + \int_{V_c} \nabla \cdot (\bar{\mathbf{v}}\bar{\mathbf{v}}) dV &= -\frac{1}{\rho} \int_{V_c} \nabla \bar{p} dV + \int_{V_c} \nu \nabla \cdot \nabla \bar{\mathbf{v}} dV + \int_{V_c} \boldsymbol{\tau} \cdot \nabla dV ; \\ \int_{V_c} \nabla \cdot \bar{\mathbf{v}} dV &= \mathbf{0}. \end{aligned} \quad (2.7)$$

Recall that the Gauss' divergence theorem is

$$\int_{V_c} \nabla \cdot \mathbf{a} dV = \int_{A_c} \mathbf{n} \cdot \mathbf{a} dA, \quad (2.8)$$

where  $\mathbf{a}$  is a vector,  $A_c$  is the boundary area of the control volume,  $\mathbf{n}$  is the normal of the boundary. Applying the Gauss' divergence theorem to the governing equations

$$\begin{aligned} \int_{V_c} \frac{\partial \bar{\mathbf{v}}}{\partial t} dV + \int_{A_c} \mathbf{n} \cdot (\bar{\mathbf{v}}\bar{\mathbf{v}}) dA &= -\frac{1}{\rho} \int_{A_c} \bar{p} \mathbf{n} dA + \int_{A_c} \nu \mathbf{n} \cdot \nabla \bar{\mathbf{v}} dA + \int_{A_c} \boldsymbol{\tau} \cdot \mathbf{n} dA ; \\ \int_{A_c} \mathbf{n} \cdot \bar{\mathbf{v}} dA &= \mathbf{0}. \end{aligned} \quad (2.9)$$

The control volume is defined using finite volume grid, as shown in Figure 2.1. According to the mean value theorem, the integral of a continuous function on a surface (or volume) can be replaced by the product of the area (or volume) and the value of a point within the surface (or volume). The arbitrary point is approximated by the point at the middle of the surface, the hollow points in Figure 2.1, for surface integral; or the point at the middle of the volume, the solid point in Figure 2.1, for volume integral. The

hollow points are often referred to surface centroid, and the solid point is often referred as the node of the finite volume.

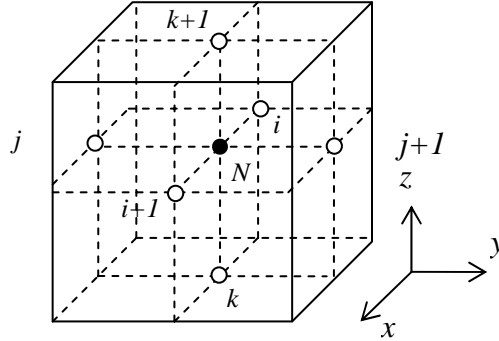


Figure 2.1 A finite volume element.

Applying this rule to Eq. (2.9), the governing equations turn to their discretized forms which only contain the velocity and pressure values at the surface (hollow) points and the volume center (solid) point.

$$\begin{aligned} \frac{\partial}{\partial t}(\bar{v}_N)\Delta V + \sum_m (\mathbf{n}A_m) \cdot (\bar{\mathbf{v}}_m \bar{\mathbf{v}}_m) = -\frac{1}{\rho} \sum_m (\mathbf{n}A_m) \cdot \bar{P}_m \\ + \sum_m v(\mathbf{n}A_m) \cdot (\nabla \bar{\mathbf{v}})_m + \sum_m (\mathbf{n}A_m) \cdot (\boldsymbol{\tau})_m; \end{aligned} \quad (2.10)$$

$$\sum_m (\mathbf{n}A_m) \cdot \bar{\mathbf{v}}_m = \mathbf{0}. \quad (2.11)$$

In the above equations,  $\Delta V$  is the discretized volume; the subscript represent the discretized value of a quantity;  $m$  takes the value of  $(i, i+1, j, j+1, k, k+1)$  as shown in Figure 2.1. The surface velocity gradient term  $(\nabla \bar{\mathbf{v}})_m$  can be evaluated using finite difference method from the nodes of neighboring elements.

$$\nabla \bar{\mathbf{v}}_m = \frac{1}{2}(\bar{\mathbf{v}}_{M-1} + \bar{\mathbf{v}}_M), \quad (2.12)$$

where  $M$  takes the value of  $(I, I+1, J, J+1, K, K+1)$ .

The pressure in Eq. (2.12) needs some special treatment. It is noticed that the four equations in Eq. (2.12) are all about velocity, and there is no dedicated equation for pressure. Solution of pressure is implicitly contained in the four equations as a constraint:

if a correct pressure field is applied, the velocities should satisfy the continuity equation. This is the pressure-velocity coupling. A popular way to deal with pressure-velocity and other nonlinearities in Eq. (2.12) is through iteration. First, a guessed value of pressure  $p^*$  is used to calculate the guessed velocity field  $\bar{v}^*$  from the momentum equations Eq. (2.10). There is a difference between the true value and the guessed value for the pressure and the velocities

$$p = p^* + p^{\sim}; \quad \bar{v} = \bar{v}^* + \bar{v}^{\sim}, \quad (2.13)$$

where a value with a superscript ( $\sim$ ) denotes the deviation from the true value. Substituting Eq. (2.13),  $p^*$  and  $\bar{v}^*$  into Eq. (2.10), a relationship between  $p^{\sim}$  and  $\bar{v}^{\sim}$  can be found as function  $\bar{v}^{\sim} = g(p^{\sim})$ , and in consequence

$$\bar{v} = \bar{v}^* + g(p^{\sim}). \quad (2.14)$$

Substitute Eq. (2.14) into the continuity equation, Eq. (2.11), the pressure correction  $p^{\sim}$  can be solved at every node. The corrected velocity field can then be obtained. Repeating this process until the difference between the velocities at successive iterations is smaller than a convergence threshold. The convergence is measured based on the scaled residual. The residual refer to the sum of the imbalance in the governing equations Eq. (2.10) obtained at the end of each iteration. The scaled residual is calculated by dividing the residual with the maximum residual obtained in the first five iterations. The convergence criterion is set to 0.001 for the scaled residual. If the scaled residual is smaller than the criteria, convergence is achieved and the solver stops iterating for the current time step and moves on to the next time steps.

In the calculation of  $\bar{v}^{\sim} = g(p^{\sim})$  at a node, the velocity corrections  $\bar{v}^{\sim}$  at surrounding nodes are needed. These correction terms are omitted, but the omission does not affect the final result if the result is converged, because a converged result leads to zero value of  $p^{\sim}$  and  $\bar{v}^{\sim}$ . The above procedure is developed by Patankar and Spalding (1972), and is known as the SIMPLE algorithm. However, the iteration is prone to diverge; therefore relaxation factors  $\alpha_p$  and  $\alpha_i$  are always used to guarantee convergence

$$\begin{aligned}
 p^n &= p^* + \alpha_p p^\sim; \\
 u_i^n &= \alpha_i u_i^n + (1 - \alpha_i) u_i^{(n-1)} \quad (i = 1, 2, 3),
 \end{aligned}
 \tag{2.15}$$

where  $n$  denotes  $n$ -th iteration.

#### 2.1.4 Solution of the Time Marching Problem

The time derivative in Eq. (2.10) needs to be resolved using a time marching scheme. The whole equation is integrated with respect to time from  $t$  to  $t + \Delta t$ .

$$\begin{aligned}
 (\bar{\mathbf{v}}_N^{t+\Delta t} - \bar{\mathbf{v}}_N^t) \Delta V + \int_t^{t+\Delta t} \sum_m (\mathbf{n}A_m) \cdot (\bar{\mathbf{v}}_m \bar{\mathbf{v}}_m) dt &= - \int_t^{t+\Delta t} \frac{1}{\rho} \sum_m (\mathbf{n}A_m) \cdot \bar{p}_m dt \\
 + \int_t^{t+\Delta t} \sum_m \mathbf{v}(\mathbf{n}A_m) \cdot (\nabla \bar{\mathbf{v}})_m dt + \int_t^{t+\Delta t} \sum_m (\mathbf{n}A_m) \cdot (\boldsymbol{\tau})_m dt;
 \end{aligned}
 \tag{2.16}$$

The time integration of a scalar function  $\phi(t)$  can be approximated by

$$\int_t^{t+\Delta t} \phi(t) dt \doteq \phi(t) \Delta t = \phi^t \Delta t; \text{ or}
 \tag{2.17}$$

$$\int_t^{t+\Delta t} \phi(t) dt \doteq \phi(t + \Delta t) \Delta t = \phi^{t+\Delta t} \Delta t.
 \tag{2.18}$$

Applying Eq. (2.17) or Eq. (2.18) to Eq. (2.16) will produce a time discretized equation. If Eq. (2.17) is used, the velocity at time  $t + \Delta t$  can be directly obtained from the quantities at time  $t$ . This is called an explicit scheme. If Eq. (2.18) is used, the velocity at time  $t + \Delta t$  must be obtained by solving algebraic equations, which leads to an implicit scheme. The implicit scheme is unconditionally stable and generally provides better accuracy than the explicit scheme for incompressible flow. Using the implicit scheme, Eq. (2.16) can be re-written as

$$\begin{aligned}
 \frac{\bar{\mathbf{v}}_N^{t+\Delta t} - \bar{\mathbf{v}}_N^t}{\Delta t} \Delta V + \sum_m (\mathbf{n}A_m) \cdot (\bar{\mathbf{v}}_m^{t+\Delta t} \bar{\mathbf{v}}_m^{t+\Delta t}) &= - \frac{1}{\rho} \sum_m (\mathbf{n}A_m) \cdot \bar{p}_m^{t+\Delta t} \\
 + \sum_m \mathbf{v}(\mathbf{n}A_m) \cdot (\nabla \bar{\mathbf{v}})_m^{t+\Delta t} + \sum_m (\mathbf{n}A_m) \cdot (\boldsymbol{\tau})_m^{t+\Delta t}.
 \end{aligned}
 \tag{2.19}$$

Combining Eq. (2.19) and the SIMPLE procedure, the pressure and velocity at time  $t + \Delta t$  can be solved.

## 2.2 Computational Model

### 2.2.1 Definitions

The components in a bundle-tube system are identified in Figure 2.2. To reduce complexity, spacer pads and bearing pads are not included in the flow simulation model.

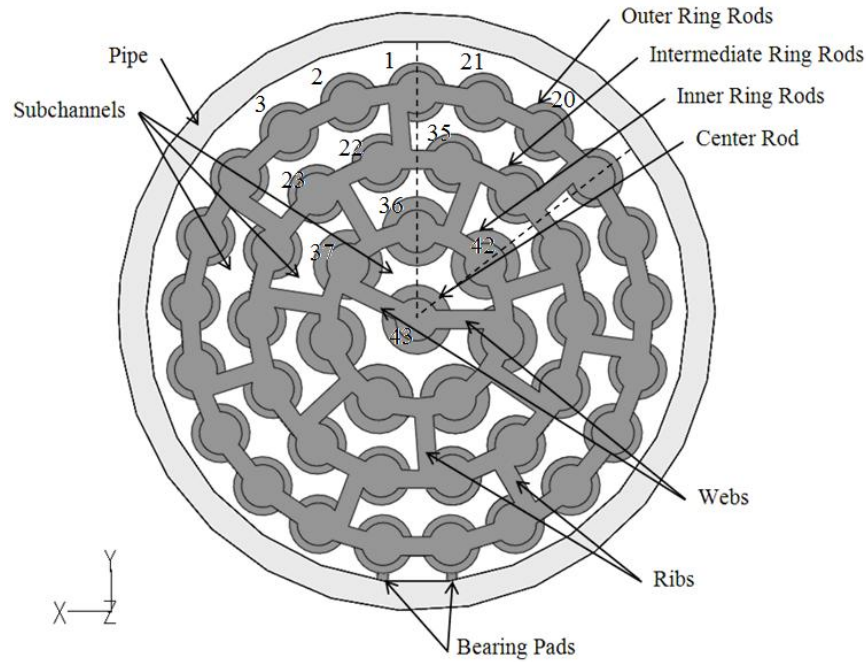
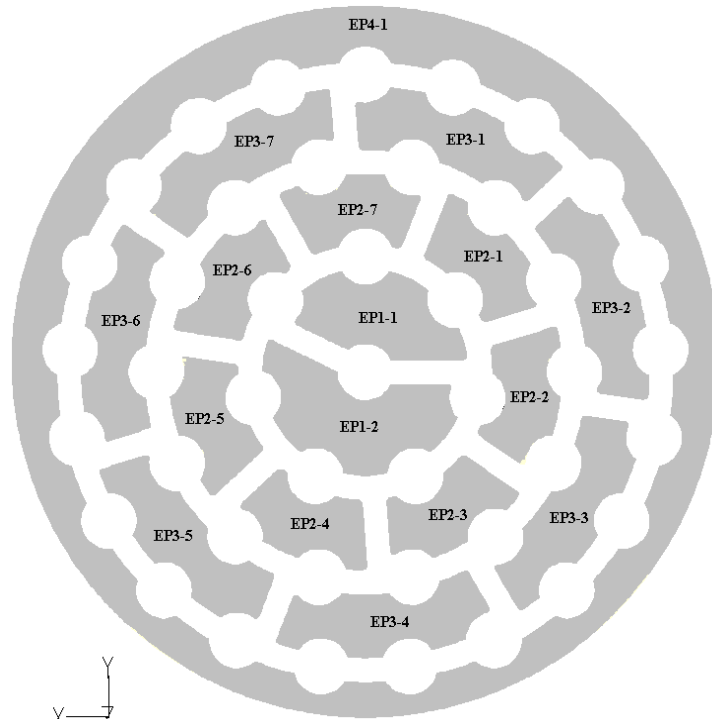
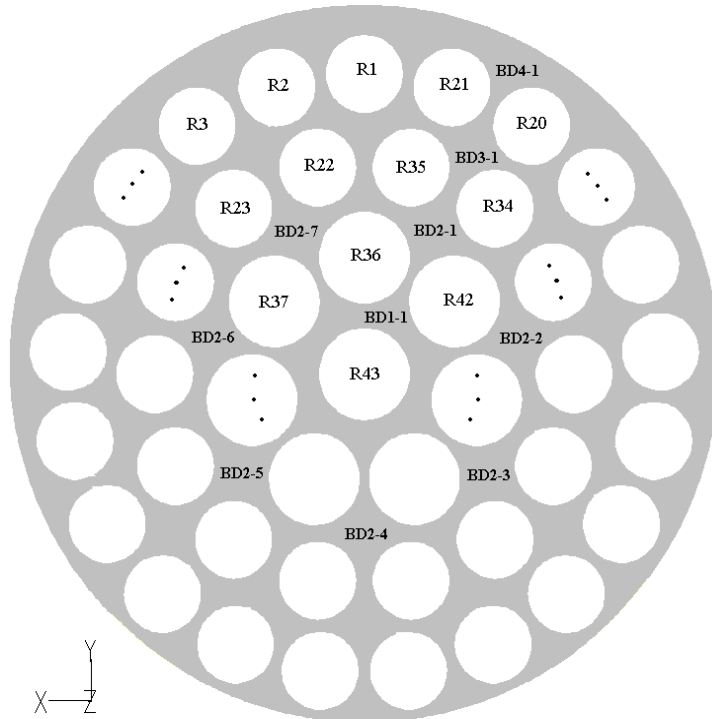


Figure 2.2 Definition of the bundle components.

Flow enters the fuel element subchannels through endplate subchannels. There are three types of subchannels in the bundle, surrounded by three fuel elements, four fuel elements and five fuel elements, respectively. The subchannels between the inner ring and intermediate ring of fuel elements are of particular interest. A label is assigned to each of the subchannels as shown in Figure 2.3. The hydraulic diameters of subchannels are slightly different. Instead of using the local hydraulic diameter for each subchannel, the hydraulic diameter of the entire bundle flow is used as a reference throughout this thesis. Its value is evaluated from  $D_h = 4A_f / P_{wet}$ , where  $A_f$  is the cross-sectional area of the bundle flow and  $P_{wet}$  is the wetted perimeter, which is the total length of the solid-fluid border in the cross section. The hydraulic diameter of the bundle flow is calculated as  $D_h \approx 0.008$  m for the simulated fuel bundle.



(a)



(b)

Figure 2.3 Definition of the flow channels: (a) endplate flow; (b) bundle flow.

### 2.2.2 Flow Model Parameters

The flow model is built and solved using commercial package FLUENT<sup>®</sup> 6. The three-dimensional computational fluid dynamics model consists of six distinct regions: 1) the upstream pipe flow region; 2) the flow passing the upstream endplate of the first bundle; 3) the flow around the fuel elements of the first bundle; 4) the flow passing the downstream endplate of the first bundle; 5) the flow passing the upstream endplate of the second bundle; 6) the flow inside the second bundle. These regions are shown in Figure 2.4. Each region is discretized individually using a different meshing scheme. As a result, the meshes at the interfaces between two neighboring regions are not compatible with each other. A non-conformable mapping is therefore used between the meshes to transfer data from one region to another. The global inertia frame is chosen as shown in Figure 2.4. The X-Y plane aligns with the upstream face of the upstream endplate of the inlet bundle with Z-axis coinciding with the longitudinal axis of the bundle. The density of the fluid is  $\rho = 1000 \text{ kg/m}^3$ , and the kinematic viscosity  $\nu = 1 \times 10^{-6}$ .

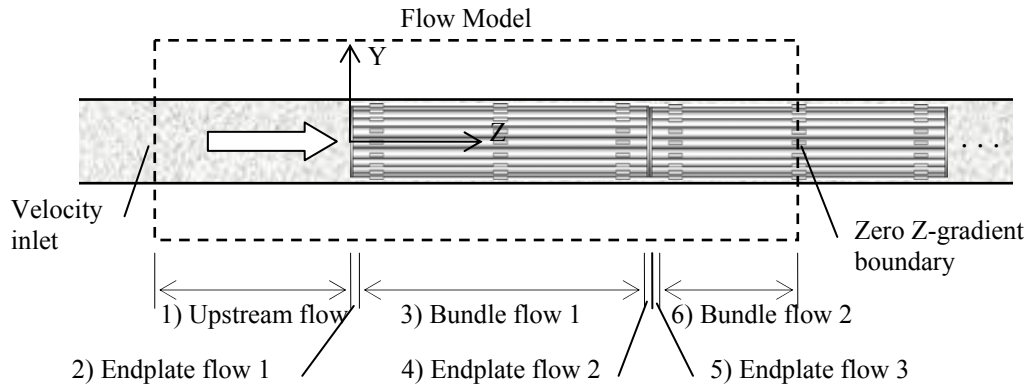


Figure 2.4 The flow regions.

The interested flow condition, or global Reynolds number inside the bundle, is about 54000. This Reynolds number corresponds to an average flow velocity of 3.0 m/s in the upstream and an average flow velocity of 6.8 m/s inside the bundle. The length scale of turbulence  $\eta$  in the bundle flow regions can be estimated with Kolmogorov microscales

<sup>®</sup> FLUENT is a registered trademark of ANSYS Inc.

(Tennekes and Lumley, 1972) as  $\eta/l \sim Re^{-3/4}$ , where  $l$  is the characteristic length of the flow, or  $D_h$ . The turbulent length scale in the bundle is  $\eta \sim 2 \times 10^{-6} m$ . In large eddy simulation, the microscale turbulence is modeled and only large scale eddies are directly solved with the filtered Navier–Stokes equations. Therefore, the restriction of the grid size depends on the dimension of the smallest eddy of interest in the simulation. In this model, Wedge grid is used. The axial discretization interval is 3 mm in average in a bundle. Finer discretization is used near the endplates, in which the grid length is about 1.5 mm. The mesh near the midplane of the bundles is coarser, with a length of 4.5 mm. The bundle flow cross section is discretized using a very fine mesh with the maximum mesh size lower than 1.5 mm in all directions. The axial discretization of the upstream pipe flow and the bundle flow for the inlet bundle are shown in Figure 2.5 and Figure 2.6 respectively. Meshing of the second bundle follows the same scheme of the inlet bundle.

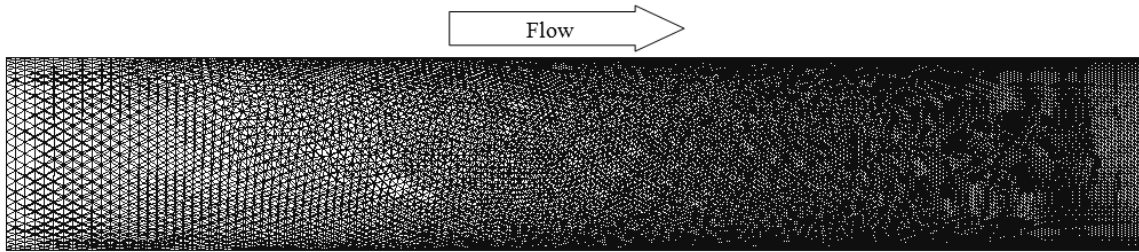


Figure 2.5 The axial discretization of the flow regions in the upstream pipe.

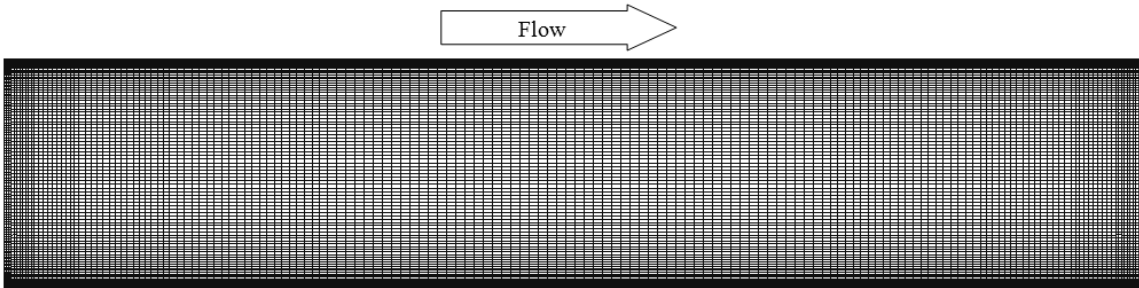


Figure 2.6 The axial discretization of the flow regions in a bundle and its endplates.

To achieve good accuracy in the near wall region, 10 thin layers of hexahedron grids with a thickness growing factor of 1.3 are used near the fuel element surfaces and the pipe surface to simulate the boundary layer. The thickness of the first layer is 0.01 mm, which corresponds to  $y^+=1$  (dimensionless wall distance) on most surfaces, except in the

vicinity of the leading edges of the fuel elements. The total thickness of the real boundary layer existing in the flow inside a bundle can be estimated as

$$\delta \sim \frac{0.5x}{\sqrt{\text{Re}_x}} = \frac{(0.5)(0.5)}{1844} = \frac{0.25}{1844} \doteq 0.135 \times 10^{-3} \text{ m} = 0.135 \text{ mm}, \quad (2.20)$$

where  $\text{Re}_x = Ux/\nu = 3.4 \times 10^6$ , and  $x = 0.5$  m (bundle length). This estimation is based the boundary layer thickness of flat plate in an open shear flow (Currie, 1974). The thickness calculated in this way is larger than that in a confined flow. The total thickness of the boundary layer mesh must be larger than the boundary layer thickness in the actual flow, therefore this estimation is conservative. The total thickness of the boundary layer mesh is 0.426 mm. The endplate flow contains 17 subchannel flows as shown in Figure 2.3. The flows are discretized using the same scheme as the bundle flow, except that the grid size in the Z-direction is 1 mm and remains uniform throughout the endplate depth. The upstream flow includes the pipe flow of  $6D_p$ , where  $D_p$  is the pipe diameter and its value is 4 inch in imperial units or 0.1016 m in metric units. The pipe flow is discretized using tetrahedron grids. The boundary layer thickness is estimated using the same method as that of the bundle flow. The meshes in the cross section of a bundle and an endplate are shown in Figure 2.7. Detailed information about the mesh can be found in Table 2.1.

Table 2.1 Mesh parameters.

Item	Value	Unit
Total number of grids	5.4	million
Bundle flow		
Boundary layer first layer thickness	0.01	mm
Boundary layer growth factor	1.3	--
Boundary layer division	10	--
Core flow mesh type	Wedge	--
Core flow mesh size	1.5	mm
Endplate flow		
Boundary layer first layer thickness	0.02	mm
Boundary layer growth factor	1.3	--
Boundary layer division	10	--
Core flow mesh type	Wedge	--
Core flow mesh size	1.0	mm
Upstream flow		
Boundary layer first layer thickness	0.02	mm
Boundary layer growth factor	1.3	--
Boundary layer division	10	--
Core flow mesh type	Tetrahedron	--
Core flow mesh size	1 – 4	mm

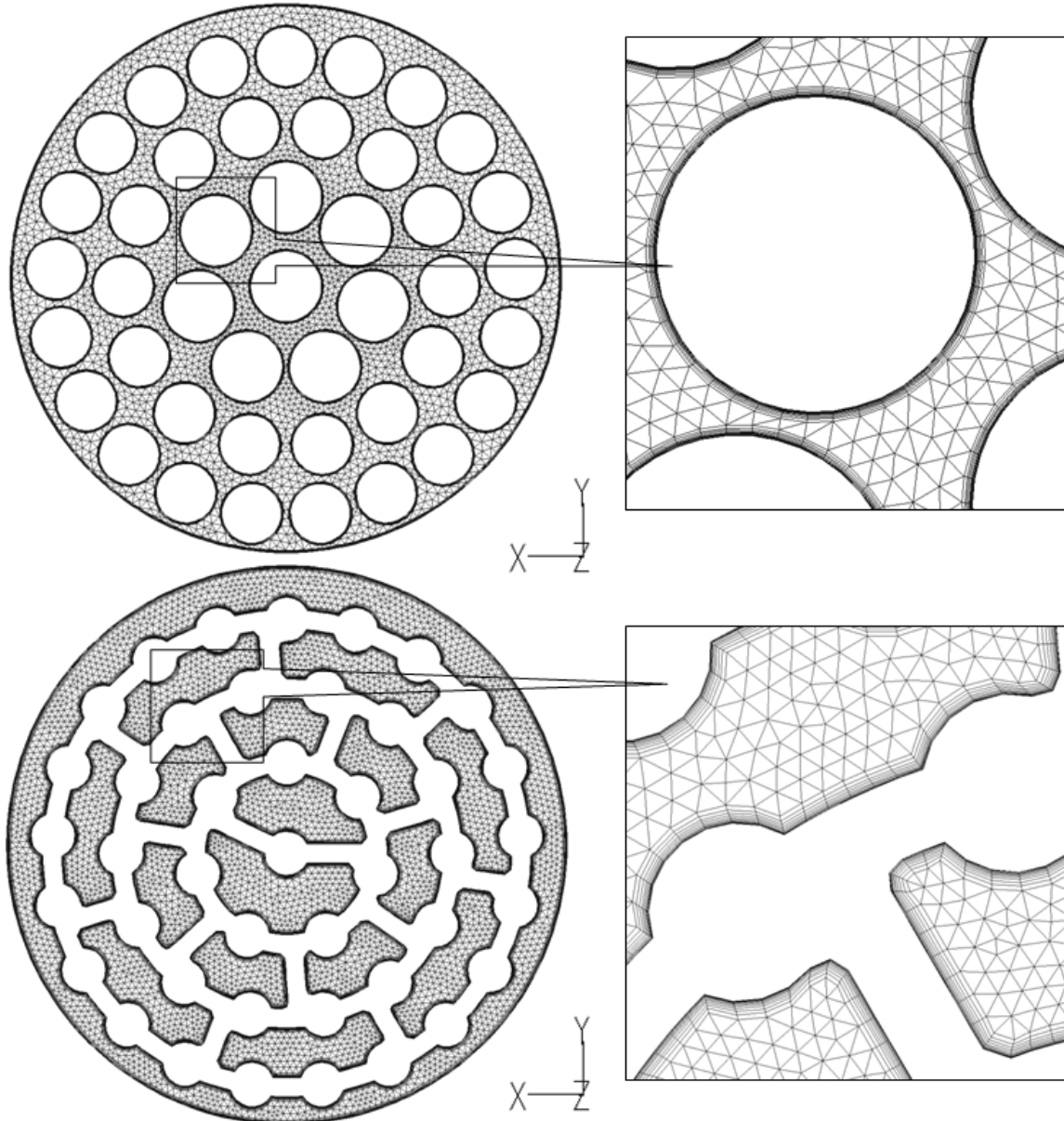


Figure 2.7 The cross-sectional discretization in a bundles and an endplates.

The upstream boundary condition is set to velocity inlet, with a uniform velocity of 3 m/s. The downstream boundary condition is set to “outflow” boundary condition, in which the Z-gradient of velocity and pressure at the boundary is zero, but the gradients in X- and Y-direction are allowed. This boundary condition simulates the fully developed flow. The distance from the upstream endplate to the location, beyond which the flow is fully developed, can be regarded as the entrance length of that bundle, denoted by  $L_e$ . For the turbulent flow entering a circular or rectangular duct, White (2003) suggests that the

entrance length can be approximated by  $L_e = 4.4 \text{Re}^{1/6}$ , while Anselmet *et al.* (2009) suggest  $L_e = 1.6 \text{Re}^{1/4}$ . For a Reynolds number in the interested range of 54000, both formulas give a similar maximum entrance distance of about  $30D_h$ . The second bundle is truncated at the midplane, which corresponds to  $31.25 D_h$ . Since no pressure boundary condition is set, a reference pressure is needed to eliminate the free degree of freedom in the pressure field. The reference pressure is set to zero at the origin of the global inertial frame, as shown in Figure 2.4. All the pressure results presented later are relative to this reference pressure.

The flow is solved in the time domain. The time step can be determined based on the time scale  $\tau \sim l \tilde{u}^{-1} \text{Re}^{-1/2} = 4 \times 10^{-5} \text{ s}$ , where  $l$  again is the characteristic length and its value is taken as that of the hydraulic diameter  $D_h = 0.008 \text{ m}$ , and  $\tilde{u}$  is the fluctuating velocity whose value is estimated to be 10% of the mean flow velocity of  $U = 6.8 \text{ m/s}$ . This leads to a sampling frequency of 25000 Hz. According to the Nyquist sampling theorem, the highest frequency that a periodic signal can be reconstructed without aliasing problem is half of the sampling frequency which is 12500 Hz in the current situation. However, the maximum discernable frequency related to the transportation of eddies depends on the eddy convective velocity  $U_c$ , the mesh size  $d_m$ , and the number of spatial points to represent a wave. According to Clinch (1969), the convective velocity, in the boundary layer of a pipe flow is independent of frequency and approximately equal to 0.6 times of the mean flow velocity except in the very low frequency range. Au-Yang (1980) indicated a value around 0.7~0.9 time of the mean flow velocity in a more complicated flow channel, e.g. a pressurized water reactor vessel. In the current flow condition,  $U_c$  is approximated to  $0.6U$ . If a wave can be represented by 2 spatial points (or 2 mesh grids) according to the Nyquist sampling theorem, the highest reliable frequency that can be discerned is determined by  $f = U_c / (2d_m)$ . For the average mesh size of 3 mm along the bundle axis, this frequency is about 680 Hz.

### 2.2.3 Grid Quality and Convergence

The mesh used in the fluid model needs to be examined for its quality. The slenderness of a grid is reflected by its aspect ratio. The aspect ratio is defined as the ratio between the

length of the longest edge and the length of the shortest edge. Ideally, the aspect ratio should be kept as unity, but a higher value may be allowed for the parallel flow in a narrow flow channel; however, the maximum aspect ratio should not exceed 5. In this model, the highest aspect ratio is about 3, located in the region near the midplane of the bundle. The flow in this region is mainly parallel flow. The aspect ratio near the endplates is set to 1, because the flow in this region is more isotropic. The maximum aspect ratio in the endplate region is close to 1. The maximum aspect ratio in the upstream pipe flow is about 1.5.

Grid skewness is another important indicator of grid quality. Skewness is defined using the deviation of the angle at the corner of a grid cell to its equiangular value. For example, when triangular mesh is used to discretize the cross-section of the bundle flow, the equiangular value, denoting as  $q_e$  is 60 degree. After creating the mesh, the maximum angle and minimum angle in a cell may be  $q_{max}$  and  $q_{min}$  respectively. The skewness is calculated as

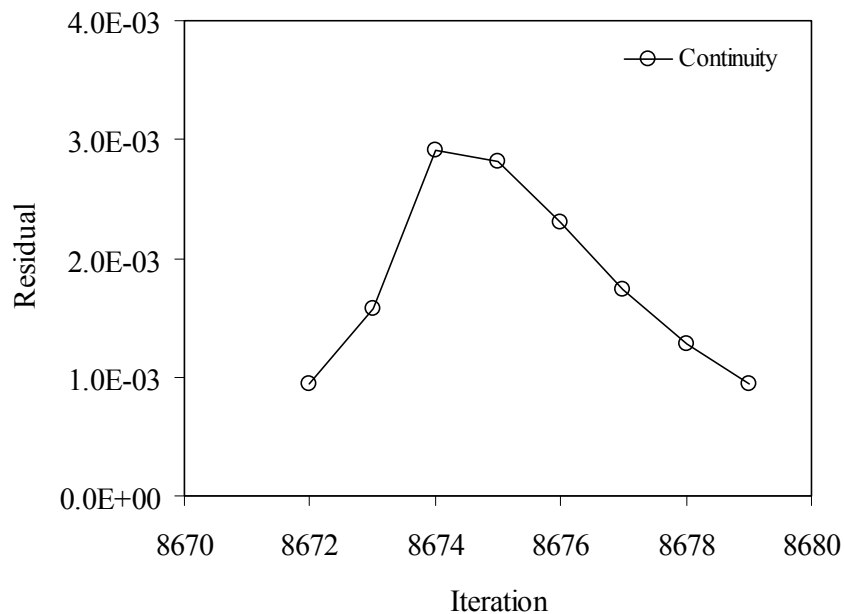
$$\text{skewness} = \max \left[ \frac{q_{max} - q_e}{180 - q_e}, \frac{q_e - q_{min}}{q_e} \right]. \quad (2.21)$$

Skewness is a value varies between 0 and 1. High skewness represents that the grid contains very sharp angles or obtuse angles. Grids with these angles usually produce large computational error and lead to the failure of the solution. The allowed maximum skewness in FLUENT is 0.98; however, the maximum skewness in a mesh should not exceed 0.9 for good accuracy. The highest skewness in this model is 0.78.

Accuracy of the numerical results is highly dependent on the convergence of the solution process. As mentioned in Section 2.1, the solution is a time marching process. In each time step, a nonlinear equation is solved in an iteration manner. The iteration is controlled by a stopping criterion measured with the normalized residuals in the governing equations. The larger the time step, the more the iterations are involved in each time step. However, a minimum of two iterations must be retained in a time step to solve the nonlinear governing equations. Too few steps of iteration may indicate that the time step is smaller than needed and the solution is not economical. A large time step leads to a

reduction of the total number of time steps, but the total number of iterations may increase since the number of iterations in each time step increases. It is found that 5 to 10 iterations in a time step is a balanced choice. However, the jump of the residuals between two time steps should not exceed one order of magnitude unless the value is far smaller than the stop criterion; otherwise artificial oscillation in the solution may occur. In the current model, the solution in each time step reaches convergence in 8 iterations. Figure 2.8 shows the convergence history of the residuals in the continuity equations and the momentum equations. The residual jumps in all equations are lower than one order of magnitude. The convergence in the continuity equation is slower than that in the momentum equations.

If the time step size is large or the mesh quality is low, the time marching solution may not be stable even the iteration in each time step is converged. The number of iterations in each time step will gradually increase and the solution process will end up with divergence. This model has been tested for stability. It is found that the number of iteration is constantly 8 through out the entire solution process and no sign of divergence is seen. Figure 2.9 shows the residuals at the last iteration in each time step for 100 time steps. It can be seen that the solution process is stable.



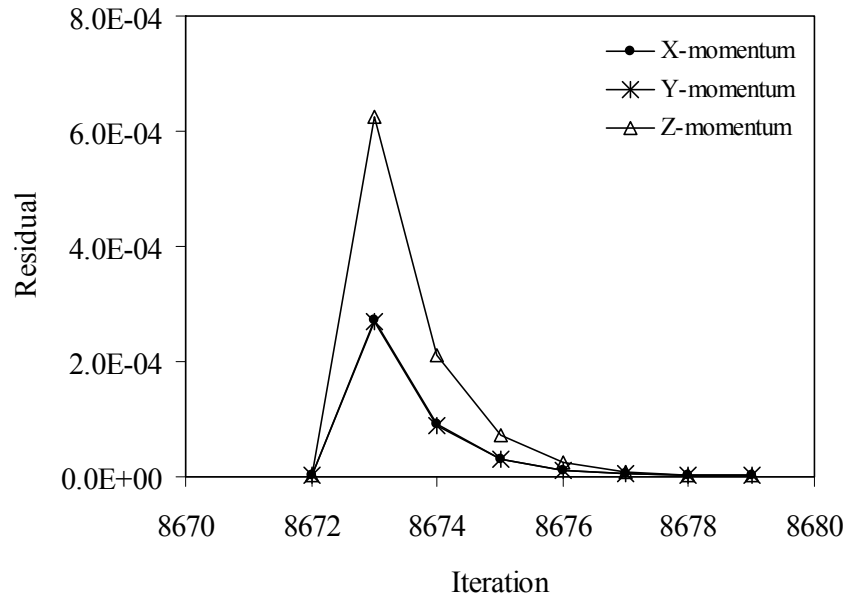


Figure 2.8 History of the residuals in the continuity equation (top) and the momentum equations (bottom) within a time step.

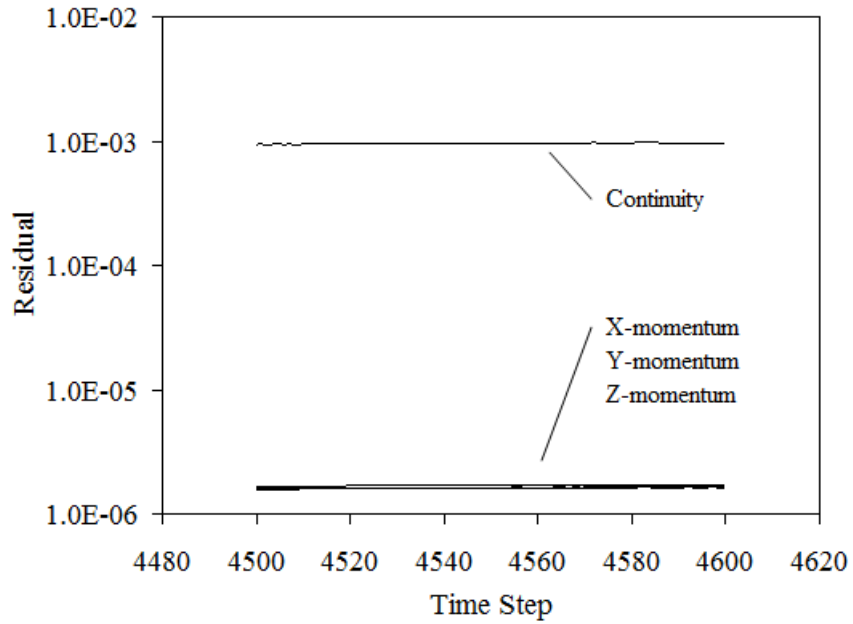


Figure 2.9 History of the residuals at the last iteration in each time step over 100 time steps.

## 2.3 Simulation Results

The flow model was solved using parallel processing on HPCVL computers, a high performance computing network attached to Queen’s University, Kingston, Ontario, Canada. Each simulation involves 24 processors and 192 GB memory. It took about 400 CPU hours to obtain a solution of 25000 time steps, or one second in flow time duration. A steady state solution was first sought using the  $k$ -epsilon method, and then the large eddy simulation was launched to obtain an unsteady solution. After 4000 time steps, a transition from the steady state solution to transient solution was completed.

### 2.3.1 Entrance Flow and Bundle Interface Flow

A number of axial locations in a bundle are chosen to examine the simulation result. The relative distances between each location and the upstream endplate-fuel-element interface of the bundle are shown in Table 2.2.

Table 2.2 Result inspection locations.

Location	Distance* (mm)	Location	Distance* (mm)	Location	Distance* (mm)
L1	10	L4	140	L7	430
L2	30	L5	250	L8	470
L3	70	L6	360	L9	490

\*Relative to the endplate-fuel-element interface at the upstream end of the bundle.

Figure 2.10 shows the in-plane velocity vectors at the inlet bundle cross section at location L1 of the inlet bundle at time  $t = 0.16$  s. Note that the endplate profile is projected to the figure as a reference in the figure. This plotting scheme is also used in some other figures. It can be seen that a counter-clockwise swirling flow exists between the intermediate ring and inner ring of fuel elements (BD2 subchannels as shown in Figure 2.3). Vortices can be found after each endplate rib and web. Inter-subchannel flows can be seen between different rings of subchannels. A preferred direction of inter-subchannel flows can also be seen among the BD2 subchannels. The swirling in-plane velocity reaches 15% of the mean axial flow, which is significant. Figure 2.11 shows the velocity magnitude contour in the Y-Z plane near the entrance region. The lower part of the figure corresponds to the BD2-4 subchannel. Complicated cross flow pattern can be seen after the endplate rib-ring joint. The wake extends to the downstream for a significant distance.

Figure 2.12 shows the velocity magnitude at location L1 of the inlet bundle at time  $t = 0.16$  s. The average velocity in the top gap is higher than that in the bottom gap. High average velocity also occurs at the BD3-1 and similar subchannels due to the large local hydraulic diameters of these subchannels. Figure 2.13 shows the static pressure contour at location L1 of the inlet bundle at time  $t = 0.16$  s. The presence of the rib-ring joint introduces a wake behind it and thus creates a low pressure area in the BD2 subchannels. The rib is not placed symmetrically in each BD2 subchannel, and this leads to an unbalanced distribution of pressure. The pressure difference causes the flow to turn counter-clockwise after it passes the ribs. At the same time, the wall pressure on the fuel elements surrounding that subchannel is also unbalanced and leads to unbalanced forces and moments. The misalignment between the endplate subchannels (for example EP2-1) and the corresponding bundle subchannels (for example BD2-1) makes the flow in that bundle subchannel to have a preferred direction. This deviated wake flow is highly unstable. Figure 2.14 shows the temporal development of the three-dimensional vortex behind the endplate in the BD2-1 subchannels. Vortices shed off from the rib and sweep down along the BD2-1 subchannel. This leads to significant oscillation of the fluid forces and moments acting on the surrounding fuel elements. Although the generation of the unstable wake flow is localized to each BD2 subchannel, the flow is reinforced when passing through the neighboring subchannels in that ring, and develops into a global swirling flow that rotates about the Z-axis. The ribs and webs in other ring of subchannels also generate unbalanced wakes, but they are separated by multiple subchannels in the tangential direction, and thus can not develop into a global pattern.

In comparison to the flow after the inlet bundle, the flow that enters the second bundle does not develop into a swirling pattern, as shown in Figure 2.15. This indicates that the swirling flow is created by a combined effect of the upstream pipe flow, the presence of the endplate ribs/rings and the misalignment between the endplate subchannels and the bundle subchannels. Figure 2.16 shows the velocity magnitude contour in the Y-Z plane across the bundle interface. Similarly to the entrance region, there exist large wakes after the endplate ribs and rings, especially in the BD2-4 subchannel.

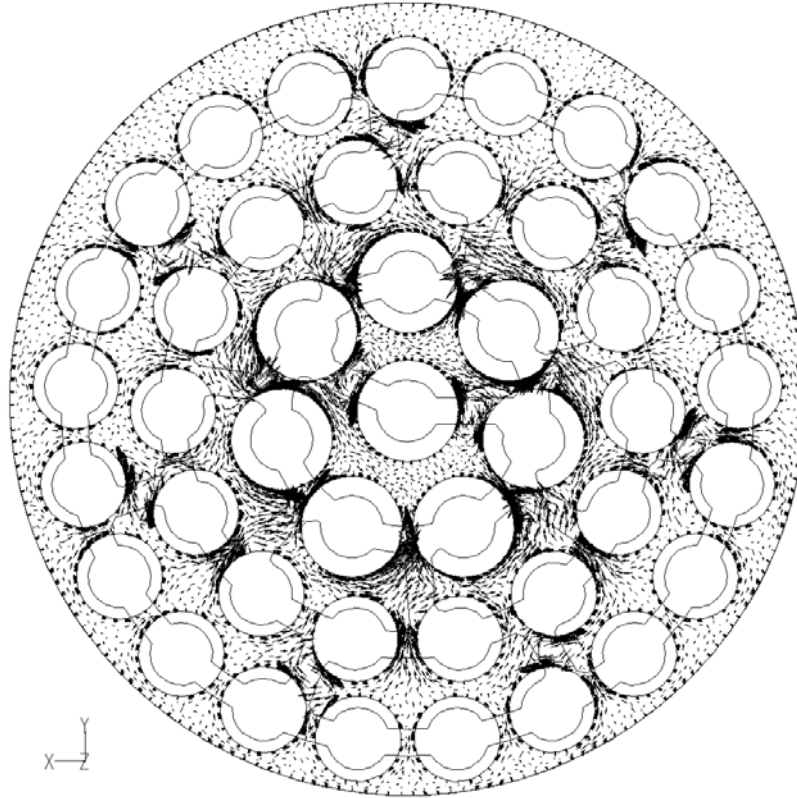


Figure 2.10 In-plane velocity vectors (15x scale) at location L1 of the inlet bundle ( $t=0.16$  s).

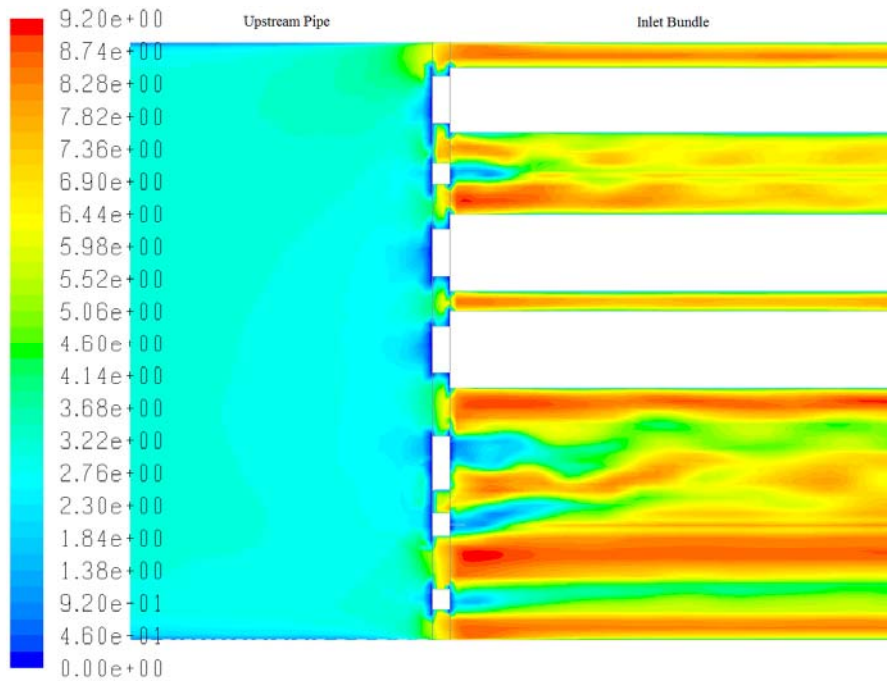


Figure 2.11 Velocity magnitude contour in the Y-Z plane at the entrance ( $t=0.16$  s).

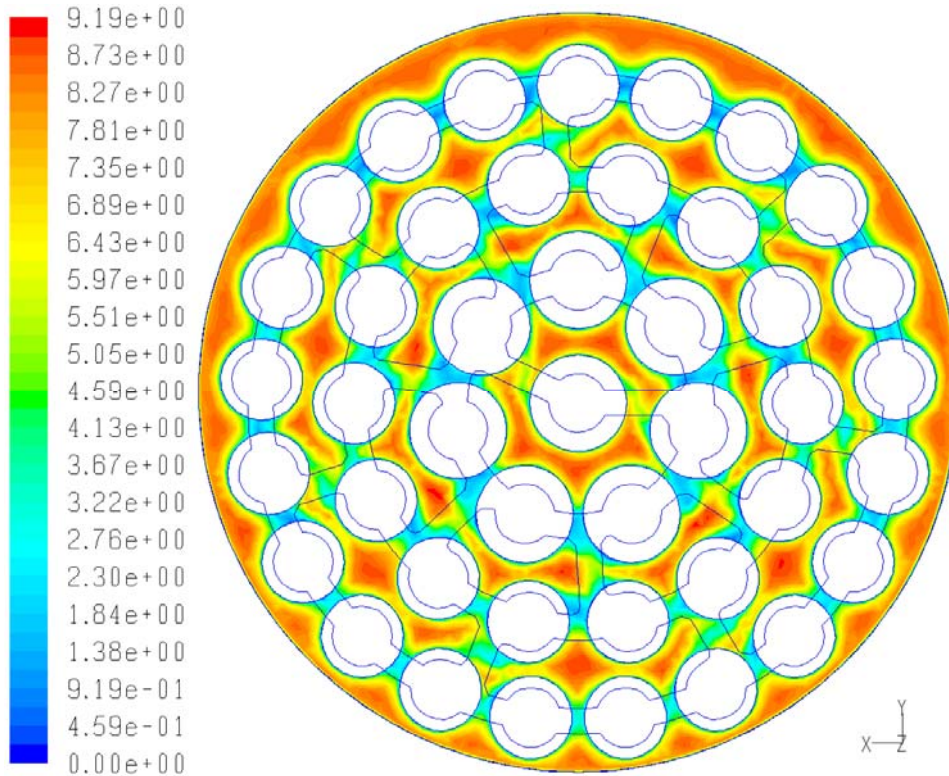


Figure 2.12 Velocity magnitude contour at location L1 of the inlet bundle ( $t=0.16$  s).

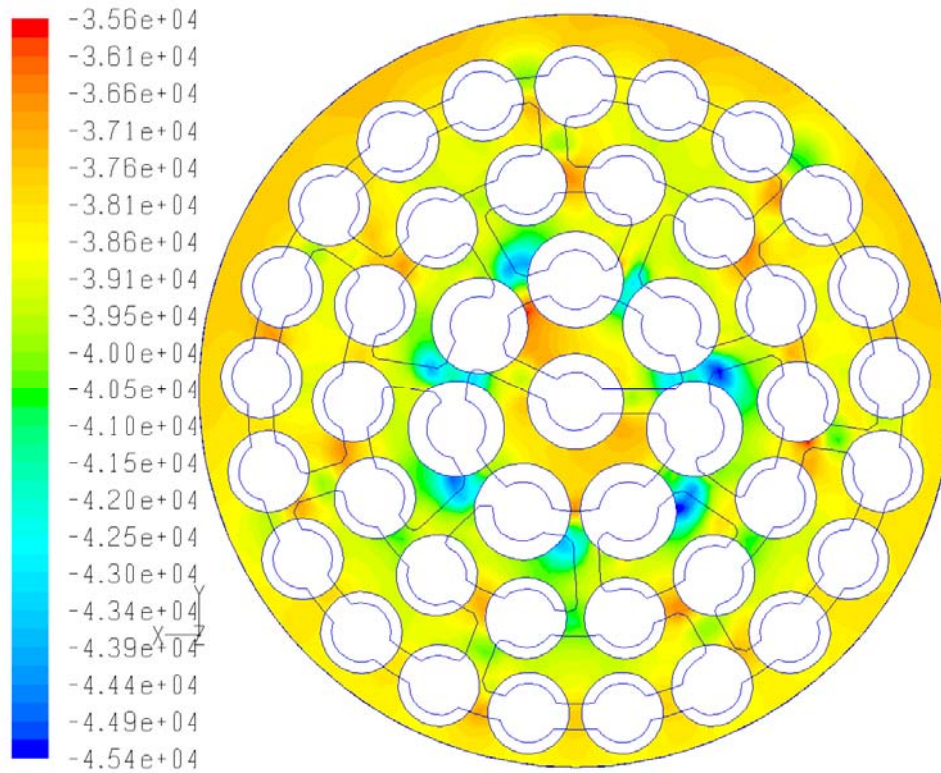


Figure 2.13 Static pressure contour at location L1 of the inlet bundle ( $t=0.16$  s).

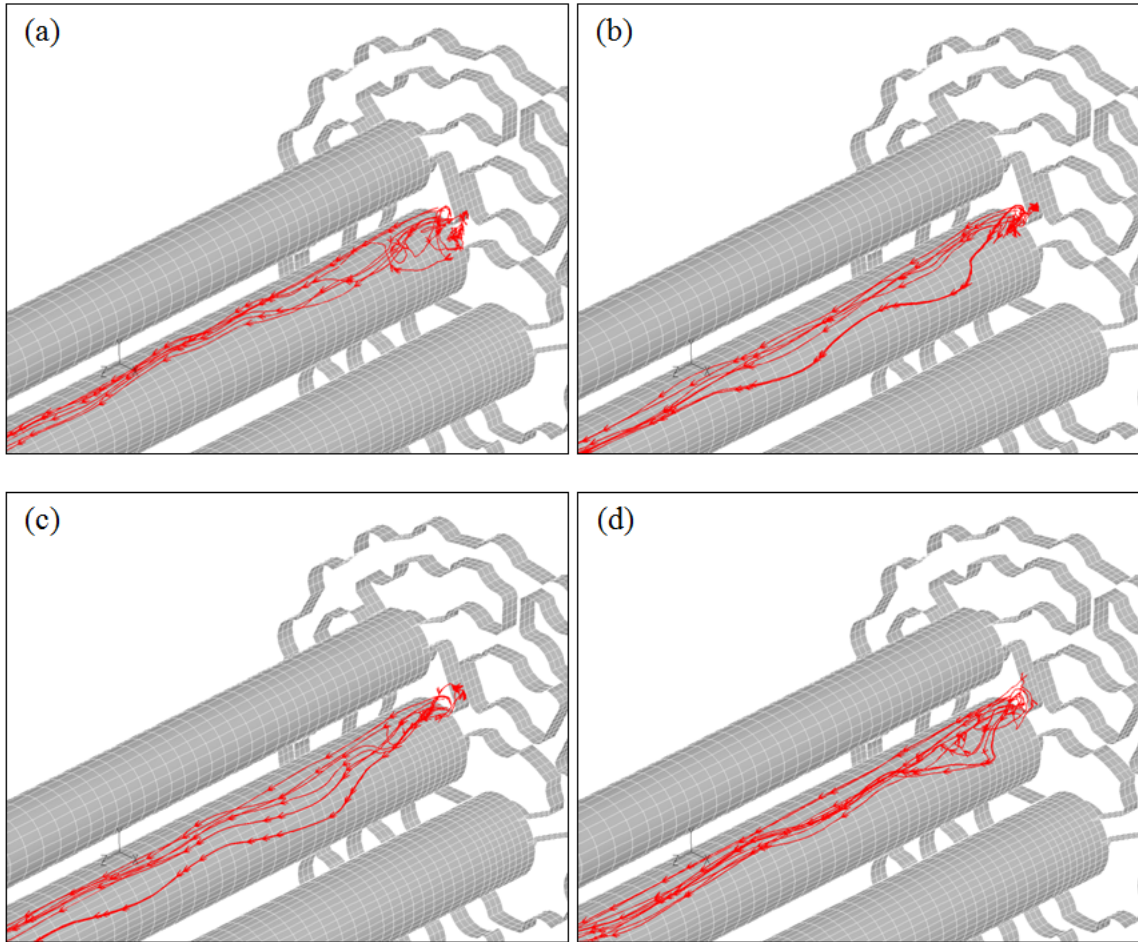


Figure 2.14 . Pathlines behind the endplate rib in the BD2-1 subchannel in the inlet bundle at different moments: (a)  $t=0.16$  s; (b)  $t=0.20$  s; (c)  $t=0.24$  s; (d)  $t=0.28$  s.

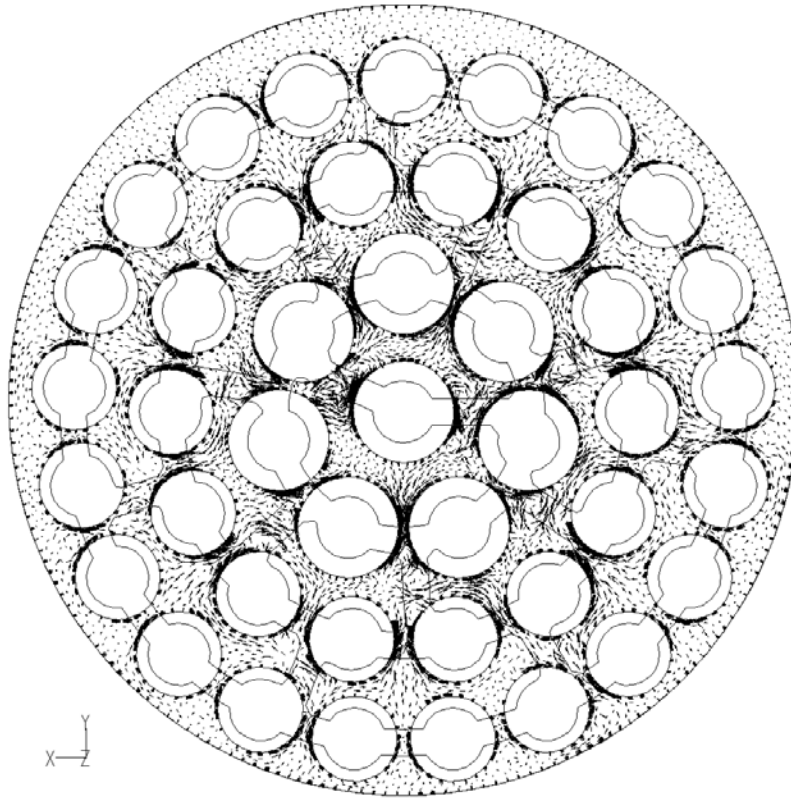


Figure 2.15 In-plane velocity vectors (15x scale) at location L1 of the second bundle ( $t=0.16$  s).

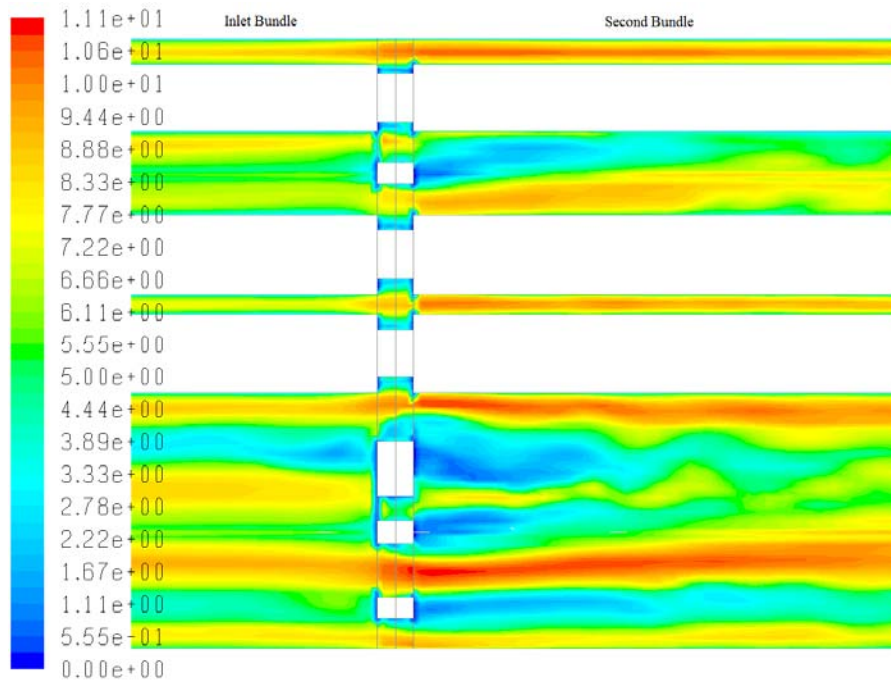


Figure 2.16 Velocity magnitude contour in the Y-Z plane at the bundle interface ( $t=0.16$  s).

### 2.3.2 Flow Development

Like any other confined flow in a slender channel, the bundle flow develops in the subchannels. Figure 2.17 and Figure 2.18 show the in-plane velocity vectors at multiple axial locations in the inlet bundle and the second, respectively. The locations are defined in Table 2.2. In the inlet bundle, the in-plane velocity is significant at locations close to the upstream endplate, such as L1, L2 and L3 in Figure 2.17. L3 corresponds to a distance of  $8.75 D_h$  from the endplate-fuel-element interface in the upstream end of the bundle. At location L5, which corresponds to  $31.25 D_h$ , the in-plane velocity becomes negligible compared to location L1, but the swirling trend still remains in the BD2 subchannels until location L7, which corresponds to  $53.75 D_h$ . The flow pattern is changed near the end of the inlet bundle due to the blockage of the endplate ribs/rings at the interface between two bundles. The flow in the second bundle, as shown in Figure 2.18, is different. Significant in-plane velocities can be seen after the endplates till location L4, but no swirling flow in the BD2 subchannels is seen. The velocity components on the centerline of three subchannels, BD1-1, BD2-1, and BD3-1 are plotted in Figure 2.19, Figure 2.20, and Figure 2.21, as well as the rate of change of these velocity components with respect to the axial coordinate. Dramatic changes occur at the entrance and the bundle interface for all velocity components. The rate of change of the velocity components are very high at the entrance and the bundle interface, but become negligible at the distance of about 1/3 bundle length after the upstream endplate for each bundle.

Figure 2.22 shows the static pressure distribution along the bundle axis on the centerline of subchannel BD1-1, BD2-1, and BD3-1. The viscous pressure drop per unit length is about 89 kPa/m, estimated using the linear part of the pressure curve between  $z = 0.1$  and  $0.4$ . This corresponds to a Darcy–Weisbach friction factor  $f_D = 0.03$  according to the

formula  $f_D = \left( \frac{2D_h}{\rho U^2} \right) \left( \frac{\Delta p}{\Delta z} \right)$ , where  $D_h = 0.008$  m;  $\rho = 1000$  kg/m<sup>3</sup>;  $U = 6.8$  m/s;  $\frac{\Delta p}{\Delta z} = 89$

kPa/m. This friction factor matches that of a smooth pipe with the Reynolds number used according to the Moody diagram (Finnemore and Franzini, 2001), which is expected to be the case.

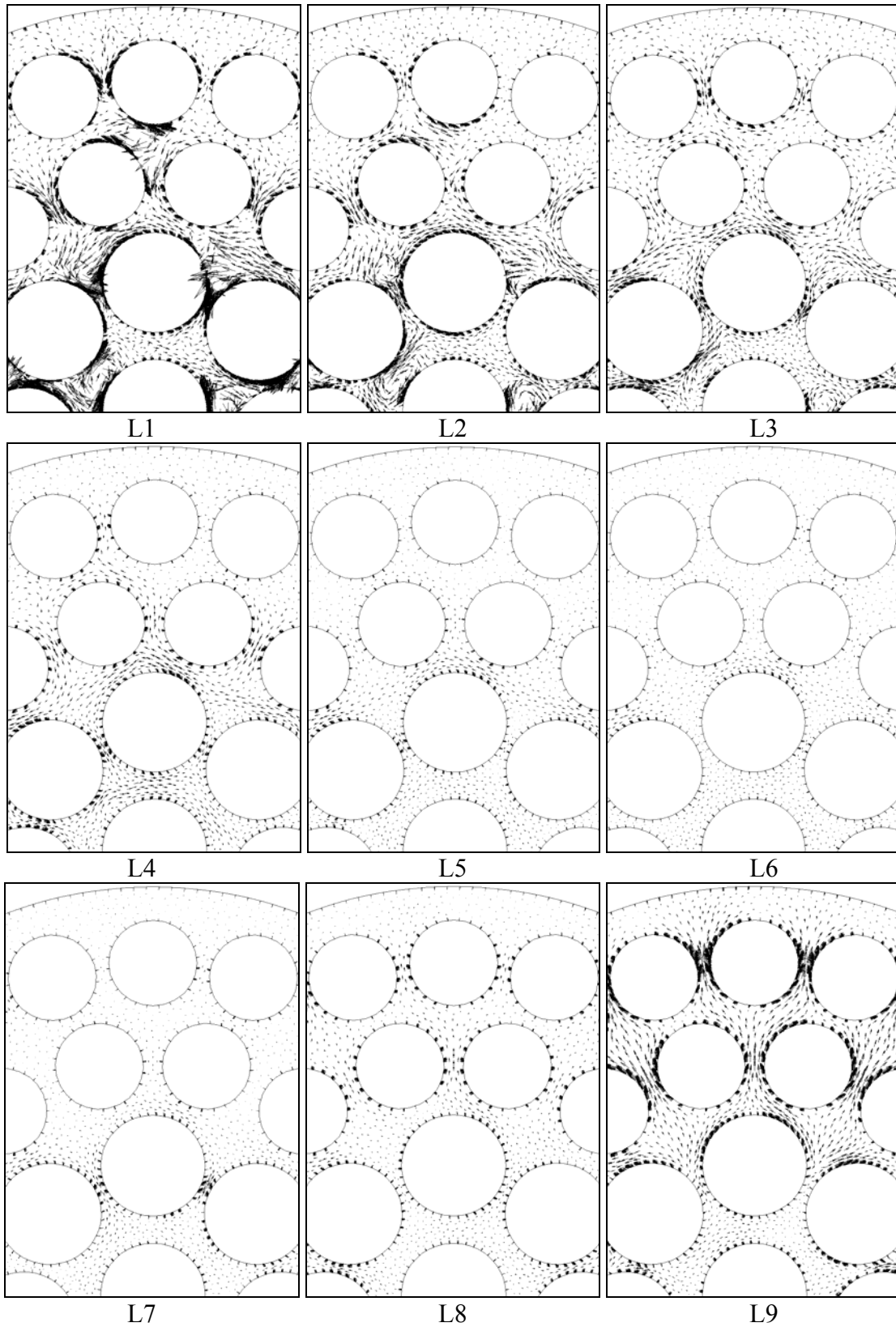


Figure 2.17 In-plane velocity vectors (15x scale) at different locations in the inlet bundle ( $t=0.16$  s).

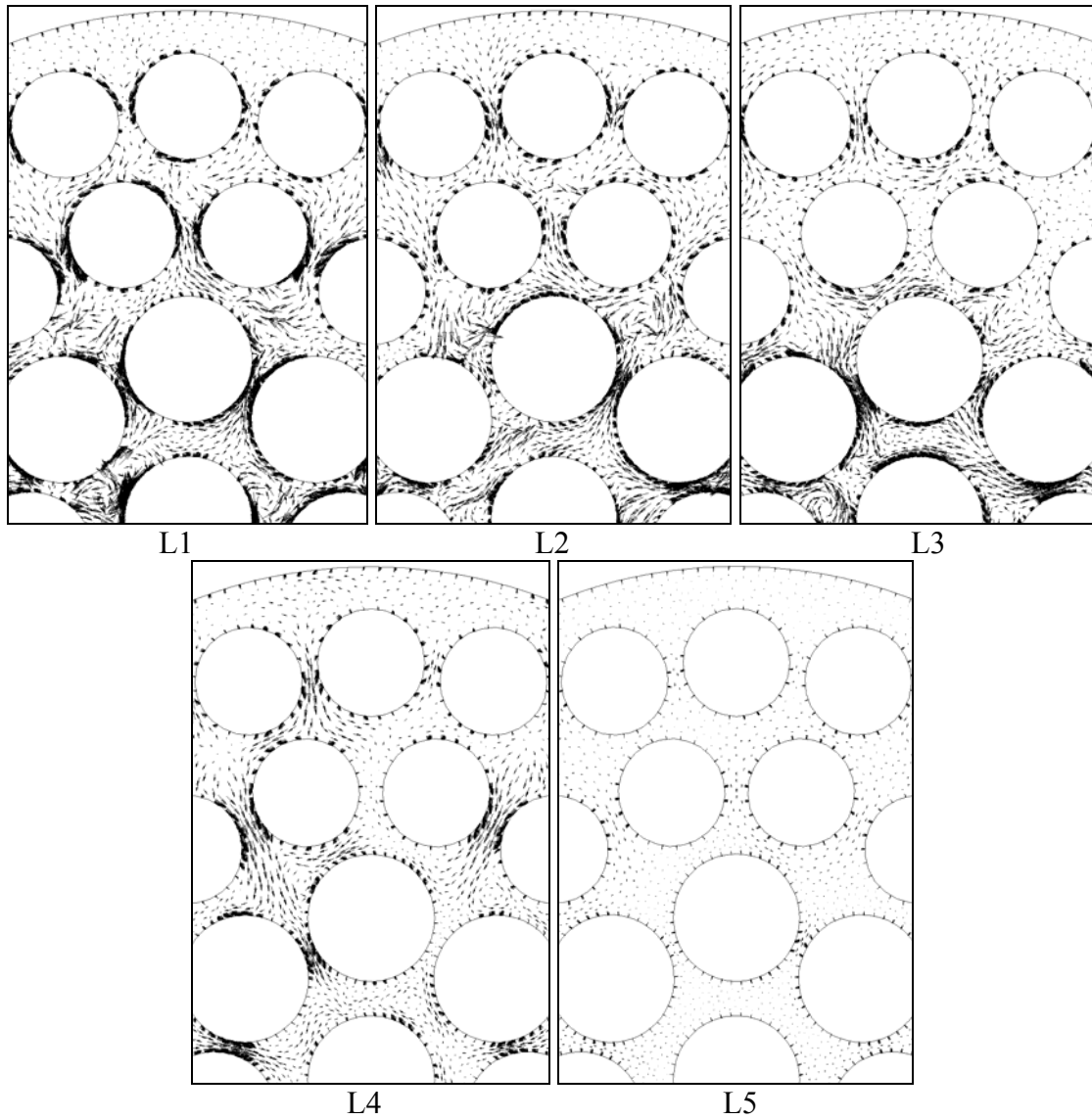


Figure 2.18 In-plane velocity vectors (15x scale) at different locations in the second bundle ( $t=0.16$  s).

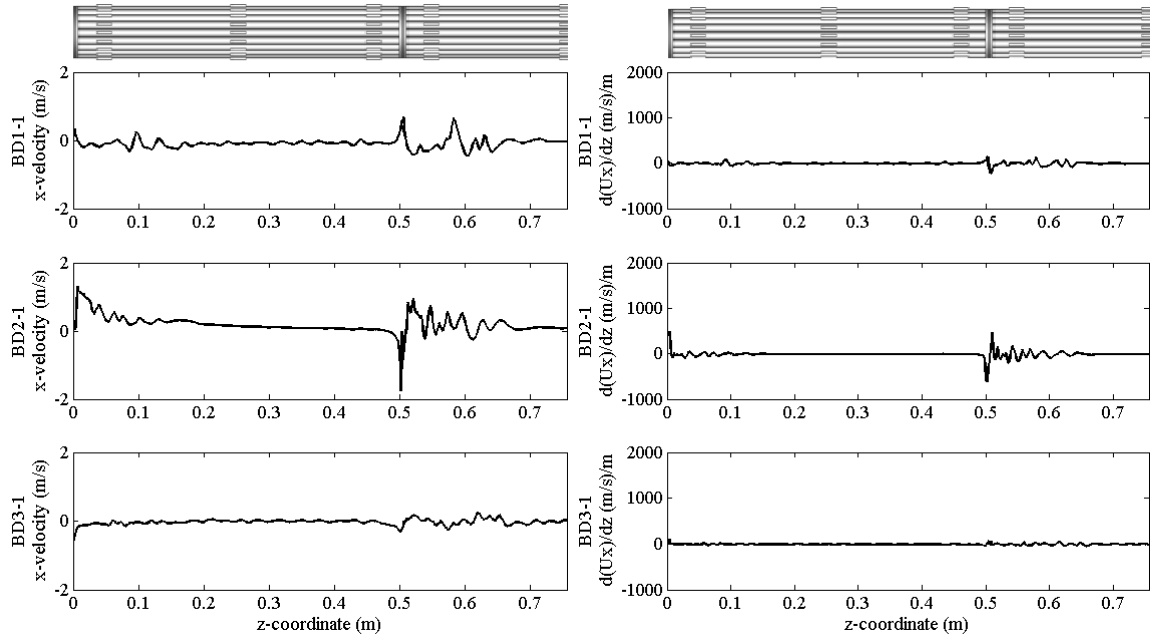


Figure 2.19 X-velocity (left) and its Z-derivative (right) on the centerline of three subchannels ( $t=0.16$  s).

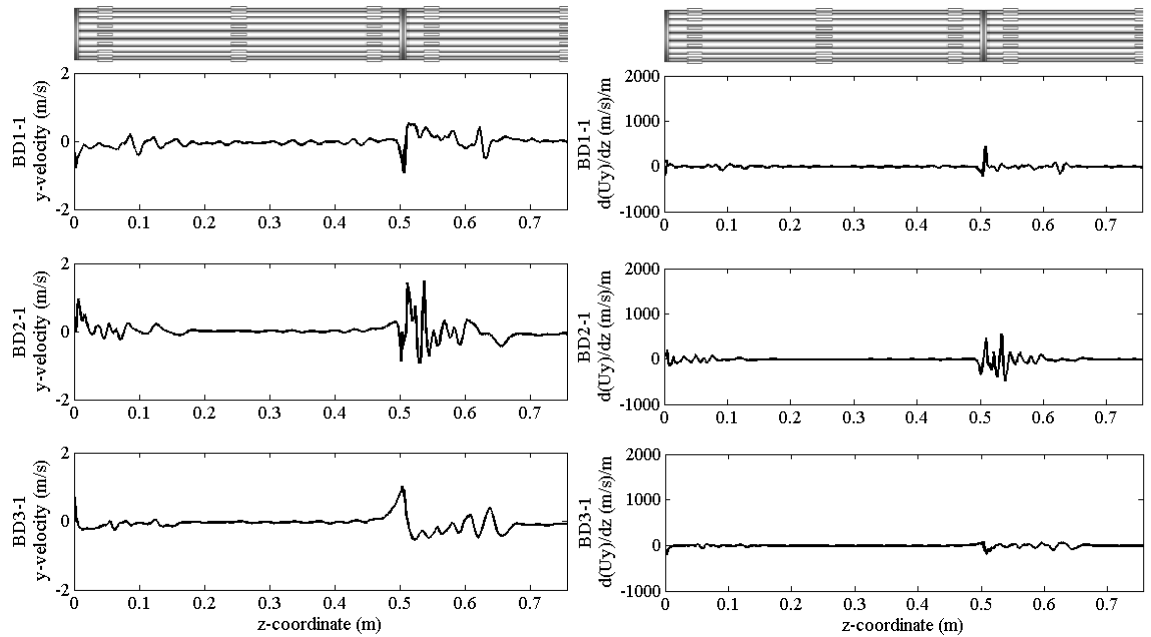


Figure 2.20 Y-velocity (left) and its Z-derivative (right) on the centerline of three subchannels ( $t=0.16$  s).

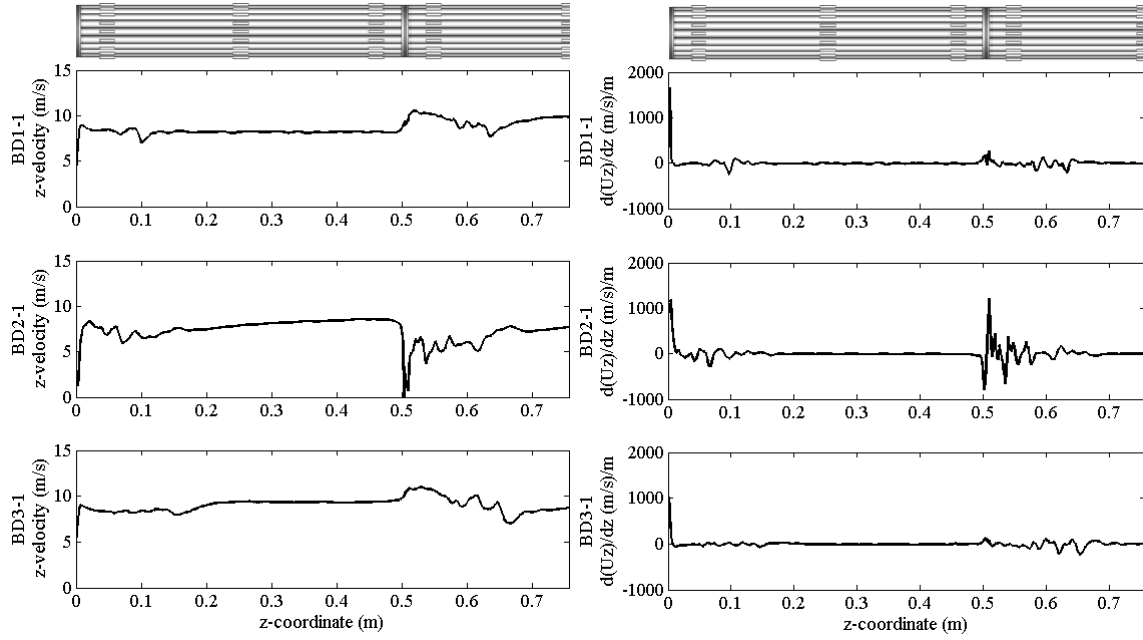


Figure 2.21 Z-velocity (left) and its Z-derivative (right) on the centerline of three subchannels ( $t=0.16$  s).

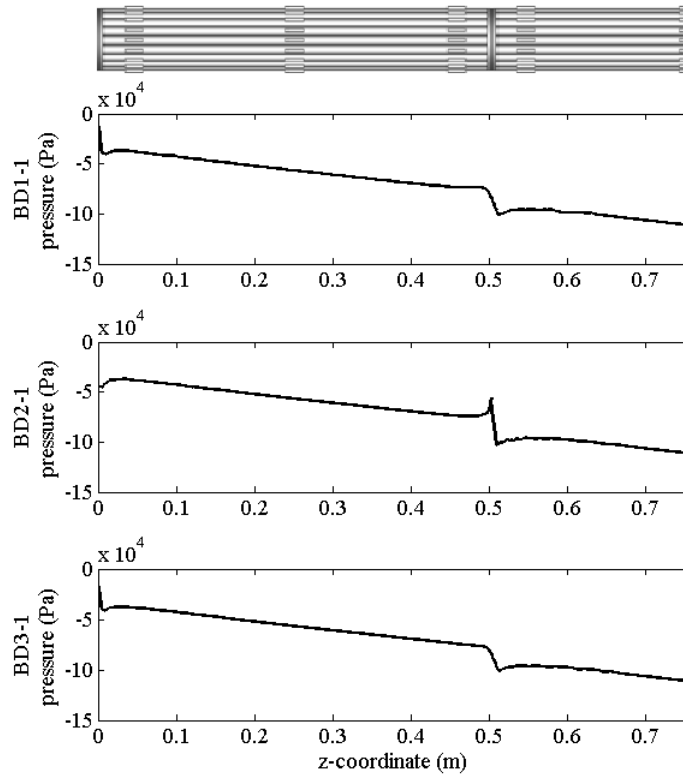


Figure 2.22 Static pressure on the centerline of three subchannels ( $t=0.16$  s).

### 2.3.3 Fluid Forces

Fluid forces can be obtained from the flow simulation results. Ideally the pressure field on the outer surface of the fuel elements and endplates at each time step are needed, but it is impractical in such a large model. The pressure calculation and data output operation dramatically reduce the overall computing speed of the parallel network. Numerical tests show that if a large amount of file operations are invoked, the solution is very slow so that a simulation of 1 second of the flow time will take three months to complete. Therefore, an alternative approach is used here. The fuel elements are divided into 10 segments and the pressure fields on these segments are integrated to find the fluid forces. The forces are output for vibration calculation. The lengths of the segments are not uniform. Shorter segments are used near the endplates and longer segments are used near the bundle midplane. The length of each segment is listed in Table 2.3. The total number of segments in a bundle is 430.

Table 2.3 Segment length.

Segment	length (mm)	Segment	length (mm)
1	10	6	110
2	20	7	70
3	40	8	40
4	70	9	20
5	110	10	10

The lift forces in the X- (horizontal) and Y- (vertical) directions are obtained on each segment. The segmental forces are summed together to obtain the overall X-force and Y-force on the inlet bundle. The X-force and Y-force, together with their PSD, are shown in Figure 2.23 and Figure 2.24, respectively. The X-force has a mean value of -0.76 N, and a fluctuation (deviation) of 0.49 N. The Y-force has a mean value of 0.0055 N and a fluctuation of 0.55 N. Spectrum of X-force shows that a large amount of vibration energy concentrates near 30 Hz and 183 Hz. A spectrum of Y-force shows that 18 Hz and 36 Hz are dominant frequencies, while some energy also concentrates around 195 Hz.

The X- and Y- forces are not uniformly distributed along the bundle longitudinal axis. The segment forces are divided by the length of the segment to approximate the distributed force at the center of the segment. The distributed forces are linearly interpolated and shown in Figure 2.25 and Figure 2.26. The figures show that the

distributed forces in both directions are small inside the bundle, but the mean value and fluctuation increase dramatically near the endplates.

When studying the low frequency fuel bundle motion, the unsteady moment of the fluid forces about the bundle centerline ( $Z$ -moment) is of special interest. This moment is calculated from the forces in the  $X$ - and  $Y$ - directions. There is an additional component of the  $Z$ -moment on each fuel element induced by the viscous friction of the flow circulating around the element, but its magnitude is of two orders of magnitude smaller than that induced by the lift forces. Therefore, this component is ignored. The  $Z$ -moment time history and its PSD are shown in Figure 2.27. The mean value of this moment is  $-0.15$  Nm and the fluctuation is  $0.004$  Nm. The PSD shows that the moment energy is mainly distributed in low frequencies. The axial distribution of the  $Z$ -moment is shown in Figure 2.28. Again, large mean and fluctuation are seen near the endplates. In the fully developed bundle flow region, the mean moment is almost zero and the fluctuation is very small.

To understand the contributions of unsteady  $Z$ -moment acting on individual fuel elements, the moment is calculated for fuel element (Rod) R1, R2, R21, R22, R35 and R36 as shown in Figure 2.2. Figure 2.29, Figure 2.30 and Figure 2.31 show the  $Z$ -moment on the above fuel elements on segment 1, 5 and 10, respectively. The frequency domain spectra are also shown in these figures. It can be seen that the  $Z$ -moment on segment 1 (the one near the upstream endplate) of these fuel elements varies fast. Predominant spikes appear around  $190$  Hz. On the contrary, the moment on the segment inside the bundle (segment 5) is slow varying and the oscillation amplitude is much smaller compared to that of segment 1. At the downstream end (segment 10), the strength of the  $Z$ -moment fluctuation becomes strong again, but the energy distribution is broad band.

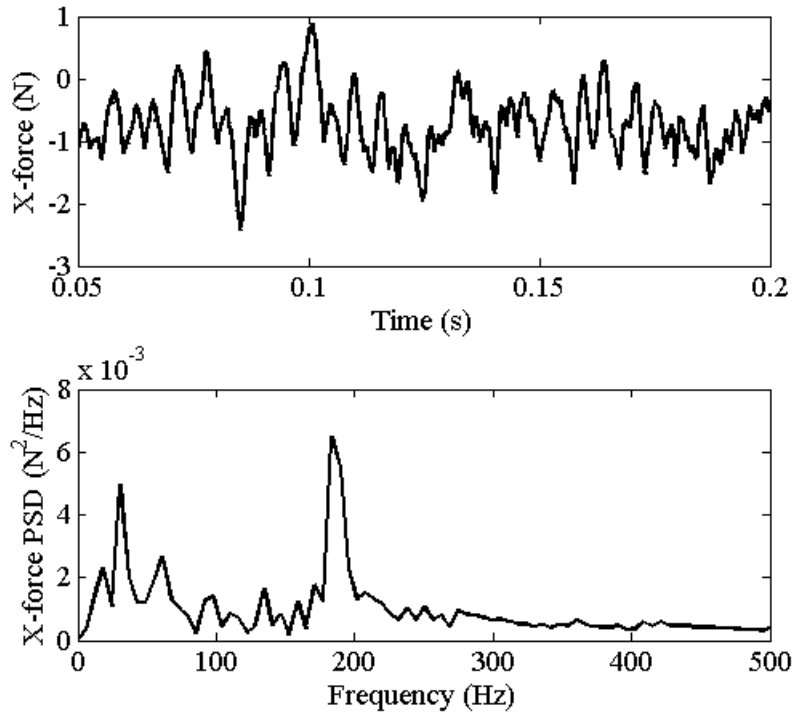


Figure 2.23 Time history and PSD of the overall X-force on all fuel elements of the inlet bundle.

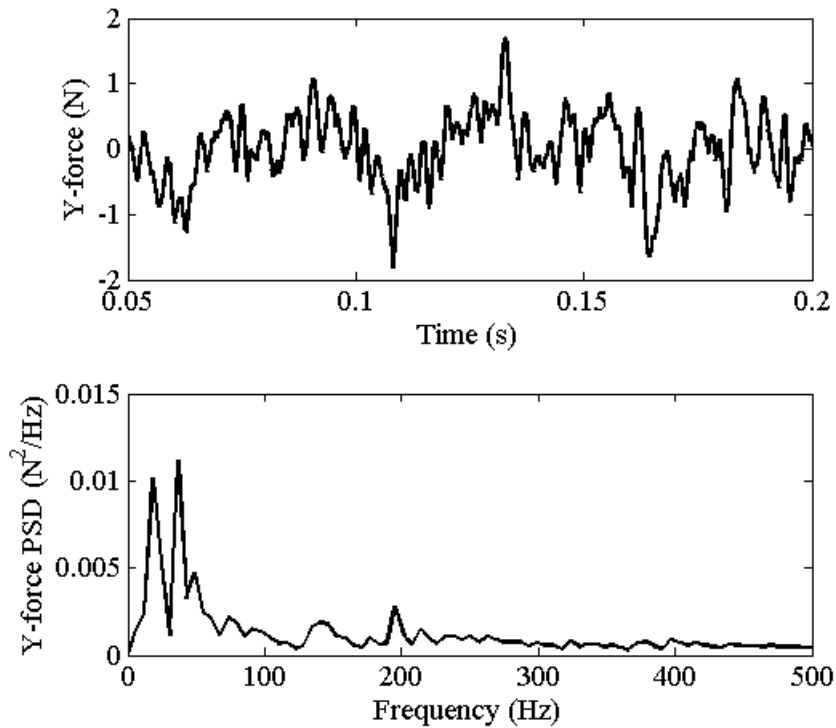


Figure 2.24 Time history and PSD of the overall Y-force on all fuel elements of the inlet bundle.

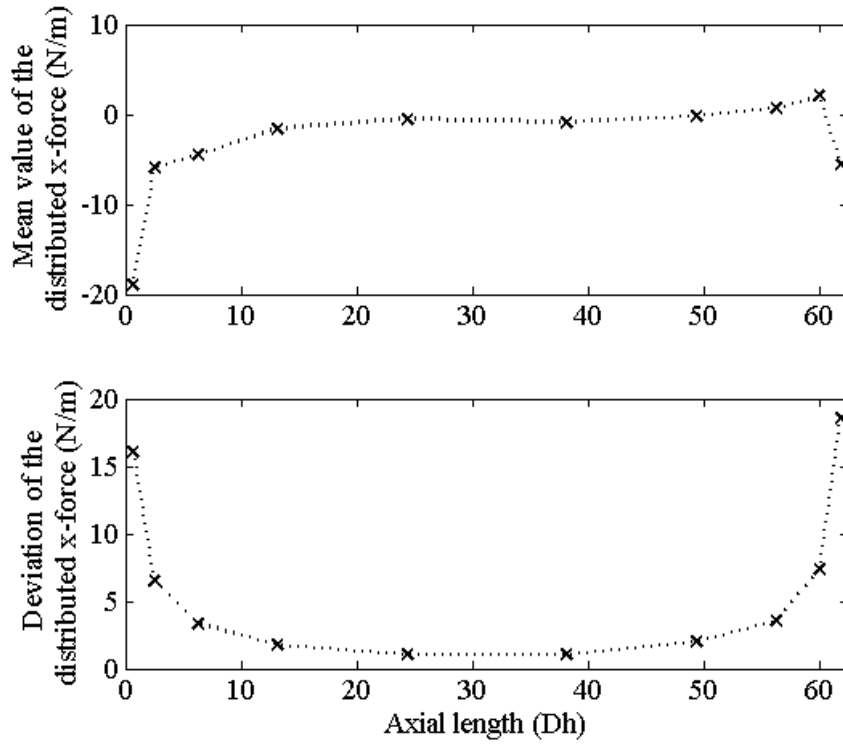


Figure 2.25 Distributed Y-force on all fuel elements of the inlet bundle.

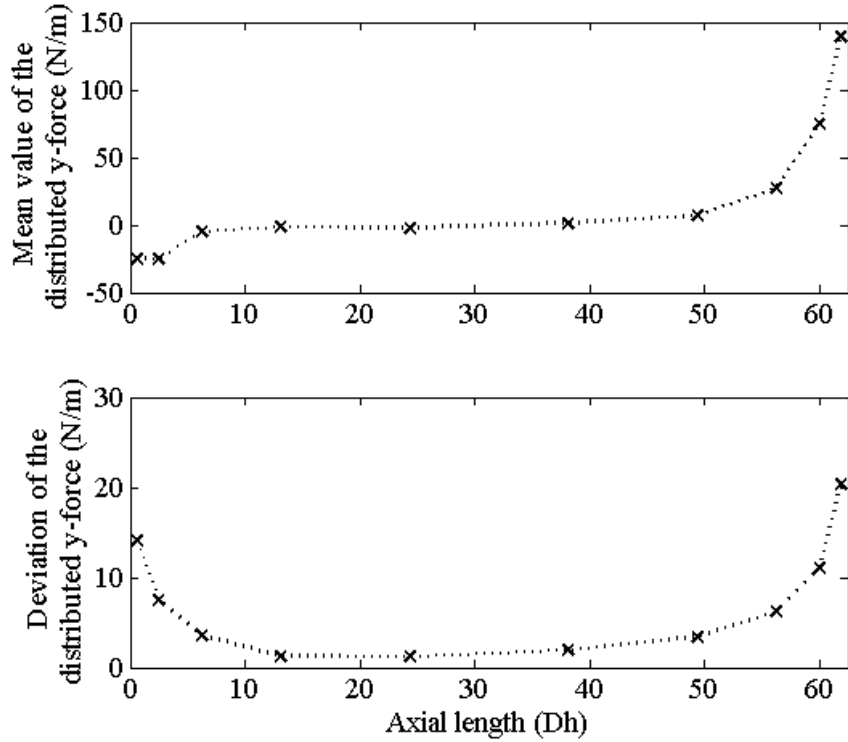


Figure 2.26 Distributed Y-force on all fuel elements of the inlet bundle.

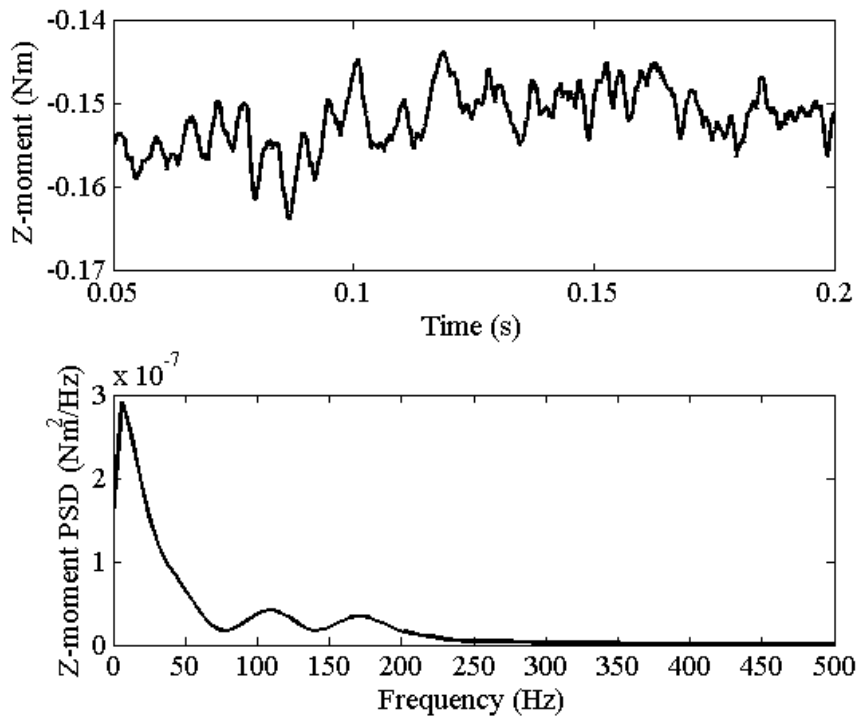


Figure 2.27 Time history and PSD of the overall Z-moment on all fuel elements of the inlet bundle.

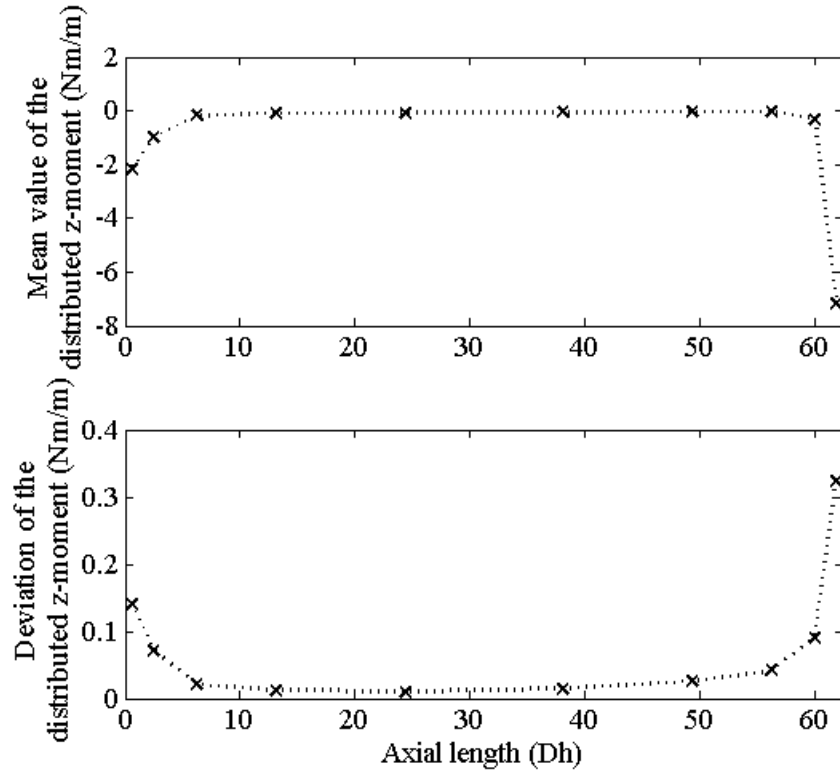


Figure 2.28 Distributed Z-moment on all fuel elements of the inlet bundle.

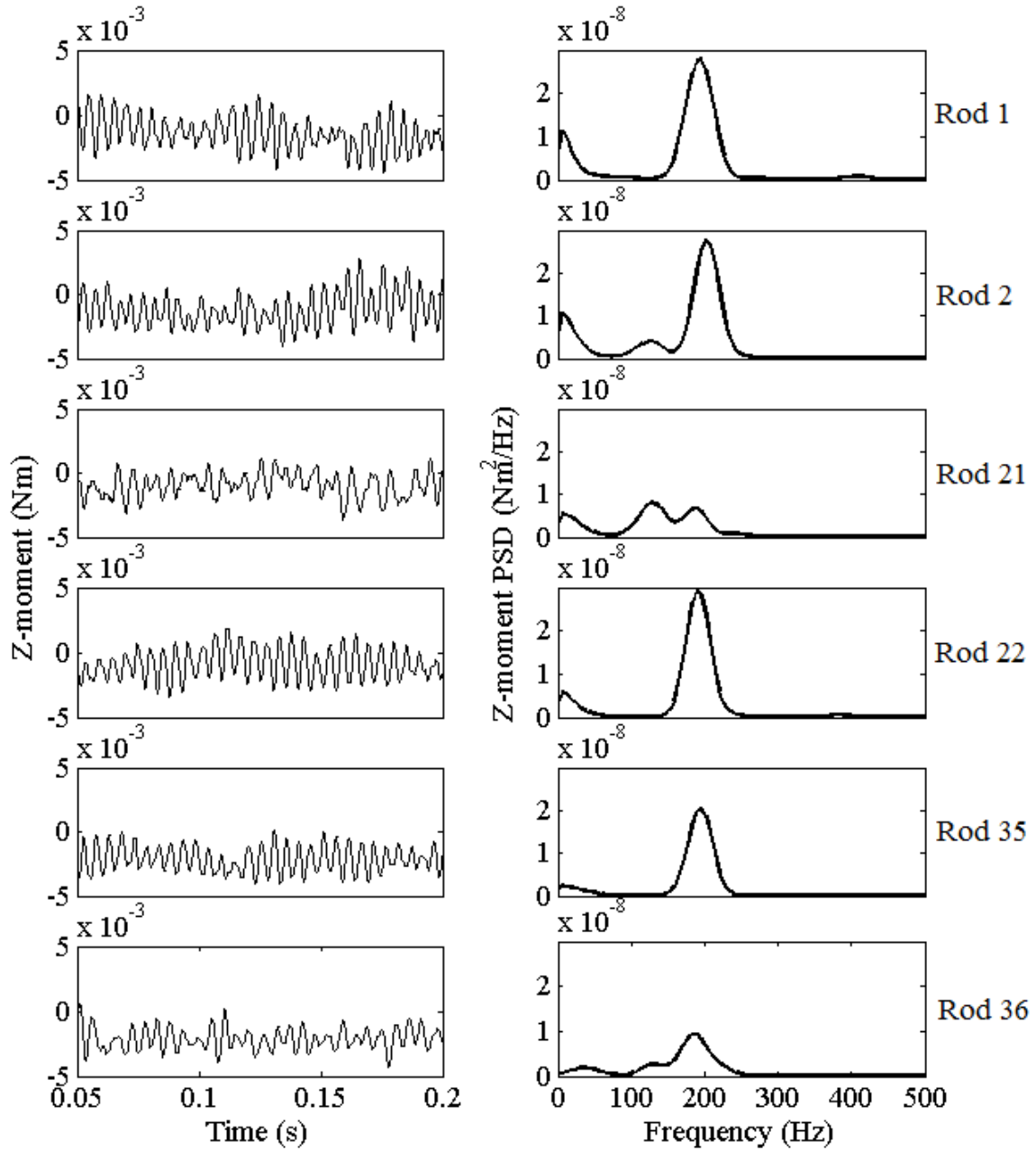


Figure 2.29 Time history and PSD of distributed Z-moment on segment 1 on selected fuel elements of the inlet bundle.

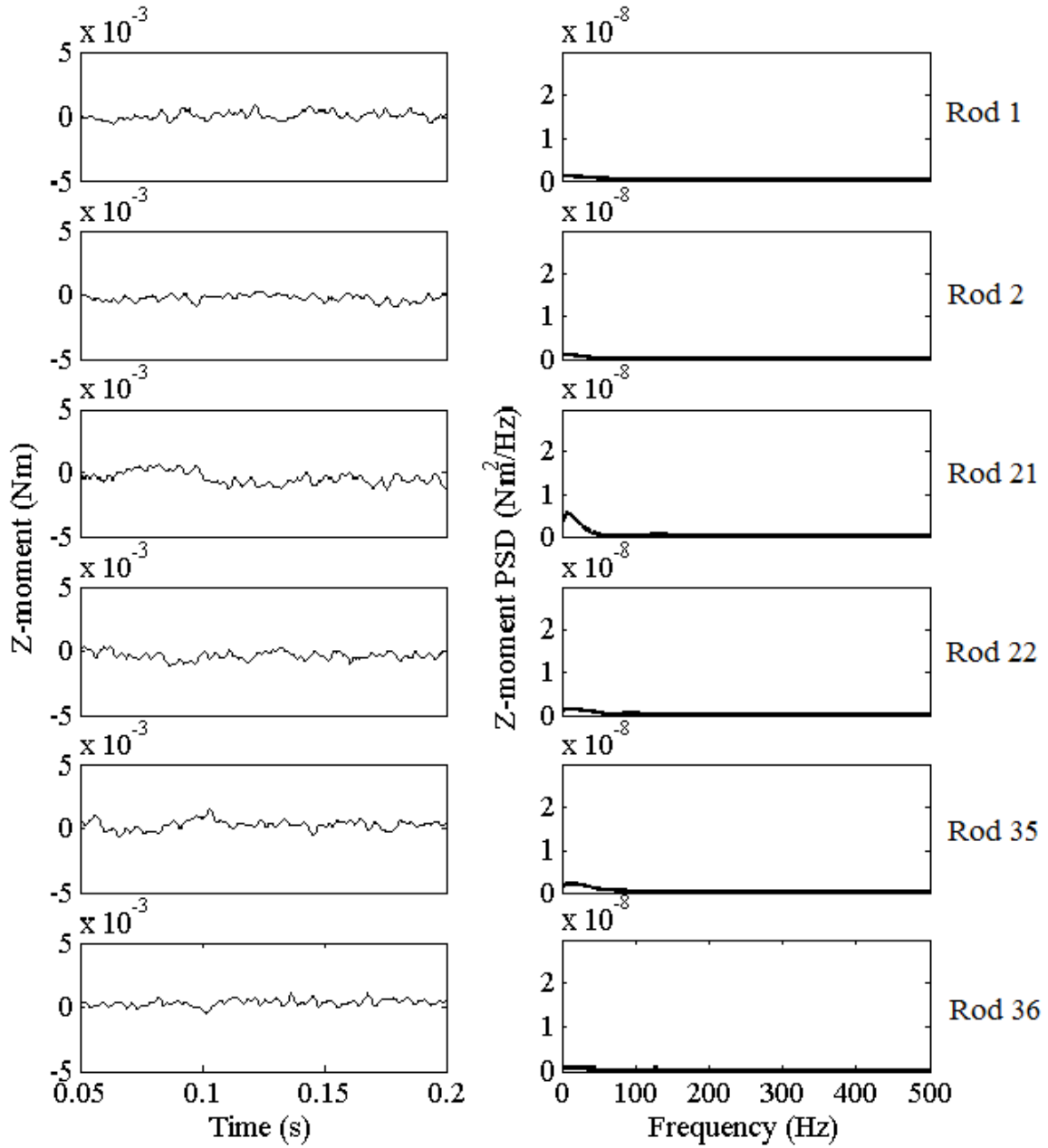


Figure 2.30 Time history and PSD of distributed Z-moment on segment 5 on selected fuel elements of the inlet bundle.

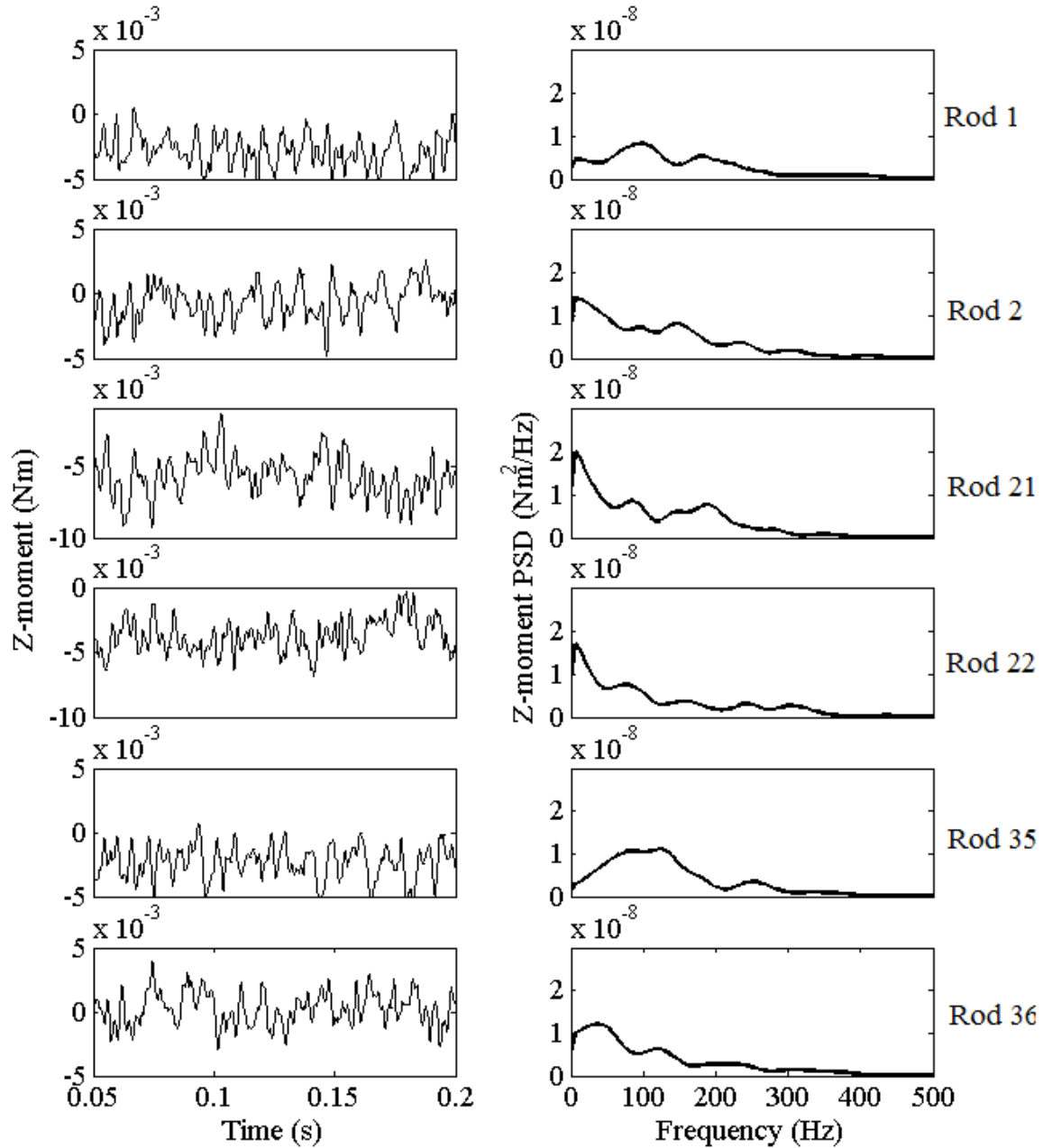


Figure 2.31 Time history and PSD of distributed Z-moment on segment 10 on selected fuel elements of the inlet bundle.

In addition to the fluid forces on the fuel elements, the forces on the two endplates of the inlet bundle are also significant. The X-force, Y-force and the Z-moment about the bundle centerline are shown in Figure 2.32, Figure 2.33 and Figure 2.34 respectively. These dynamic loads must be considered in a vibration model of the bundle.

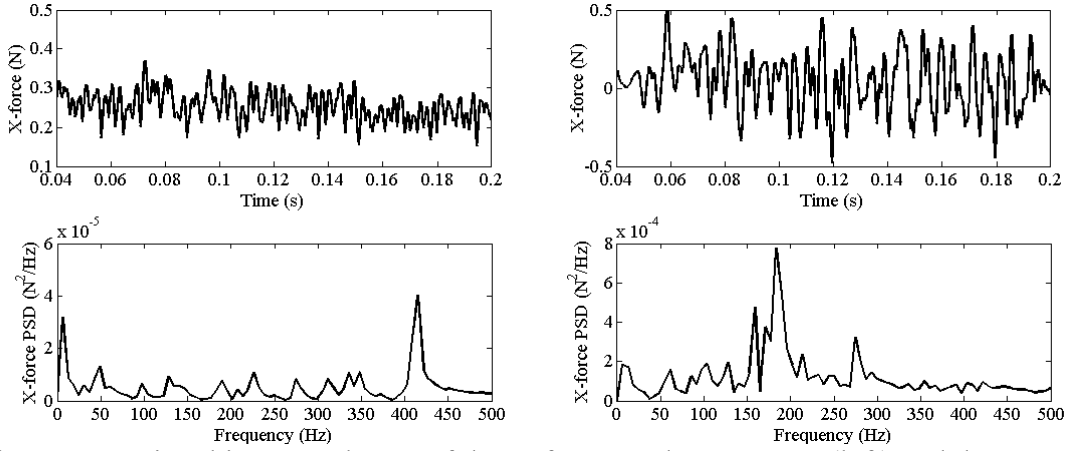


Figure 2.32 Time history and PSD of the X-force on the upstream (left) and downstream (right) endplates of the inlet bundle.

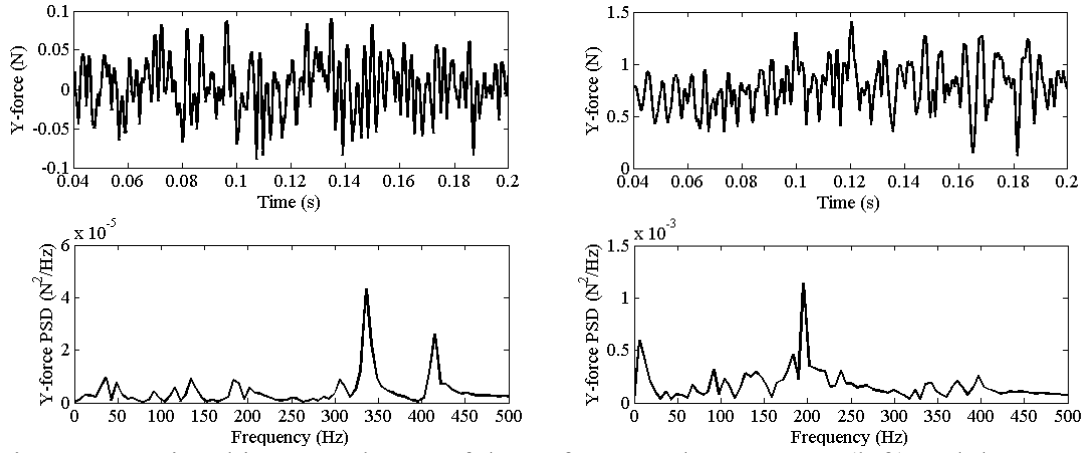


Figure 2.33 Time history and PSD of the Y-force on the upstream (left) and downstream (right) endplates of the inlet bundle.

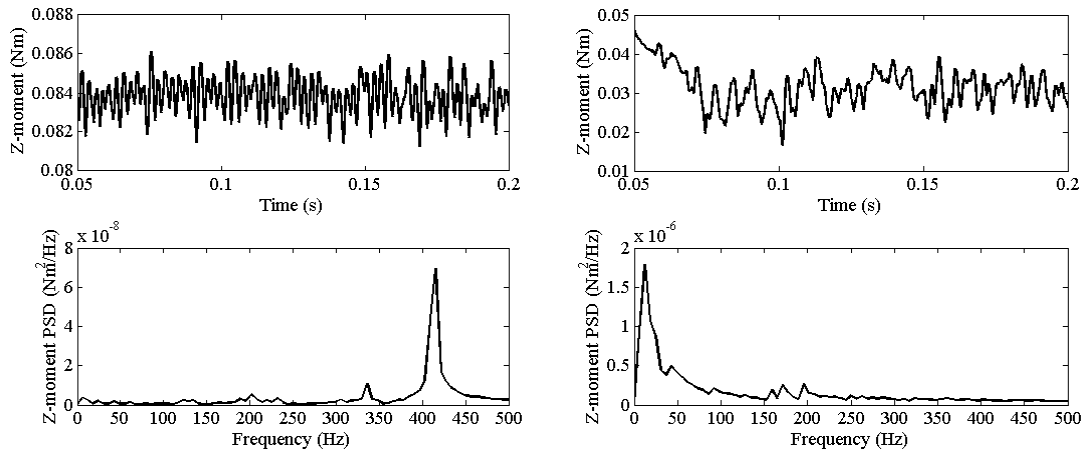


Figure 2.34 Time history and PSD of the Z-moment on the upstream (left) and downstream (right) endplates of the inlet bundle.

The longitudinal drag force is regarded as steady and uniformly distributed. The influence of the longitudinal drag is incorporated to the bending of the fuel elements by including  $p$ -delta effect, a destabilization effect induced by the axial compressive load (Lindeburg and Baradar, 2001). The value of the drag force is obtained using empirical friction equations and will be described in Chapter 4.

## 2.4 Experimental Validation

### 2.4.1 Experimental Setup

To validate the simulation results, the wall pressure fluctuation on the inner surface of the tube was measured. The measurement was conducted on the experimental setup shown in Figure 2.35. It was found that a centrifugal pump produced significant acoustic pressure pulsation in the closed loop. A large tank was used instead to provide the head for creating the flow in the test section. Due to the limit of the tank capacity, the maximum volume flow rate that can be achieved is  $35 \text{ m}^3/\text{h}$ . The flow rate decreases as the water is discharged to the lower-head reservoir. It was found that within 3 seconds, the loss of the water head in the tank is about 1 % compared to that at the full capacity. It takes 2 seconds from the moment of opening the main valve to achieve a fully developed regime in the fuel bundle area. To balance the needs between a longer record length in signal processing and a slowly varying flow rate, the data record is limited to within 2 seconds. In the measurements, the mean flow velocity in the test chamber was controlled to be around  $1 \text{ m/s}$ , which yields a global Reynolds number of 18000 at the bundle upstream.

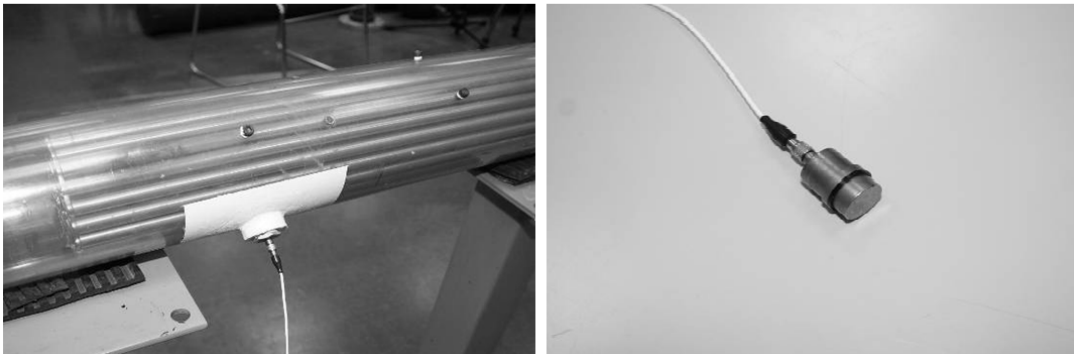
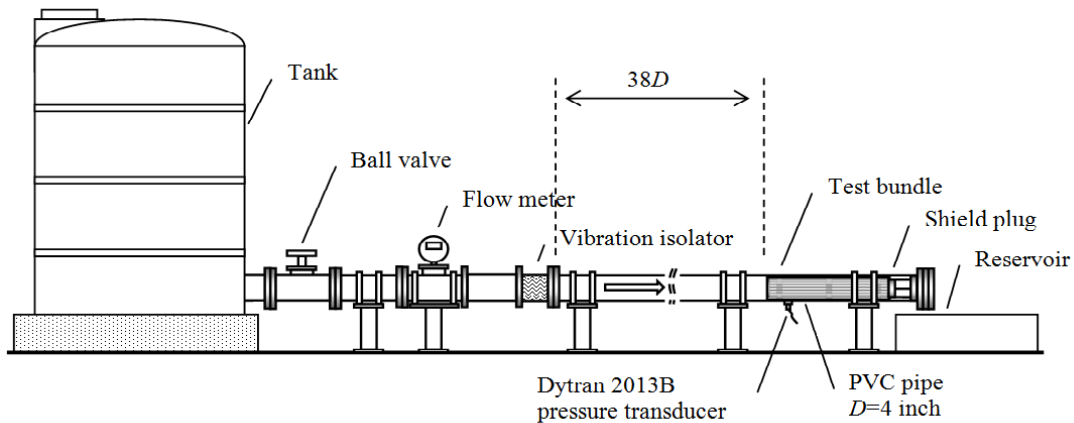


Figure 2.35 Experimental setup.

A Dytran 2130B hydrophone was flush mounted near the bottom of the tube. The axial location of the sensor was 80 mm in the downstream of the inlet endplate of the bundle. This sensor contains a piezoelectric sensing element and can only measure the varying pressure. The sensitivity of the hydrophone is 0.276 mV/Pa. The full measuring range is 172.4 kPa and the resolution is 0.17 Pa. A 16-bit data acquisition system and a computer were used to record the voltage output from the pressure transducer. The resolution of the data acquisition system is 0.03 mV, which corresponds to 0.1 Pa. A sampling rate of 97.7 kHz was used, and the duration of each measurement is 1.34 seconds. There was no aliasing problem with this sampling rate, because the measured signal does not contain any significant frequency component in the range higher than 10 kHz.

#### 2.4.2 Wall Pressure Measurement for Pipe Flow

Structure-borne and water-borne noises were present in the pressure signals. These noises were reduced by installing vibration isolators, yet they were not completely eliminated. To evaluate the background noise in this hydraulic system, the wall pressure fluctuation and tube accelerations were measured with a mean flow velocity of 1 m/s before the simulated bundle was inserted. The measured wall pressure fluctuation and its nondimensionalized PSD is shown in Figure 2.36 and compared to a wall pressure measurement of turbulent pipe flow from Clinch (1969). The horizontal axis is the reduced frequency  $fD/U$ , where  $f$  is frequency in Hz; tube diameter  $D = 0.1016$  m and the main flow velocity  $U = 1$  m/s. The vertical axis is the wall pressure PSD normalized to  $\rho^2 U^3 D$ , where  $\rho$  is the water density.

#### 2.4.3 Wall Pressure Measurement for Bundle Flow

The bundle flow measurements were repeated five times for the desired water level in the tank. Although the water level drops slowly during a measurement, the variations of pressure were picked up by the pressure transducer. As a result, a slowly varying mean appears in the recorded signals. During the tests, low frequency surface waves in the tank were observed. This signal was also detected by the pressure transducer. To remove the slowly varying mean and the surface wave noise, a high pass digital filter with a cut-off

frequency of 4 Hz was applied. The filtered signals for all the measurements were then fed to a computer code, where the averaged one-sided power spectral density (PSD) is calculated using Welch's modified periodogram method (Oppenheim and Schaffer, 1975). Figure 2.37 shows the time domain signals and their PSDs of the five tests.

The computational model is solved under the same flow condition ( $Re = 18000$ ). The mesh was slightly modified to reflect a large boundary layer thickness. The smoothed wall pressure PSD of the simulation result is compared in Figure 2.38 with that of the experimental results. The simulation result is generally higher than the measurements with a factor of 2 ~ 3. This indicates that the large eddy simulation may overly predict the pressure fluctuation. However, the PSD curves from the numerical simulation and averaged experimental data bear the same trend.

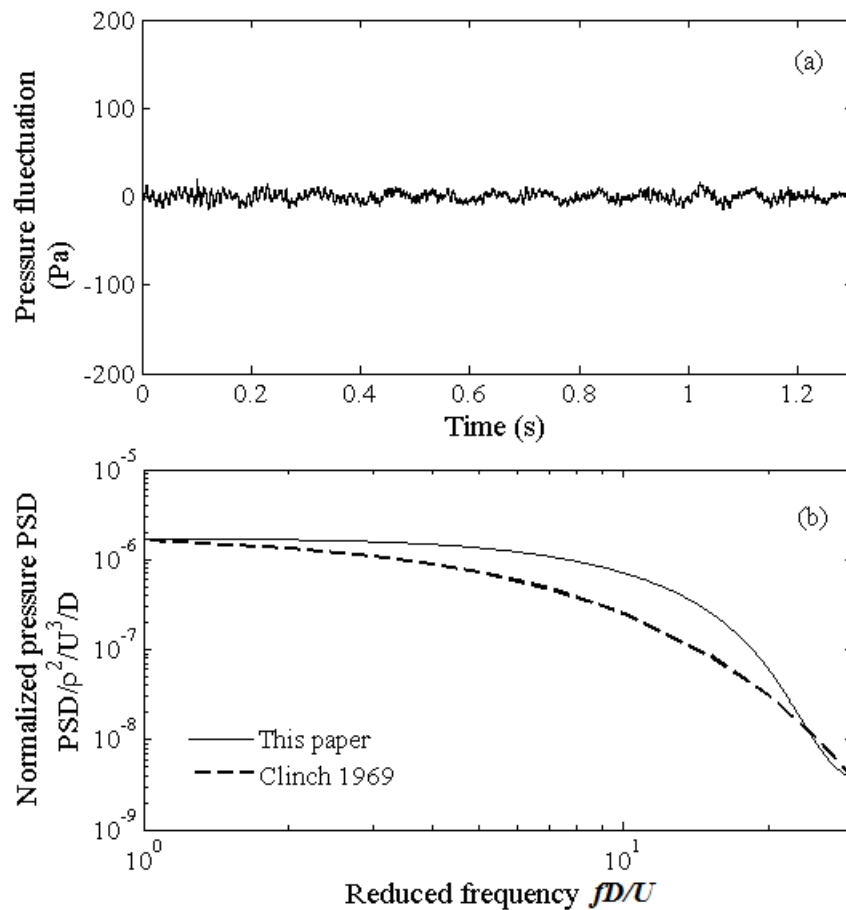


Figure 2.36 Wall pressure of the pipe flow without simulated bundle: (a) time domain signal; and (b) the smoothed normalized PSD.

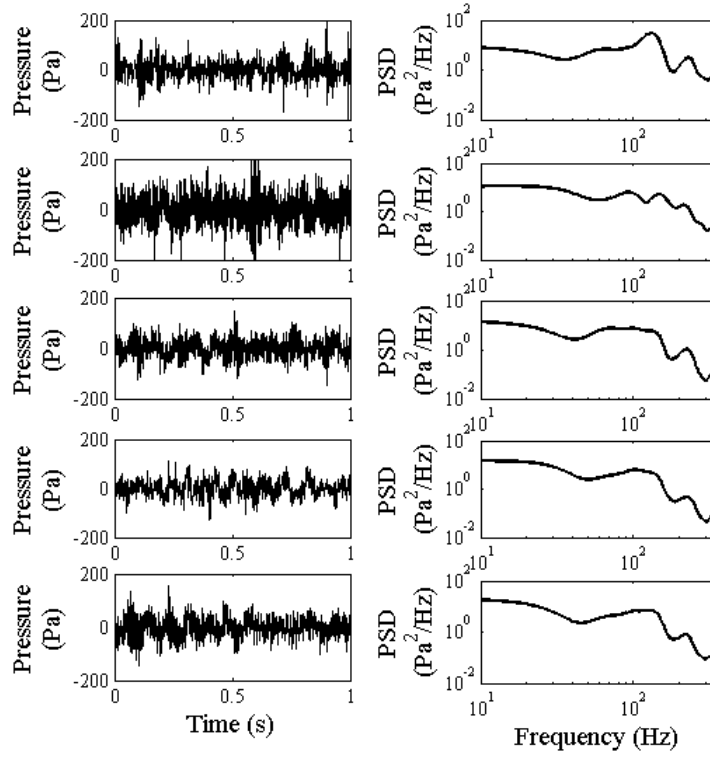


Figure 2.37 Five measurements of wall pressure fluctuations and their PSDs.

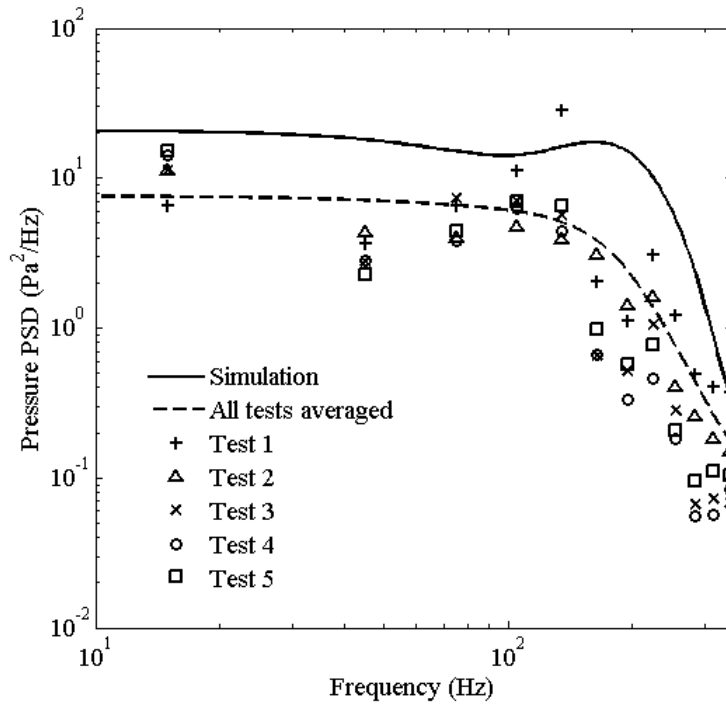


Figure 2.38 Comparison of the smoothed wall pressure PSD between experiment and simulation.

## 2.5 Summary of the Chapter

In this chapter, a three-dimensional flow model including the upstream pipe, the inlet bundle and a half of the second bundle was modeled and solved using large eddy simulation.

The numerical results showed that the abrupt change of flow channel and the presence of the endplate at the inlet of the bundle string introduced unstable vortices. Transport of these vortices produced unsteady forces on the fuel bundle. The misalignment between the endplate subchannels and the bundle subchannels introduced a swirling flow with a preferred direction inside the bundle. This swirling flow was also unsteady. After entering the bundle, the flow developed quickly to reach full development. The fully developed flow was disturbed again at the downstream endplate. The highest velocity change was found to occur at the downstream endplate.

The fuel elements in the inlet bundle were divided into a number of segments and fluid forces were obtained on each segment. The segmented model provided an efficient and practical measure of the force distribution along the bundle. It was found that fluid forces near the upstream and downstream endplates were significant while the fully developed flow in the middle of the bundle relatively produced little force. Time history of the distributed fluid forces was obtained. They will be used as excitations to calculate the bundle response in Chapter 4.

Experiments were conducted to measure the wall pressure on the pressure tube within the bundle region. The measured wall pressure was compared to simulation results, and a reasonable match was found.

## CHAPTER 3 STRUCTURAL MODEL

This chapter presents the structural modeling of the simulated fuel bundle. The bundle is discretized using two types of finite elements. The fuel elements are modeled using beam elements and the endplates are modeled using thick plate elements. Experiments are done to validate the finite element model.

Section 3.1 presents the finite element modeling of the fuel elements. Section 3.2 presents the modeling of the endplates. Section 3.3 presents the procedure of joining the endplates and the fuel elements. Section 3.4 presents the modeling of fuel bundles and the solution of the free vibration of a fuel bundle.

### 3.1 Fuel Elements

In the simulation fuel bundle, a fuel element is a solid circular beam with a length-to-radius ratio greater than 38. The Euler-Bernoulli beam theory (Przemeniecki 1968; Meirovitch, 2001) is suitable for modeling such a slender structure. In this section, a three-node three-dimensional Euler-Bernoulli beam element, as shown in Figure 3.1, with torsion is developed. The finite element procedure is briefly described here.

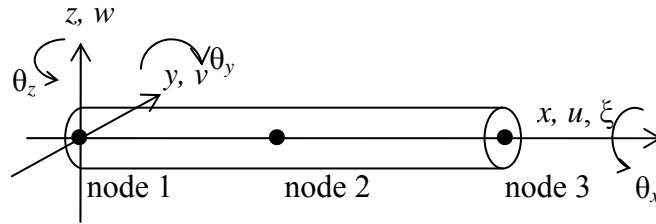


Figure 3.1 The three-node Euler-Bernoulli beam element.

The Euler-Bernoulli beam theory states that the cross section of the beam remains undeformed and perpendicular to the neutral axis after deformation. The three dimensional version of the theory can be expressed as below

$$\begin{aligned}
 u(x, y, z, t) &= u_o(x, t) - y\theta_z(x, t) + z\theta_y(x, t); \\
 v(x, y, z, t) &= v_o(x, t) - z\theta_x(x, t); \\
 w(x, y, z, t) &= w_o(x, t) + y\theta_x(x, t);
 \end{aligned}
 \tag{3.1}$$



$$\mathbf{u} = \mathbf{D}(\xi) \begin{bmatrix} \mathbf{D}(\xi_1) \\ \mathbf{D}(\xi_2) \\ \mathbf{D}(\xi_3) \end{bmatrix}^{-1} \bar{\mathbf{u}} = \mathbf{N}(\xi) \bar{\mathbf{u}}. \quad (3.3)$$

where  $\bar{\mathbf{u}} = \{\bar{\mathbf{u}}_1 \ \bar{\mathbf{u}}_2 \ \bar{\mathbf{u}}_3\}^T$ ;  $\xi_1$ ,  $\xi_2$  and  $\xi_3$  are the axial locations of node 1, 2 and 3 in terms of the local coordinate  $\xi$ .

The kinetic energy of the element can be expressed as

$$\begin{aligned} T_e &= \int_V \frac{\rho_s}{2} (\dot{u}^2 + \dot{v}^2 + \dot{w}^2) dV \\ &= \frac{\rho_s}{2} \int_V \mathbf{u}^T \mathbf{H}_m \mathbf{u} dV = \frac{\rho_s}{2} \int_V \bar{\mathbf{u}}^T \mathbf{N}^T \mathbf{H}_m \mathbf{N} \bar{\mathbf{u}} dV \\ &= \frac{1}{2} \bar{\mathbf{u}}^T \left( \int_V \rho_s \mathbf{N}^T \mathbf{H}_m \mathbf{N} dV \right) \bar{\mathbf{u}} = \frac{1}{2} \bar{\mathbf{u}}^T \left( \int_0^{l_e} \rho_s \mathbf{N}^T \bar{\mathbf{H}}_m \mathbf{N} d\xi \right) \bar{\mathbf{u}} = \frac{1}{2} \bar{\mathbf{u}}^T \mathbf{M}_e \bar{\mathbf{u}}. \end{aligned} \quad (3.4)$$

where  $\mathbf{M}_e$  is the element mass matrix;  $\rho_s$  is the material density of the fuel elements; and

$$\mathbf{H}_m = \begin{bmatrix} 1 & 0 & 0 & 0 & z & -y \\ & 1 & 0 & -z & 0 & 0 \\ & & 1 & y & 0 & 0 \\ & & & y^2+z^2 & 0 & 0 \\ sym. & & & & z^2 & -yz \\ & & & & & y^2 \end{bmatrix}; \quad \bar{\mathbf{H}}_m = \begin{bmatrix} A & 0 & 0 & 0 & B_y & -B_z \\ & A & 0 & -B_y & 0 & 0 \\ & & A & B_z & 0 & 0 \\ & & & J & 0 & 0 \\ sym. & & & & I_y & -B \\ & & & & & I_z \end{bmatrix}.$$

The potential energy of the element can be expressed as

$$\begin{aligned} V_e &= \int_V \frac{1}{2} [E\varepsilon_x^2 + G(\gamma_{xy}^2 + \gamma_{xz}^2)] dV \\ &= \frac{1}{2} \int_V \mathbf{u}'^T \mathbf{H}_k \mathbf{u}' dV = \frac{1}{2} \int_V \bar{\mathbf{u}}^T \mathbf{N}'^T \mathbf{H}_k \mathbf{N}' \bar{\mathbf{u}} dV = \frac{1}{2} \int_V \mathbf{u}'^T \mathbf{H}_k \mathbf{u}' dV = \frac{1}{2} \int_V \bar{\mathbf{u}}^T \mathbf{N}'^T \mathbf{H}_k \mathbf{N}' \bar{\mathbf{u}} dV \\ &= \frac{1}{2} \bar{\mathbf{u}}^T \left( \int_V \mathbf{N}'^T \bar{\mathbf{H}}_k \mathbf{N}' d\xi \right) \bar{\mathbf{u}} = \frac{1}{2} \bar{\mathbf{u}}^T \mathbf{K}_e \bar{\mathbf{u}}. \end{aligned} \quad (3.5)$$

where  $\mathbf{K}_e$  is the element stiffness matrix;  $E$  is the Young's modulus,  $G$  is the shear modulus. A prime denotes the derivative of the quantity with respect to  $\xi$ .  $\mathbf{H}_k$  and  $\bar{\mathbf{H}}_k$  are

$$\mathbf{H}_k = \begin{bmatrix} 1 & 0 & 0 & 0 & z & -y \\ & 0 & 0 & 0 & 0 & 0 \\ & & 0 & 0 & 0 & 0 \\ & & & y^2+z^2 & 0 & 0 \\ sym. & & & & z^2 & -yz \\ & & & & & y^2 \end{bmatrix}; \quad \overline{\mathbf{H}}_k = \begin{bmatrix} EA & 0 & 0 & 0 & EB_y & -EB_z \\ & 0 & 0 & 0 & 0 & 0 \\ & & 0 & 0 & 0 & 0 \\ & & & GJ & 0 & 0 \\ sym. & & & & EI_y & -EB \\ & & & & & EI_z \end{bmatrix}.$$

The fuel element used in this research is circular, and therefore cross-section warping and does not happen.

### 3.2 Endplates

A typical CANDU fuel endplate consists of a few circular rings and a number of radial straight ribs. It is a component that holds together the fuel elements in different rings and forms an integral fuel bundle. The fuel elements are dynamically coupled through the endplates. An accurate endplate model is essential to the bundle vibration analysis.

Since fuel elements are modeled as beams, it will be convenient to model the endplates as beams or plates so that the degrees of freedom at the joint between the two structures match. Although more accurate finite element models can be developed using three dimensional elements, e.g., brick elements, the number of degrees of freedom is unnecessarily high; issues of inconsistency arise when the fuel elements and the endplates are joined together.

The endplate used in this modeling is shown in Figure 3.2, and the specifications are listed in Table 3.1. Note that the actual endplate design has not been finalized by its designer, AECL. The thickness of the endplate in the simulated bundle is based on a reference value given by AECL. The dimensions of the ribs and rings are same as the actual endplate. The material of the real endplate is zircaloy. The Young's modulus of zircaloy is 168 GPa with a Poisson's ratio of 0.25 at room temperature.

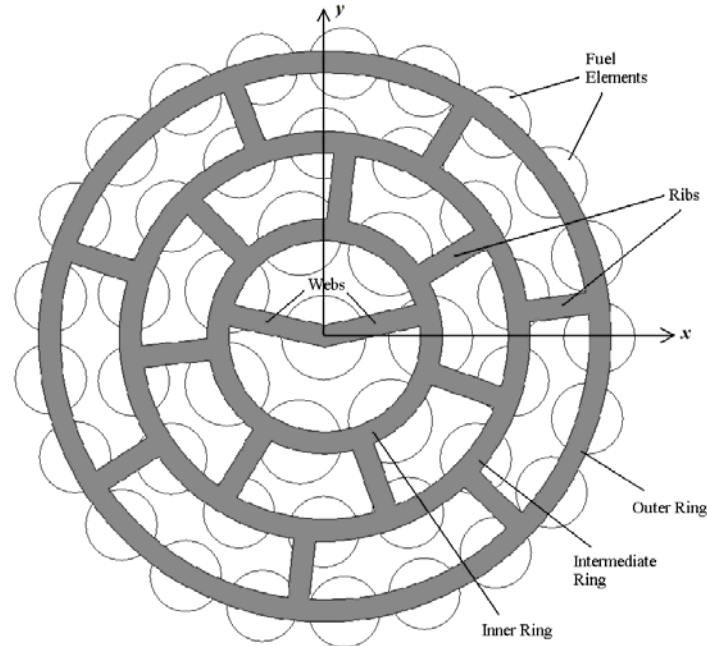


Figure 3.2 Front view of the endplate in the test fuel bundle.

Table 3.1 Endplate specification.

Parameters	Symbol	Values
Outer ring mean radius (mm)	$R_1$	42.5
Intermediate ring mean radius (mm)	$R_2$	30.0
Inner ring mean radius (mm)	$R_3$	16.5
Ring and rib width (mm)	$b$	3.4
Thickness (mm)	$t$	3.0
Young's Modulus (GPa)	$E$	210.0
Poisson's ratio	$\nu$	0.3
Shear Modulus (GPa)	$G$	80.8

The thickness of the endplate used in the simulated bundle is 3.0 mm; while the width of the ribs and rings are 3.4 mm. The endplate is considered very thick with a width-to-thickness ratio of 1.13.

A nine-node three-dimensional plate element has been developed by Yu and Wen (2007) based on Reddy's third-order thick plate theory (Reddy, 1984, 1996). A review of the thick plate theory and the finite element procedure for this thick plate element is given in Appendix. The endplate model built with the thick plate element is introduced below.

An endplate coordinate frame is defined as shown in Figure 3.2. The origin locates at the center of the endplate. The  $x$ -axis is defined as horizontal and the  $y$ -axis is vertical. The  $z$ -axis is perpendicular to the surface of the paper following the right-hand rule.

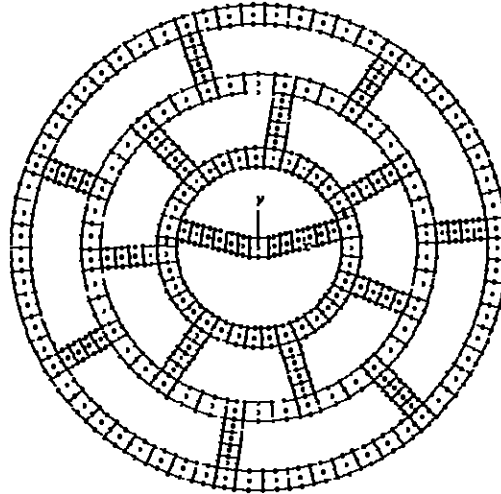


Figure 3.3 Mesh of the endplate model using the nine-node thick plate element.

The endplate is meshed using the nine-node thick plate element as shown in Figure 3.3. All the rings and ribs are meshed with one division in width. The element lengths in the angular direction in the outer ring, the intermediate ring and the inner ring are chosen as 1.2, 1.2 and 1.0 times of their width. The element length along the ribs is chosen to be 0.6 times of the rib width. The circular rings are meshed first with a numbering scheme shown in Figure 3.4a. This scheme guarantees a small bandwidth when the stiffness matrix is stored in a band format. Ribs are meshed after the rings with a numbering scheme shown in Figure 3.4b. The numbering scheme also guarantees a small bandwidth in the rib.

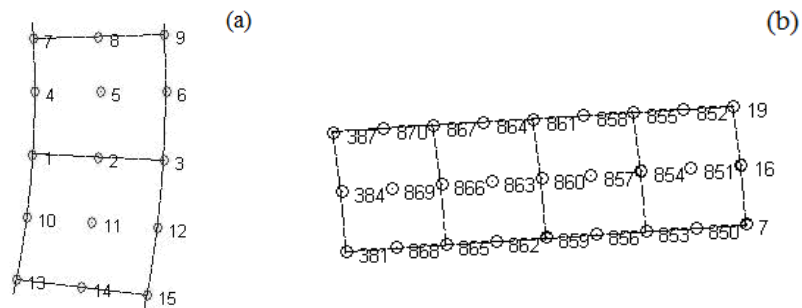


Figure 3.4 Node numbering schemes for the ring (a) and the rib (b).

Although the stiffness matrix bandwidths within the rings and the ribs are small, the entire endplate has a very large bandwidth after the rings and the ribs are assembled. This greatly undermines the efficiency when a band solver is used. To reduce computational

effort, substructuring method is employed. Each ring and rib is regarded as a subcomponent. The shared nodes between rings and ribs are considered as interface nodes. In addition, some nodes are used to establish the welds between the endplate and the fuel elements. These nodes are also kept as interface nodes in the substructuring procedure. Other nodes are considered interior nodes. The interior degrees of freedom in each subcomponent can be eliminated using static condensation (Bathe, 1996), as

$$\tilde{\mathbf{K}}_{ii} = \mathbf{K}_{ii} - \mathbf{K}_{ij} \mathbf{K}_{jj}^{-1} \mathbf{K}_{ji}, \quad (3.6)$$

where  $\mathbf{K}_{ii}$ ,  $\mathbf{K}_{ij}$ ,  $\mathbf{K}_{ji}$ , and  $\mathbf{K}_{jj}$  are the partitions of the stiffness matrix according to the interface and interior degrees of freedom; the subscript (i) denotes the interface degrees of freedom and the subscript (j) denotes the interior degrees of freedom.  $\tilde{\mathbf{K}}_{ii}$  is the condensed stiffness matrix for the interface degrees of freedom. The benefit is that the bandwidth of  $\mathbf{K}_{jj}$  in each subcomponent is small and  $\mathbf{K}_{jj}^{-1} \mathbf{K}_{ji}$  can be solved efficiently using a band solver. The subcomponents are kept small and substructured individually to avoid multiplication of large matrices in the calculation of  $\mathbf{K}_{ij}(\mathbf{K}_{jj}^{-1} \mathbf{K}_{ji})$ . After each subcomponent is substructured, the condensed stiffness matrices are assembled together to form the global stiffness matrix for the endplate.

A second level substructuring is applied to further eliminate the degrees of freedom on the shared nodes between the rings and the ribs. The entire endplate is then reduced to a superelement. The nodes of the super element are shown in Figure 3.5.

The boundary conditions are applied using the penalty method by modifying the corresponding diagonal entries in the stiffness matrix. For example, for a clamped boundary condition at 3 o'clock location in the outer ring, all degrees of freedom at node 4, 5 and 6 in Figure 3.4a should be fixed. This can be achieved by replacing the corresponding diagonal element in the stiffness matrix with a large number. The value of this large number should be a few orders higher than the largest diagonal element in the stiffness matrix. The largest diagonal element in the stiffness matrix is known to be at the order of  $10^6$ , so a value at the order of  $10^{10}$  can be used for the large number.

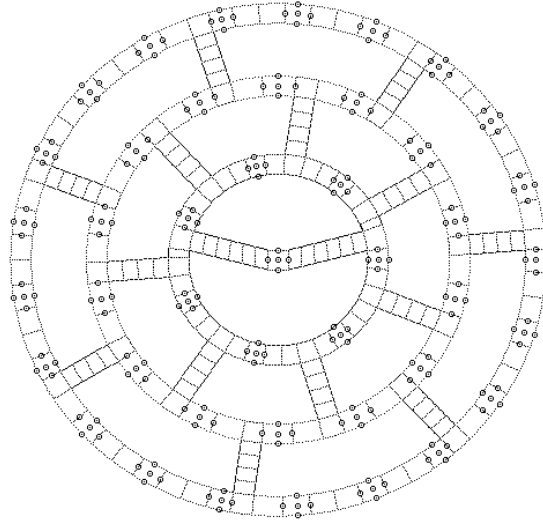


Figure 3.5 Super-element of the endplate.

To evaluate the accuracy of this endplate model, numerical tests are conducted. The plate model is compared to a model built with three-dimensional twenty-node brick elements (Hexa20) and solved using OpenFEM\*. The mesh information of the two models is listed in Table 3.2. The material properties are those of steel (Table 3.1). The finite element mesh, created using nine-node thick plate elements is shown in Figure 3.5. The model created using the Hexa20 elements is shown in Figure 3.6. In all numerical studies, the endplate is clamped at the outer ring at 9 o'clock position.

Table 3.2 Meshing parameters for two simulation endplates

Finite Element Model	Number of Elements	Number of DOFs
Twenty-node brick (Hexa20, OpenFEM)	2433	35130
Nine-node plate (Current thesis)	209	6,045

---

\* OpenFEM is an open-source finite element package co-owned by INRIA and SDTools. The software is licensed under the “GNU Lesser Public License”.

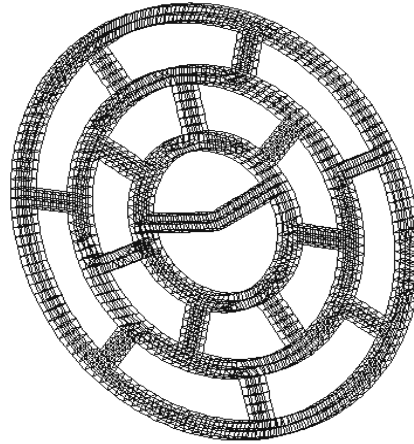


Figure 3.6 Endplate model discretized using Hexa20 elements.

Two load cases are designed for the endplate models. In the first load case, in-plane and out-of-plane bending are induced by a concentrated force. In the second case, bending and twisting are caused by a concentrated moment. It is noted that, in the brick element model, moment can not be directly applied to a node because the brick element nodal degrees of freedom do not include rotation angles. Therefore, a pair of offset forces (opposite in direction and equal in magnitude) are applied to its two immediate neighboring nodes to approximate a moment. Details of loads are given in Table 3.3.

Table 3.3 Load definition of the test cases.

Load case	Forces/Moments	Location (x, y, z) (mm)
1	$F_y = 100 \text{ N}$ $F_z = 30 \text{ N}$	(42.5,0,0)
2	$M_x = 0.15 \text{ Nm}$ $M_y = 0.17 \text{ Nm}$	(42.5,0,0)

The displacements ( $U_x$ ,  $U_y$  and  $U_z$ ) of the endplate in the mid-plane at the mean radius of the intermediate ring (Radius=30 mm), obtained using the two different approaches, are plotted against the polar angle in Figure 3.7 for load case 1 and in Figure 3.8 for load case 2. The horizontal axis of these figures is the angle along the intermediate ring, starting from 3 o'clock position (angle  $0^\circ$ ) and rotating counter-clockwise. Figure 3.7 shows the deformation of the intermediate ring due to load case 1. The maximum of  $U_y$  and  $U_z$  happens at the 3 o'clock position (angle  $0^\circ$ ), because this location is close to the load location. The minimum of  $U_y$  and  $U_z$  occurs at the 9 o'clock (angle  $180^\circ$ ) because this

location is near the constraint at the outer ring.  $U_x$  is negative in the first and second quadrants, and becomes positive in the third and fourth quadrant due to  $F_y$ . Load case 2 is used for out-of-plane twisting examination; the in-plane deformation  $U_x$  and  $U_y$  is negligibly small as shown in Figure 3.8. The out-of-plane deformation  $U_z$  is negative due to the applied  $y$ -moment. Its minimum occurs between  $270^\circ$  and  $360^\circ$  due to the applied  $x$ -moment. The results from the two models match with each other very well with a maximum error less than 1%.

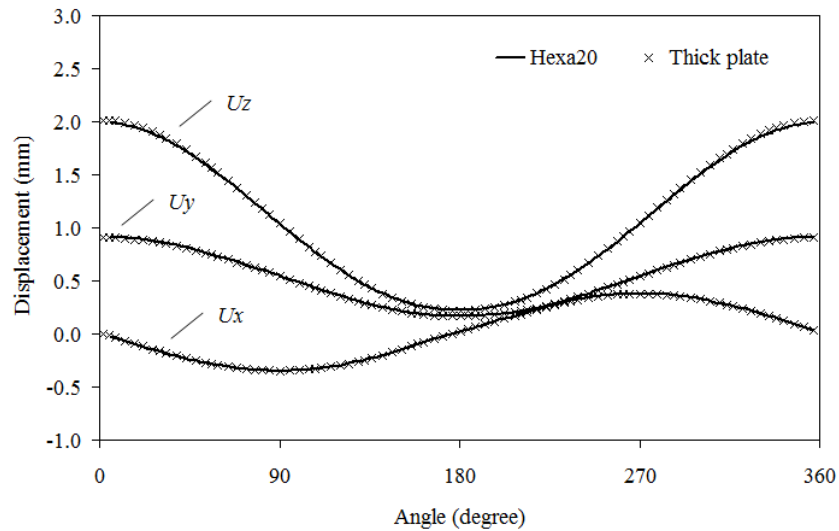


Figure 3.7 Displacements at the nodes in the mid-plane of the intermediate ring at Radius=30 mm for load case 1.

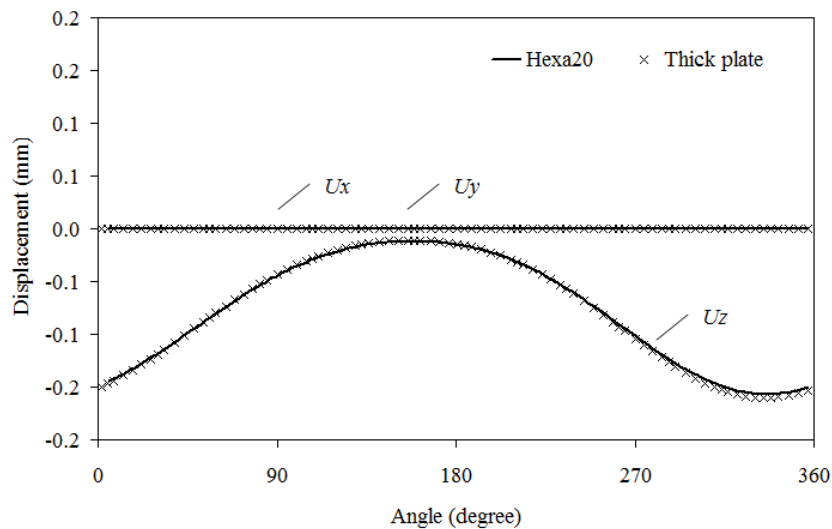


Figure 3.8 Displacements at the nodes in the mid-plane of the intermediate ring at Radius=30 mm for load case 2.

In a dynamic analysis, the mass of the endplates is ignored since the mass of two endplates only takes slightly more than 0.5% of the mass of the entire bundle.

### 3.3 Joint of Beam Element and Plate Element

There are six field variables at each node on a beam element: the three translations and three rotations; while the plate element only provides five field variables at each node, the three translations and two rotations. The rotation about the normal of the plate is not included. When the two elements are assembled together, special treatment must be applied to maintain consistency according to force balance.

The fuel elements are welded to the endplates. The weld joint greatly strengthens the rigidity of the endplate. Recall that the beam element is developed based on the Euler-Bernoulli beam theory so that the cross-section remains rigid after deformation. This assumption is reused in dealing with the joint. Figure 3.9 is a close-up of the joint nodes on the endplate rings shown in Figure 3.5. The nodes are numbered as 5, 6, 7, 8 and 9. These nodes enclose the area that covered by the beam cross-section.  $\alpha$  is the angular position of the joint, measured from 3 o'clock position.  $\Delta$  is the radius of the covered area.

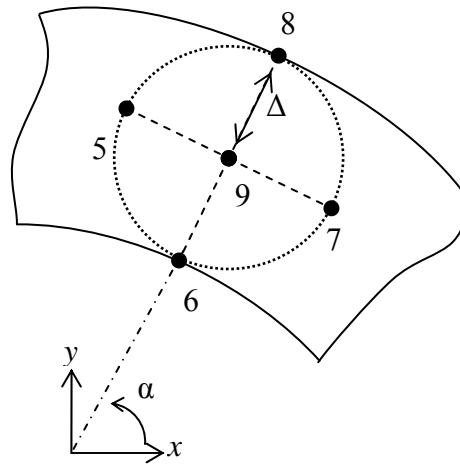


Figure 3.9 Joint nodes on an endplate ring.

Denote the translations and rotations of the node at the end of the beam as  $u, v, w$ , and  $\theta_x, \theta_y, \theta_z$ , respectively. Denote the translations and rotations of node  $i$  on the plate element in Figure 3.9 as  $u^i, v^i, w^i, \phi_x^i, \phi_y^i$ . Due to the rigid cross-section assumption, line 5-9-7 and 6-9-8 remain straight after deformation, and the displacements of node 5, 6, 7,

and 8 can be related to the translations and rotations of the beam node according to rigid body kinematics

$$\mathbf{u}^i = \mathbf{u}_b + \mathbf{A}_b \mathbf{x}^i \quad (i=5,6,7,8), \quad (3.7)$$

where  $\mathbf{u}^i = (u^i, v^i, w^i)^T$ ;  $\mathbf{u}_b = (u, v, w)^T$ ;  $\mathbf{x}^i = \mathbf{r}^i - \mathbf{r}^9 = (x_i, y_i, z_i)^T$ ;  $\mathbf{r}^i$  ( $i=5,6,7,8,9$ ) represent the global coordinates of node  $i$ .  $\mathbf{A}_b$  is a rotation matrix

$$\mathbf{A}_b = \begin{bmatrix} 0 & -\theta_z & \theta_y \\ \theta_z & 0 & -\theta_x \\ -\theta_y & \theta_x & 0 \end{bmatrix}$$

In addition to the above relationship, the rotation angles of all the nodes are equal to that of the beam node

$$\varphi_x^i = \theta_y; \quad \varphi_y^i = -\theta_x \quad (i=5,6,7,8,9). \quad (3.8)$$

Combining Eq. (3.7) and (3.8), a transform between the nodal degrees of freedom of the plate node  $i$  and the beam node can be established

$$\begin{Bmatrix} u^i \\ v^i \\ \varphi_x^i \\ \varphi_y^i \\ w^i \end{Bmatrix} = \begin{bmatrix} 1 & 0 & 0 & 0 & z_i & -y_i \\ 0 & 1 & 0 & -z_i & 0 & x_i \\ 0 & 0 & 0 & 0 & 1 & 0 \\ 0 & 0 & 0 & -1 & 0 & 0 \\ 0 & 0 & 1 & y_i & -x_i & 0 \end{bmatrix} \begin{Bmatrix} u \\ v \\ w \\ \theta_x \\ \theta_y \\ \theta_z \end{Bmatrix} \quad \text{or } \bar{\mathbf{u}}^i = \mathbf{C}^i \bar{\mathbf{u}}_b. \quad (3.9)$$

Applying Eq. (3.9) to nodes 5, 6, 7, 8 and 9, a transform between the 5 nodes and the beam node can be obtained as

$$\begin{Bmatrix} \bar{\mathbf{u}}^5 \\ \bar{\mathbf{u}}^6 \\ \bar{\mathbf{u}}^7 \\ \bar{\mathbf{u}}^8 \\ \bar{\mathbf{u}}^9 \end{Bmatrix} = \begin{bmatrix} \mathbf{C}^5 \\ \mathbf{C}^6 \\ \mathbf{C}^7 \\ \mathbf{C}^8 \\ \mathbf{C}^9 \end{bmatrix} \bar{\mathbf{u}}_b \quad \text{or } \bar{\mathbf{u}}^n = \mathbf{C}^n \bar{\mathbf{u}}_b \quad (n=1,2,\dots,N), \quad (3.10)$$

where  $n$  represents the index of the joint. This transform can be applied to the endplate stiffness matrix  $\mathbf{K}_{ep}$  during assembly to obtain a new matrix  $\tilde{\mathbf{K}}_{ep}$  which is consistent with the beam matrices, such that:

$$\tilde{\mathbf{K}}_{ep} = \begin{bmatrix} \mathbf{C}^1 & & \\ & \ddots & \\ & & \mathbf{C}^N \end{bmatrix}^T \mathbf{K}_{ep} \begin{bmatrix} \mathbf{C}^1 & & \\ & \ddots & \\ & & \mathbf{C}^N \end{bmatrix}. \quad (3.11)$$

### 3.4 Fuel Bundle

The finite element model of the bundle is shown in Figure 3.10. The fuel elements are discretized with 3 elements with different length. The beam element has 5th-order polynomials as shape functions for bending, so even three divisions is sufficient to simulate the first few bending modes accurately. Higher bending modes fall in a very high frequency range and are not considered in the current research. Geometric parameters and material properties are given in Table 3.4.

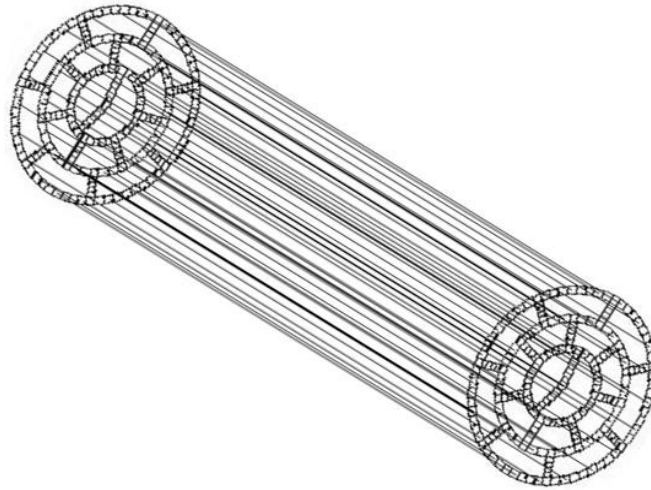


Figure 3.10 Finite element model of a simulated bundle.

Table 3.4 Geometric parameters and material properties of the bundle model

Parameters	Symbol	Values
Bundle length (mm)	L	500.0
Outer ring mean radius (mm)	R1	42.5
Intermediate ring mean radius (mm)	R2	30.0
Inner ring mean radius (mm)	R3	16.5
Ring and rib width (mm)	b	3.4
Endplate thickness (mm)	t	3.0
Young's Modulus (GPa)	E	200.0
Poisson's ratio	$\nu$	0.3
Shear Modulus (GPa)	G	76.9
Density ( $\text{kg/m}^3$ )	$\rho_s$	7800

The boundary conditions of the bundle are set to simple-supported connection at four locations, as shown in Figure 3.11, where bearing pads on the bottom two fuel elements make contact with the supporting tube. All the translational degrees of freedom are constrained while leaving rotational degrees of freedom free.

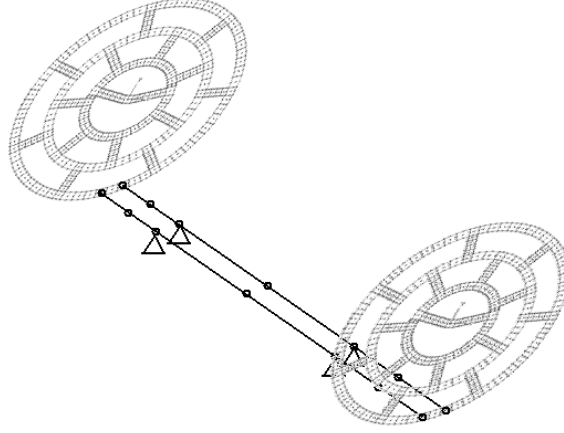


Figure 3.11 Nodes and constrained locations on the bottom fuel elements.

The element mass and stiffness matrices of the beam elements and the stiffness matrix of the endplates can be assembled to form the global mass and stiffness matrices. The linear equations of motion of the bundle for free vibration can be obtained using the Lagrange equations (Meirovitch, 2001) as

$$\frac{d}{dt} \left( \frac{\partial T}{\partial \dot{\mathbf{q}}} \right)^T - \left( \frac{\partial T}{\partial \mathbf{q}} \right)^T + \left( \frac{\partial V}{\partial \mathbf{q}} \right)^T = \mathbf{0}. \quad (3.12)$$

where  $T = \sum_{i=1}^{N_{elem}} T_e^i$ , representing the total kinetic energy;  $N_{elem}$  is the total number of beam

element.  $T_e^i = \left( \frac{1}{2} \dot{\mathbf{q}}_e^T \mathbf{T}^T \mathbf{M}_e \mathbf{T} \dot{\mathbf{q}}_e \right)_i$  is the kinetic energy of the  $i$ -th beam element.  $\mathbf{T}$  is the coordinate transform matrix that transfers the global (bundle) coordinates to the element coordinate, such that  $\bar{\mathbf{u}} = \mathbf{T} \mathbf{q}_e$ .  $\mathbf{q}_e$  represents the nodal displace vector in a beam finite

element in the global coordinates.  $V = \sum_{i=1}^{N_{elem}} V_e^i + \sum_{j=1}^{N_{ep}} V_{ep}^j$  is the total potential energy that

includes the sum of the element potential energy of beam elements  $V_e^i = \left( \frac{1}{2} \mathbf{q}_e^T \mathbf{T}^T \mathbf{K}_e \mathbf{T} \mathbf{q}_e \right)_i$

and the endplate potential energy  $V_{ep}^j = \left( \frac{1}{2} \mathbf{q}_{ep}^T \mathbf{K}_{ep} \mathbf{q}_{ep} \right)_j$ .  $\mathbf{q}_{ep}$  represents the endplate

superelement interface variables.  $N_{ep}$  is the total number of endplates.  $\mathbf{q}$  represent the

total nodal variable vector in the global coordinates  $\mathbf{q} = \left\{ (\mathbf{q}_e^1)^T, \dots, (\mathbf{q}_e^{N_{elem}})^T, (\mathbf{q}_{ep}^1)^T, \dots, (\mathbf{q}_{ep}^{N_{ep}})^T \right\}^T$ .

$$\mathbf{M}\ddot{\mathbf{q}} + \mathbf{K}\mathbf{q} = \mathbf{0}. \quad (3.13)$$

where  $\mathbf{M}$  and  $\mathbf{K}$  are the global mass and stiffness matrix assembled from the element mass stiffness matrix respectively. Natural frequencies and mode shapes can be obtained by solving the eigenvalue problem  $\omega_i^2 \mathbf{M}\boldsymbol{\phi}_i = \mathbf{K}\boldsymbol{\phi}_i$ , where  $\omega_i$  is the  $i$ -th natural frequency, and  $\boldsymbol{\phi}_i$  is the corresponding modal vector. The eigenvalue problem was solved using subroutines in LAPACK<sup>†</sup>. The first 20 natural frequencies are listed in Table 3.5. Mode shapes for mode 1, 2, 3 and 20 are shown in Figure 3.12. Note that the mode shapes are displayed with straight lines joining adjacent nodes.

Table 3.5 Natural frequencies of the bundle.

Mode	Frequency (Hz)						
1	7.7	6	94.8	11	101.9	16	104.4
2	50.8	7	95.4	12	102.0	17	104.6
3	93.0	8	96.3	13	102.7	18	105.4
4	93.8	9	99.6	14	103.5	19	106.4
5	94.3	10	101.4	15	104.3	20	107.1

It is necessary to validate the accuracy of the meshing scheme and the numerical solution routines used in this thesis against independent finite element code. The modal solution from this model is compared to that of a bundle model developed in ANSYS<sup>®</sup> ED Release 8.0 using straight beam elements. The comparison of the natural frequencies is shown in Table 3.6.

Table 3.6 Validation on the current finite element model against ANSYS ED 8.0

Mode	Natural frequencies (Hz)			Mode	Natural frequencies (Hz)		
	Current	ANSYS	Error		Current	ANSYS	Error
1	7.7	7.5	2.7%	4	93.8	93.2	0.6%
2	50.8	50.0	1.6%	5	94.3	93.6	0.7%
3	93.0	87.7	6.0%	6	94.8	94.0	0.9%

<sup>†</sup> LAPACK, a Fortran library in the public domain, containing fully tested subroutines for solving linear systems.

<sup>®</sup> ANSYS, a registered trade mark of ANSYS, Inc.

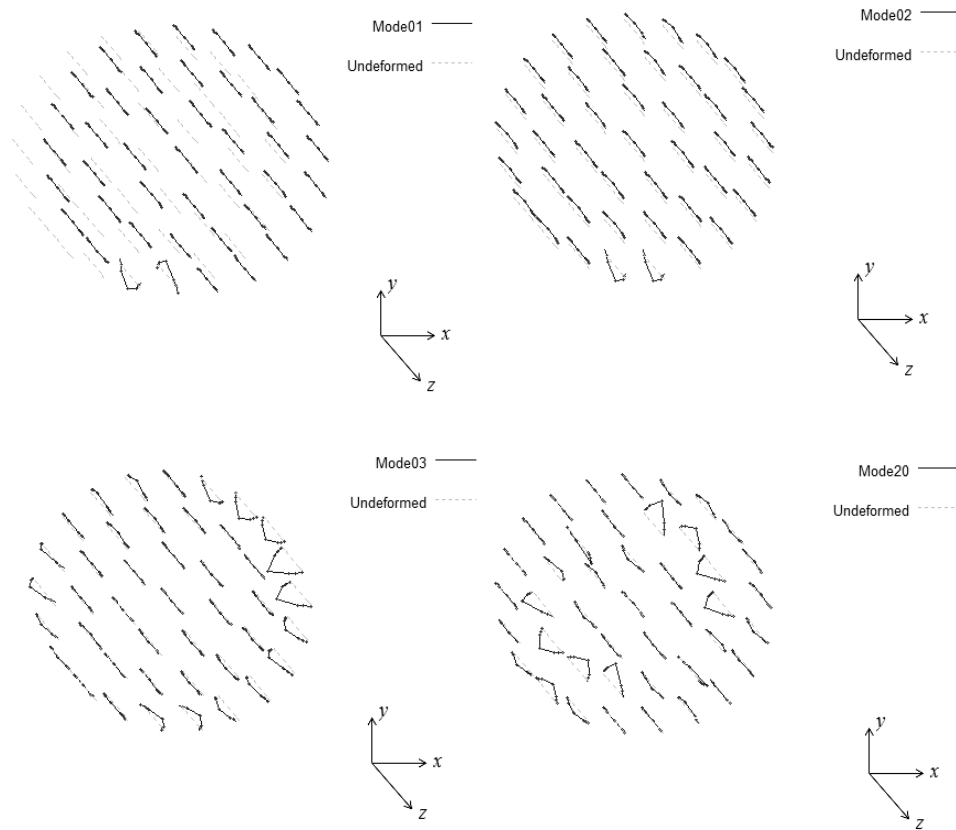


Figure 3.12 Mode shapes for four modes.

### 3.5 Summary of the Chapter

In this chapter, a finite element model of the fuel bundle was developed. The fuel elements were modeled using three-node beam elements; while the endplates were modeled using special nine-node thick plate elements. Free vibration simulation was conducted using this model and the result was compared to that from ANSYS.

## CHAPTER 4 VIBRATION OF THE INLET BUNDLE SUBJECTED TO TURBULENT FLOW

This chapter presents the modeling and solution procedures for the vibration of the inlet bundle induced by the turbulent coolant flow. The finite element models developed in Chapter 3 is adopted for structural response. Weak coupling between the structural motion and the fluid flow is applied to the structural model. The response of the inlet bundle under the fluid excitation from Chapter 2 is sought with modal analysis in the time domain and the frequency domain respectively. Experiments are conducted and compared to the simulation results.

Section 4.1 presents the experimental work related to the inlet bundle vibration under multiple flow conditions. Section 4.2 explains how the structure interacts with the fluid and how this interaction is simplified based on the flow condition for use in the inlet bundle vibration model. Section 4.3 established the system governing equations and the solution methods. Section 4.4 describes the solution methods used to obtain the bundle response. Section 4.5 presents the numerical results and the comparison with experiments.

### 4.1 Experiments for the Fuel Bundle Vibration

#### 4.1.1 *Experimental Setup and Procedures*

Experiments have been done to study the flow-induced vibration of the inlet bundle. The experimental test rig, as illustrated in Figure 4.1, consists of a 500 gallon tank, a 15 m PVC pipe loop, and a 10 horsepower centrifugal pump. The inner diameter  $D_p$  of the pipe is 101.6 mm (4 inch). The test chamber, located before the vertical pipe that connected to the tank, is made of clear PVC pipe. The distance between the inlet of the test chamber and the elbow in the nearest upstream is  $30D_p$ . This allows the pipe flow to fully develop before entering the test section. Two bundles are placed in the test chamber. A shield plug is mounted to the pipe using flanges at the outlet of the test chamber. The shield plug stops the bundle from sliding along the pipe when flow is applied. The second bundle is clamped to the shield plug. Stopping screws are used from the side at multiple

locations on the second bundle to prevent it from rocking. The purpose of using the second bundle is to eliminate wake at the downstream of the inlet bundle. The inlet bundle is separated using a tiny roller from the second bundle. The roller prevents the inlet bundle from moving along the pipe but allows the motion in the lateral directions. The size of the roller is very small so the gap between the two bundles is not too large to significantly affect the flow. The pump provides a maximum mass flow rate of 25.7 kg/s when two bundles are present in the test chamber. Tap water at room temperature is used as the fluid. Pressurization of 1.4 atmosphere pressure is (142 kPa) applied to eliminate air bubbles and cavities. A magnetic flow meter is installed to record the mass flow rate.

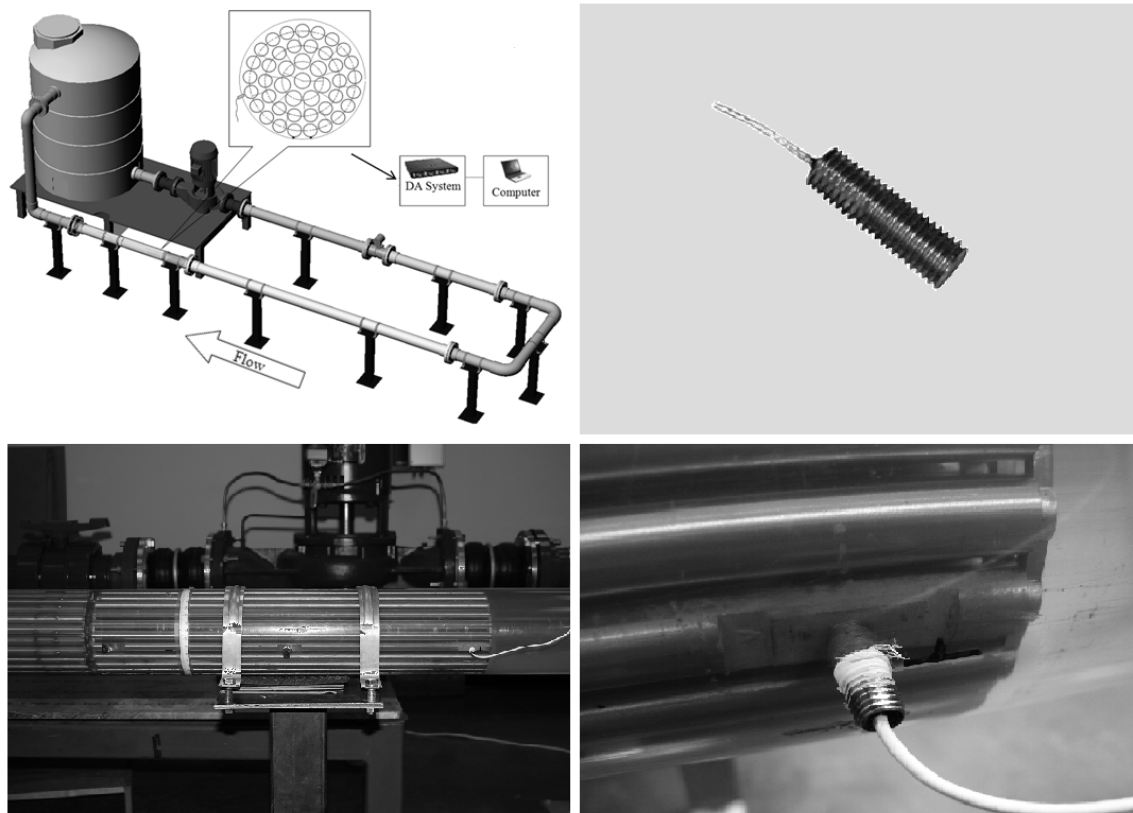


Figure 4.1 Experimental setup for the flow-induced vibration of the inlet bundle.

A non-contact differential variable reluctance transducer (MicroStrain NC-DVRT-1.5) is installed at the location shown in Figure 4.1 and Figure 4.2. The sensor detects distance between a target object and the face of the transducer head. The reluctance of the coils within the sensor is changed when the face of the transducer is in close proximity to a ferrous or highly conductive material. The transducer outputs a voltage signal that is a

nonlinear function of the distance. The typical repeatability of this transducer is  $\pm 2 \mu\text{m}$  and the frequency range is 0 to 800 Hz. The voltage signals output from the sensor are collected by the HS4 multi-channel data acquisition system at a sampling rate of 1 kHz. This sampling rate is sufficiently high to prevent aliasing problem because the DVRT displacement transducer is insensitive to high frequency vibrations. The transducer has a cut-off frequency of 800 Hz. The transducer only works with ferrous material and does not react to fuel elements made of stainless steel. A small piece of steel plate is mounted on the monitored fuel element (R7 defined in Figure 2.2) at the sensor location as shown in Figure 4.1. The size of the steel plate is recommended by the manufacturer of the transducer and does not influence accuracy. The transducer was calibrated by the manufacturer with water as working medium. It needs to be emphasized that the readout of the transducer is the normal distance between the sensor and the target.

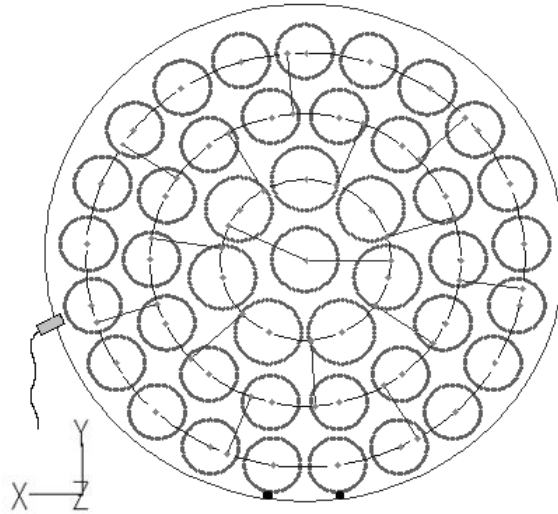


Figure 4.2 Illustration of the sensor location.

#### 4.1.2 Free Vibration of the Inlet Bundle in Still Fluid

A free vibration test has been conducted on the inlet bundle in the test chamber without filling with water. An impact is applied to the pipe at the bundle location. The response is recorded and shown in Figure 4.3. The fundamental frequency is 6.6 Hz. The motion is a rocking motion. The viscous damping factor  $\zeta$  can be calculated using the formula

$$\zeta = \frac{\delta_j}{\sqrt{4\pi^2 + \delta_j^2}}; \quad \delta_j = \frac{1}{j} \ln \frac{d_i}{d_{i+j}}, \quad (4.1)$$

where  $i$  and  $j$  are integers;  $d_i$  is the value of the  $i$ -th peak;  $d_{i+j}$  is the value of the  $(i+j)$ -th peak. The viscous damping factor  $\zeta$  is calculated to be 0.012 from the measurement.

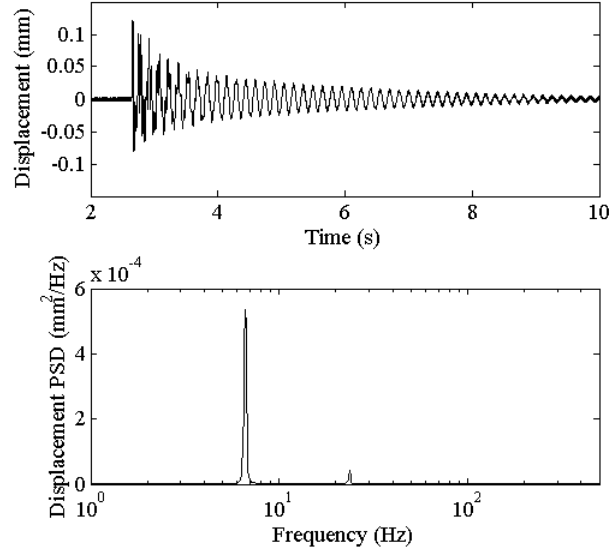


Figure 4.3 Time history and PSD of the relative displacement between the sensor and the monitored fuel element in the free vibration without water.

The free vibration response of the inlet bundle with the test chamber fully filled with water but no flow is shown in Figure 4.4. The dominant frequency reduces to 5.4 Hz due to added mass and viscous damping. The damping factor  $\zeta$  for is calculated to be 0.031 based on the measurement. This indicates that for the fundamental rocking motion, the fluid damping is very small.

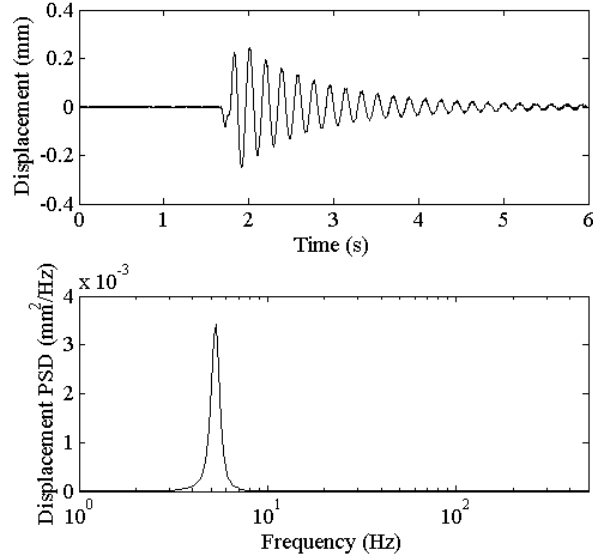


Figure 4.4 Time history and PSD of the relative displacement between the sensor and the monitored fuel element in the free vibration within water.

#### 4.1.3 *Vibration of the Inlet Bundle Induced by Flow*

The flow-induced vibration of the bundle was recorded for 40 mass flow rates from 8.3 to 25.6 kg/s. The corresponding range of the average flow velocity in the bundle is 2.3 to 7.2 m/s. The record length for each measurement is 60 seconds.

The measured relative displacements between the transducer head and the target fuel element, together with their PSD, for six flow velocities are shown in Figure 4.5. Note that the mean value of the displacement has been deducted. The PSD is evaluated using Welch's method (Oppenheim and Schaffer, 1975) with an overlapping of 50% and a Gaussian window applied to each data segment.

The maximum displacement is less than 0.1 mm for the highest flow velocity case, and reduces to 0.01 mm for the lowest flow velocity case. In all six cases, the predominant frequency appears around 5.5 Hz, without obvious shifting with the change of the flow velocity. This indicates that there is no instability issue and the bundle vibration is largely a forced vibration problem. The sharp spikes appearing in the higher frequency range are induced by the electric noise, because they are precisely 60, 120, 180 and 360 Hz and the alternating current in the power supply has a frequency of 60 Hz.

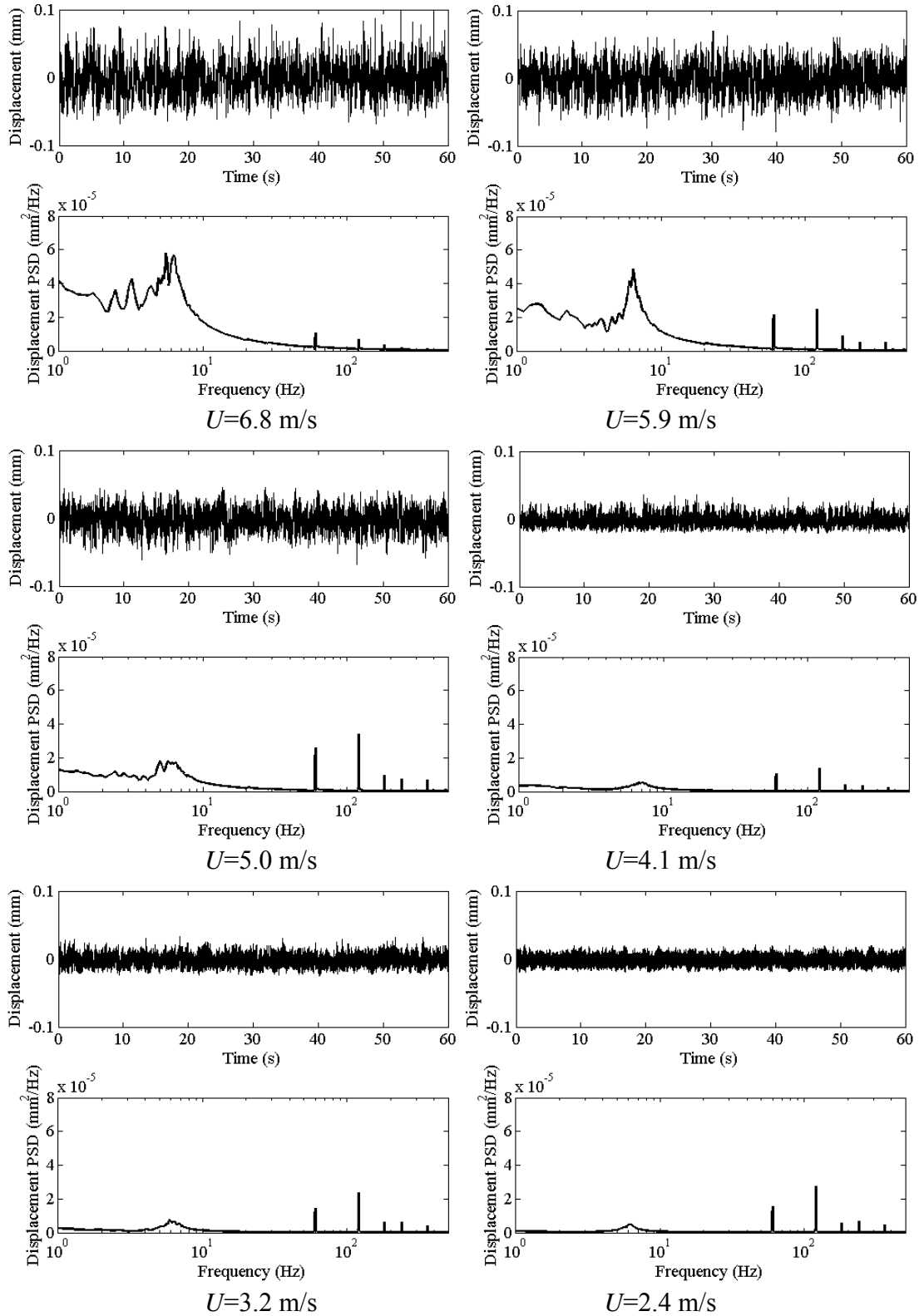


Figure 4.5 Time history and PSD of the relative displacement between the sensor and the monitored fuel element obtained in the flow-induced vibration experiments.

## 4.2 Solid-Fluid Interaction

### 4.2.1 Solid-Fluid Coupling

A submerged body is subjected to force and moment induced by the pressure distribution and viscous friction on the solid-fluid boundary. If the body undergoes a motion, the fluid field is disturbed by this motion and extra fluid force and moment will be exerted. The solid-fluid interaction must be considered in a flow-induced vibration analysis; however, solution of fully coupled structure and fluid field is difficult and sometimes impossible for complicated engineering systems. Simplification is necessary and beneficial.

Experiments show that the bundle vibration amplitude is in the order of 0.1 mm level. This amplitude is very small compared to the diameters of the fuel elements (11 and 13 mm) and the cross-sectional dimension of the subchannels (5~15 mm). The change on the geometry of the flow channels caused by the motion of the bundle is therefore negligible. The vibration velocity amplitude is in the order of 1 mm/s, which is far smaller than the average flow velocity of 6.8 m/s in the bundle, and even much smaller than the flow velocity oscillation caused by turbulence. Therefore, the influence of the structural motion to the solution of the fluid field is negligible. This allows the fluid field to be solved for fluid excitation without considering the bundle motion as what has been done in Chapter 2. However, the dynamic properties of the bundle are significantly influenced by the presence of the flow due to added mass, fluid damping and added stiffness. These terms come from the reaction force of a fluid field to the structure motion, and can be obtained by analytically solving a simple fluid field, such as a cross flow or a parallel flow. The added mass, fluid damping and added stiffness can then be applied back to the structure together with the fluid excitation to calculate the flow-induced vibration response. The coupling between the structure and the fluid is reduced by this approach, and therefore it is referred as weak solid-fluid coupling.

The bundle flow is largely a parallel flow since the flow channel is very long compared to the hydraulic diameter of the subchannels. The ratio between the length and the hydraulic diameter  $D_h$  (defined in Section 2.2.1) reaches 62.5. The solid-fluid interaction force on the fuel elements can be obtained by following the approach developed by Lighthill

(1960) and Paidoussis (1966, 2004). As shown in Figure 4.6, a slender cylinder in a parallel flow with a mean flow velocity of  $U$  is subjected to a distributed drag force  $F_L$  and lift forces  $F_A^y, F_N^y$  in the  $x$ - $y$  plane.

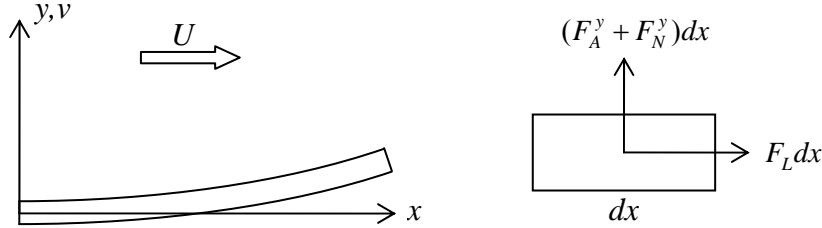


Figure 4.6 Cylinder in parallel flow.

$F_A$  is the inviscid force per unit length. This force arises from the solution of the potential flow surrounding the cylinder that is disturbed by the lateral displacement  $v$  of the cylinder.  $F_L$  and  $F_N$  are the viscous friction forces per unit length in the longitudinal and the normal direction, respectively. According to Paidoussis (2004), these forces can be written in the following form

$$F_A^y = \chi \rho A \frac{\partial^2 v}{\partial t^2} + U(1 + \chi \rho A) \frac{\partial^2 v}{\partial x \partial t} + U^2 \frac{\partial^2 v}{\partial x^2}; \quad (4.2)$$

$$F_N^y = \frac{1}{2} \rho D U C_N \left( \frac{\partial v}{\partial t} + U \frac{\partial v}{\partial x} \right) + \frac{1}{2} \rho D C_D \frac{\partial v}{\partial t}; \quad (4.3)$$

$$F_L = \frac{1}{2} \rho D U^2 C_T, \quad (4.4)$$

where  $\chi$  is the added mass coefficient due to confinement. Its value can be calculated as  $\chi = (D_{ch}^2 + D_r^2) / (D_{ch}^2 - D_r^2)$  (Chen and Wambsganss, 1972; Paidoussis, 1973);  $D_{ch}$  is the average subchannel diameter, estimated as 16 mm in the bundle;  $D_r$  is the average cylinder diameter, estimated to be 12 mm;  $\rho$  is the fluid density;  $A$  is the cross-sectional area of the cylinder;  $D$  is the diameter of the cylinder;  $C_N$  and  $C_T$  are the viscous drag coefficients in the lateral and longitudinal direction respectively;  $C_D$  is the viscous drag coefficient in quiescent flow. The term containing  $C_D$  represents the fluid damping on a

vibrating cylinder submerged in still fluid (Blevins, 1993). Similarly, the lateral forces in the  $x$ - $z$  plane have the form

$$F_A^z = \chi\rho A \frac{\partial^2 w}{\partial t^2} + U(1 + \chi\rho A) \frac{\partial^2 w}{\partial x \partial t} + U^2 \frac{\partial^2 w}{\partial x^2}; \quad (4.5)$$

$$F_N^z = \frac{1}{2}\rho D U C_N \left( \frac{\partial w}{\partial t} + U \frac{\partial w}{\partial x} \right) + \frac{1}{2}\rho D C_D \frac{\partial w}{\partial t}; \quad (4.6)$$

$C_T$  and  $C_N$  are empirical coefficients whose values need to be measured. Hoerner (1965) compiled the value of  $C_T$  from the measurement done by other researchers for cylinders in a parallel flow. Hoerner's data recommended  $C_T = 0.02$ . Ni and Hansen (1978) measured  $C_T$  for turbulent flows with Reynolds numbers from  $7.2 \times 10^4$  to  $1.1 \times 10^5$ . The result showed that  $C_T$  could be approximated as 0.012. Paidoussis (2004) recommended a reasonable range for  $C_T$  as  $0.008 \leq C_T \leq 0.02$ . For the value of  $C_N$ , Oreloff and Ives (1969) found that  $C_N = 2C_T$  for smooth cylinder, and therefore a reasonable range for  $C_N$  is  $0.016 \leq C_N \leq 0.04$ . In the current research,  $C_T$  and  $C_N$  are chosen as 0.01 and 0.02, respectively.  $C_D$  is related to the vibration amplitude and frequency of the cylinder. For a long cylinder oscillating in quiescent viscous fluid,  $C_D = \pi^2 D f c_d$ , where  $f$  is the oscillation frequency in Hz and  $c_d = 2\sqrt{2} / \sqrt{\pi f D^2 / (2\nu)}$  (Batchelor, 1967). For current application, it can be calculated  $C_D \approx 0.05$  for the fundamental mode ( $f \approx 6$  Hz) and  $C_D \approx 0.15$  for the second modes ( $f \approx 50$  Hz). For higher modes,  $C_D$  increase with  $\sqrt{f}$ ; however, the damping factor  $\zeta$  varies with  $C_D / f$ . Therefore, the damping for higher modes is small and plays minor role. In the solution of the bundle vibration, the value of  $C_D$  is taken as a constant of 0.1.

#### 4.2.2 Added Mass, Added Stiffness and Fluid Damping

Eqs (4.2), (4.3), (4.5) and (4.6) give the added mass, added stiffness and fluid damping for the fuel elements in the bundle flow. The added mass terms are

$$\chi\rho A \frac{\partial^2 v}{\partial t^2} \text{ in } y\text{-direction}; \quad (4.7)$$

$$\chi\rho A \frac{\partial^2 w}{\partial t^2} \text{ in } z\text{-direction.}$$

The added stiffness terms are

$$\begin{aligned} U^2 \frac{\partial^2 v}{\partial x^2} \text{ and } \frac{1}{2} \rho D U C_N U \frac{\partial v}{\partial x} \text{ in } y\text{-direction;} \\ U^2 \frac{\partial^2 w}{\partial x^2} \text{ and } \frac{1}{2} \rho D U C_N U \frac{\partial w}{\partial x} \text{ in } z\text{-direction.} \end{aligned} \quad (4.8)$$

The fluid damping terms are

$$\begin{aligned} \frac{1}{2} \rho D (U C_N + C_D) \frac{\partial v}{\partial t} \text{ and } U (1 + \chi \rho A) \frac{\partial^2 v}{\partial x \partial t} \text{ in } y\text{-direction;} \\ \frac{1}{2} \rho D (U C_N + C_D) \frac{\partial w}{\partial t} \text{ and } U (1 + \chi \rho A) \frac{\partial^2 w}{\partial x \partial t} \text{ in } z\text{-direction.} \end{aligned} \quad (4.9)$$

Note that the coordinates used here are the local frame attached on fuel elements. The  $x$ -axis of this frame coincides with the fuel element neutral axis.

The above added mass, added stiffness and damping terms need to be implemented into the formula of the fuel element finite element. Added mass and added stiffness matrices can be calculated and sum up with the structural mass and stiffness matrix. The damping matrix can also be calculated.

The added mass matrix can be obtained in the similar way as the structural mass matrix

$$\mathbf{M}_e^a = \int_0^{l_e} \mathbf{N}^T \bar{\mathbf{H}}_m^a \mathbf{N} d\xi \text{ and } \bar{\mathbf{H}}_m^a = \begin{bmatrix} 0 & & & & \\ & \chi\rho A & & & \\ & & \chi\rho A & & \\ & & & 0 & \\ & & & & 0 \\ & & & & & 0 \end{bmatrix}. \quad (4.10)$$

The added stiffness matrix contains two parts as

$$\mathbf{K}_e^a = \mathbf{K}_e^{ai} + \mathbf{K}_e^{av}, \quad (4.11)$$

where  $\mathbf{K}_e^{ai}$  arises from the inviscid force  $F_A$  and  $\mathbf{K}_e^{av}$  comes from the viscous force  $F_N$ .

$$\mathbf{K}_e^{ai} = \int_x \mathbf{N}^T \bar{\mathbf{H}}_k^{ai} \mathbf{N}'' d\xi \text{ and } \bar{\mathbf{H}}_k^{ai} = \begin{bmatrix} 0 & & & & & \\ & U^2 & & & & \\ & & U^2 & & & \\ & & & 0 & & \\ & & & & 0 & \\ & & & & & 0 \end{bmatrix}; \quad (4.12)$$

$$\mathbf{K}_e^{av} = \int_x \mathbf{N}^T \bar{\mathbf{H}}_k^{av} \mathbf{N}' d\xi \text{ and } \bar{\mathbf{H}}_k^{av} = \begin{bmatrix} 0 & & & & & \\ & \rho D U^2 C_N & & & & \\ & & \rho D U^2 C_N & & & \\ & & & 0 & & \\ & & & & 0 & \\ & & & & & 0 \end{bmatrix}. \quad (4.13)$$

In the above equations, a prime denotes the differentiation with respect to  $x$ .

The damping matrix also contains two parts that comes from the inviscid force  $F_A$  and the viscous force  $F_N$ .

$$\mathbf{C}_e = \mathbf{C}_e^i + \mathbf{C}_e^v; \quad (4.14)$$

$$\mathbf{C}_e^i = \int_x \mathbf{N}^T \bar{\mathbf{H}}_c^i \mathbf{N}' d\xi \text{ and } \bar{\mathbf{H}}_c^i = \begin{bmatrix} 0 & & & & & \\ & U(1+\chi\rho A) & & & & \\ & & U(1+\chi\rho A) & & & \\ & & & 0 & & \\ & & & & 0 & \\ & & & & & 0 \end{bmatrix}; \quad (4.15)$$

$$\mathbf{C}_e^v = \int_x \mathbf{N}^T \bar{\mathbf{H}}_c^v \mathbf{N} d\xi \text{ and } \bar{\mathbf{H}}_c^v = \begin{bmatrix} c_1 & & & & & \\ & c_2 & & & & \\ & & c_3 & & & \\ & & & c_4 & & \\ & & & & c_5 & \\ & & & & & c_6 \end{bmatrix}, \quad (4.16)$$

where  $c_i$  ( $i=1, \dots, 6$ ) are coefficients of viscous damping for the six degrees of freedom of a beam node,  $u, v, w, \theta_x, \theta_y, \theta_z$ ; it is known that  $c_2 = c_3 = \rho D(UC_N + C_D)/2$  and all other  $c_i$  are equal to zero.

It can be seen that matrices  $\mathbf{K}_e^a$  and  $\mathbf{C}_e^i$  are not symmetric. They can be converted to symmetric forms so that symmetric band matrix storage format and corresponding solvers can be used for better efficiency. This is done by considering the virtual work contributed by a force  $F_y = \alpha \frac{\partial v}{\partial x}$

$$\delta W = \int_0^{l_e} \delta v F_y d\xi = \int_0^{l_e} \delta v \alpha \frac{\partial v}{\partial x} d\xi = \int_0^{l_e} \delta \bar{v}_s^T \mathbf{N}_y^T \alpha \mathbf{N}'_y \bar{v}_s d\xi = \delta \left( \frac{1}{2} \int_0^{l_e} \bar{v}_s^T \mathbf{N}_y^T \alpha \mathbf{N}'_y \bar{v}_s d\xi \right). \quad (4.17)$$

where  $\bar{v}_s$  is the nodal displacement in the  $y$ -direction;  $\mathbf{N}_y$  is the shape function for displacement  $v$ . Since  $\delta w$  is a scalar, the transpose of a scalar is itself.

$$\delta W = \delta \left( \frac{1}{2} \int_0^{l_e} \bar{v}_s^T \mathbf{N}_y^T \alpha \mathbf{N}'_y \bar{v}_s d\xi \right)^T = \delta \left( \frac{1}{2} \int_0^{l_e} \bar{v}_s^T \mathbf{N}'_y{}^T \alpha \mathbf{N}_y \bar{v}_s d\xi \right) = \int_0^{l_e} \delta \bar{v}_s^T \mathbf{N}'_y{}^T \alpha \mathbf{N}_y \bar{v}_s d\xi. \quad (4.18)$$

Therefore,  $\delta w$  can be written in an alternate form

$$\delta W = \frac{1}{2} \left( \int_0^{l_e} \delta \bar{v}_s^T \mathbf{N}_y^T \alpha \mathbf{N}'_y \bar{v}_s d\xi + \int_0^{l_e} \delta \bar{v}_s^T \mathbf{N}'_y{}^T \alpha \mathbf{N}_y \bar{v}_s d\xi \right). \quad (4.19)$$

Utilizing the above approach,  $\mathbf{K}_e^a$  and  $\mathbf{C}_e^i$  can be written as

$$\tilde{\mathbf{K}}_e^a = \frac{1}{2} \mathbf{K}_e^a + \frac{1}{2} (\mathbf{K}_e^a)^T \quad \text{and} \quad \tilde{\mathbf{C}}_e^i = \frac{1}{2} \mathbf{C}_e^i + \frac{1}{2} (\mathbf{C}_e^i)^T. \quad (4.20)$$

$\tilde{\mathbf{K}}_e^a$  and  $\tilde{\mathbf{C}}_e^i$  are symmetric and can be handled as other matrices.

Numerical solutions show that  $\tilde{\mathbf{K}}_e^a$  and  $\tilde{\mathbf{C}}_e^i$  can contain negative values on the diagonal entries. This indicates that the added stiffness may weaken the structure and the added damping may introduce instability. However, the values of the elements in  $\tilde{\mathbf{K}}_e^a$  are many orders smaller than those in the structural stiffness matrix and therefore have no actual influence on the system stiffness. The value of  $\tilde{\mathbf{C}}_e^i$  depends on the mean velocity of the parallel flow  $U$ . Following Paidoussis (2004), a dimensionless flow velocity can be defined as  $u_c = UL\sqrt{\rho A/EI}$ , where  $L$ ,  $A$ ,  $E$ , and  $I$  are the length, the cross-sectional area, the Young's modulus and the cross-sectional area moment of inertia of a fuel element;  $\rho$  is the fluid density. The highest dimensionless velocity is  $u_c = 0.31$  for the fuel elements at center and in the inner ring; and  $u_c = 0.26$  for the fuel elements in the intermediate ring and outer ring. These dimensionless velocities are far below the critical velocity of  $u_c = 3.5$  required for fluid-elastic instability to occur (Paidoussis 2004). Therefore, individual fuel elements are not expected to experience fluid-elastic instability issues.

### 4.2.3 *P-Delta Effect*

For slender beam structure subjected to compressive longitudinal load, the longitudinal load introduces an additional moment when the beam undergoes a lateral deflection. This additional moment leads to a larger bending displacement and hence undermines the beam stiffness. This effect is called the *p*-delta effect. Fuel elements in a bundle string are subjected to large longitudinal load due to the frictional drag  $F_L = \frac{1}{2}\rho DU^2 C_T$  and the form drag applied on the inlet endplate on the upstream surface. It is necessary to consider the *p*-delta effect.

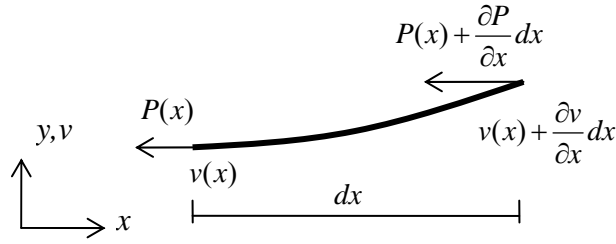


Figure 4.7 An element of a beam with distributed longitudinal force.

When a axial force per unit length  $P(x)$  is applied to a beam as shown in Figure 4.8, the additional moments produced by this axial force on an element are

$$\begin{aligned} dM_z &= -(P + \frac{\partial P}{\partial x} dx) \frac{\partial v}{\partial x} dx \doteq -P(x) \frac{\partial v}{\partial x} dx = -P(x) \theta_z dx; \\ dM_y &= -(P + \frac{\partial P}{\partial x} dx) \frac{\partial w}{\partial x} dx \doteq -P(x) \frac{\partial w}{\partial x} dx = P(x) \theta_y dx. \end{aligned} \quad (4.21)$$

The virtual work introduced by these moments is

$$\begin{aligned} \delta W &= \int_{x_1}^{x_2} -\delta \theta_z P(x) \theta_z dx + \int_{x_1}^{x_2} \delta \theta_y P(x) \theta_y dx = \int_0^l \delta \bar{\mathbf{u}}^T \mathbf{N}^T \bar{\mathbf{H}}_k^P \mathbf{N} \bar{\mathbf{u}} d\xi \\ \bar{\mathbf{H}}_k^P &= \begin{bmatrix} 0 & & & & \\ & 0 & & & \\ & & 0 & & \\ & & & 0 & \\ & & & & P(x) \\ & & & & & P(x) \end{bmatrix}. \end{aligned} \quad (4.22)$$

### 4.2.4 Discretization of the Fluid Excitations

The fluid forces obtained from the flow simulation have to be discretized based on the finite element mesh. The fluid forces are regarded as concentrated forces acting on the center of each segment. The nodal force vector  $\bar{\mathbf{F}}^e$  in a finite element can be calculated as

$$\bar{\mathbf{F}}^e(t) = \sum_{n=1}^{Ne} \mathbf{N}^T \mathbf{F}_n^e(t), \quad (4.23)$$

where  $\mathbf{F}_n^e$  is the concentrated force vector within the length of the finite element;  $Ne$  is the number of concentrated forces within the length of the finite element. After the nodal forces in all elements are computed, the global force vector  $\mathbf{F}$  can be assembled. Figure 4.8 shows the discretized forces on a few selected fuel elements.

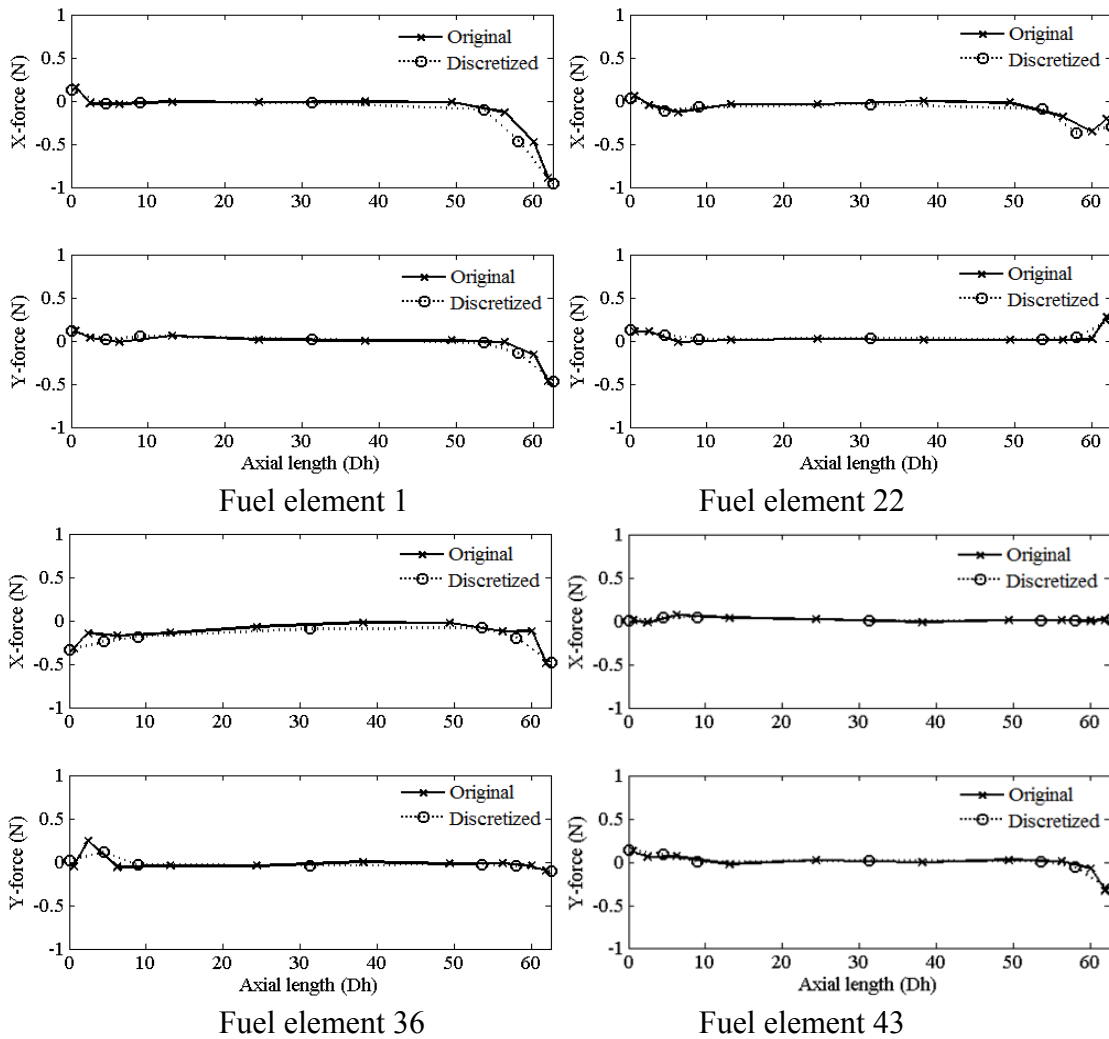


Figure 4.8 Discretized fluid forces on selected fuel elements.

### 4.3 Equations of Motion

#### 4.3.1 Equations of Motion

The system governing equation can be derived by extending Eq. (3.13) as

$$\mathbf{M}_{sys} \ddot{\mathbf{u}}(t) + \mathbf{C}_{sys} \dot{\mathbf{u}}(t) + \mathbf{K}_{sys} \mathbf{u}(t) = \mathbf{F}(t). \quad (4.24)$$

If the conventional finite element formulation is used,  $\mathbf{u}$  represents the nodal displacement vector  $\mathbf{u} = (u, v, w, \theta_x, \theta_y, \theta_z)^T$ .  $\mathbf{M}_{sys} = \mathbf{M}_s + \mathbf{M}_f$  and  $\mathbf{K}_{sys} = \mathbf{K}_s + \mathbf{K}_f$  are the system mass and stiffness matrices respectively.  $\mathbf{M}_s$  is the structural mass matrix corresponding to the  $\mathbf{M}$  matrix in Eq. (3.13),  $\mathbf{M}_f$  is the added mass matrix assembled from  $\mathbf{M}_e^a$ .  $\mathbf{K}_s$  is the structural stiffness matrix corresponding to the  $\mathbf{K}$  matrix in Eq. (3.13).  $\mathbf{K}_f$  is the global added stiffness matrix assembled from  $\mathbf{K}_e^a$ . This term is negligible compared to  $\mathbf{K}_s$  in the current application.  $\mathbf{C}_{sys} = \mathbf{C}_i + \mathbf{C}_v$  is the system damping matrix.  $\mathbf{C}_i$  is the damping matrix assembled from  $\mathbf{C}_e^i$ , representing the damping effect introduced by the inviscid force.  $\mathbf{C}_v$  is the damping matrix assembled from  $\mathbf{C}_e^v$ , representing the viscous damping. Boundary conditions have been applied to the above matrices using the penalty method by replacing the diagonal entries in the system stiffness matrix by a large number.

#### 4.3.2 Modal Analysis

The system equations can be converted to phase space by modal analysis. Suppose  $\boldsymbol{\varphi}_i$  ( $i=1, \dots, N$ ) is the modal vectors obtained by solving the free vibration problem

$$\mathbf{M}_{sys} \ddot{\mathbf{u}} + \mathbf{K}_{sys} \mathbf{u} = \mathbf{0}. \quad (4.25)$$

The displacement vector can be expressed as the linear combination of the modal vectors

$$\mathbf{u} = \sum_{i=1}^N \boldsymbol{\varphi}_i \eta_i = \boldsymbol{\Phi} \boldsymbol{\eta}. \quad (4.26)$$

where  $\boldsymbol{\Phi} = [\boldsymbol{\varphi}_1 \ \boldsymbol{\varphi}_2 \ \dots \ \boldsymbol{\varphi}_N]$ ,  $\boldsymbol{\eta} = (\eta_1, \dots, \eta_{N_m})$ .

The system equation Eq. (4.24) can be transformed to the phase space by substituting Eq. (4.26) into Eq. (4.24) and pre-multiply with  $\Phi^T$

$$\begin{aligned} [\Phi^T \mathbf{M}_{sys} \Phi] \ddot{\eta} + [\Phi^T \mathbf{C}_{sys} \Phi] \dot{\eta} + [\Phi^T \mathbf{K}_{sys} \Phi] \eta &= \Phi^T \mathbf{F}; \text{ or} \\ \widehat{\mathbf{M}} \ddot{\eta} + \widehat{\mathbf{C}} \dot{\eta} + \widehat{\mathbf{K}} \eta &= \mathbf{Q}. \end{aligned} \quad (4.27)$$

where  $\widehat{\mathbf{M}} = \Phi^T \mathbf{M}_{sys} \Phi$  is the modal mass matrix;  $\widehat{\mathbf{K}} = \Phi^T \mathbf{K}_{sys} \Phi$  is the modal stiffness matrix.

$\widehat{\mathbf{M}}$  and  $\widehat{\mathbf{K}}$  are diagonal due to the orthogonal property of the mode shapes  $\phi_i^T \phi_j = 0$  ( $i \neq j$ ).

Generally speaking  $\widehat{\mathbf{C}}$  is not diagonal, but numerical calculation shows that the off-diagonal elements are small. In a slightly damped system, a common approximation is to ignore the off-diagonal damping terms and keep the diagonal terms as the modal damping. With this approximation, the modal equations of motion can be decoupled into a set of independent single-DOF equations

$$m_i \ddot{\eta}_i(t) + c_i \dot{\eta}_i(t) + k_i \eta_i(t) = Q_i(t) \quad (i = 1, \dots, N_m), \quad (4.28)$$

where  $N_m$  is the total number of modes retained in a modal analysis.

## 4.4 Solution Methods for Decoupled Equations

Once the system equations of motion are transformed into the phase space, each uncoupled equation can be solved as a single-DOF system. The response of  $\eta_i(t)$  can be obtained using many approaches, such as the discrete convolution integral method (Meirovitch, 2001), the state transition matrix method (Meirovitch, 1997; Ogata, 2002), and the frequency domain solution using the system transfer function (Wirsching, *et al.*, 1995). The convolution integral and state transition matrix method produce deterministic time domain solution. The solution can be used to track the motion of material points at all solution time. The state transition matrix method is a recursive method and hence very efficient in solving a response with a very large number of time steps, on which the convolution integral method often fails. The drawback of this method is that the solution is influenced by the assumed initial conditions. The solution duration must be sufficiently long for the solution to converge. This is difficult because the flow simulation is very time consuming. The frequency domain solution is based on the system transfer function and the auto/cross spectral density of the excitation. The solution gives out statistical properties of the response as a stationary random process without any information about the location of a material point at a particular moment. The state transition matrix method and the transfer function method may be combined to obtain a full understanding of the bundle response.

### 4.4.1 Response in Time Domain

If  $F(t)$  is regarded as a function with deterministic values, Eq. (4.28) can be solved using the state transition matrix method. First rewrite the Eq. (4.28) by dividing  $m_i$  at both sides

$$\ddot{\eta}_i(t) + 2\zeta_i\omega_i\dot{\eta}_i(t) + \omega_i^2\eta_i(t) = m_i^{-1}Q_i(t), \quad (4.29)$$

where  $\omega_i = \sqrt{k_i/m_i}$  is the natural frequency of the  $i$ -th mode;  $\zeta_i = c_i/(2m_i\omega_i)$  is the modal damping factor. Denoting the state variables  $a_i(t) = \eta_i(t)$  and  $b_i(t) = \dot{\eta}_i(t)$ , Eq. (4.28) can be transformed into the state domain

$$\begin{aligned} \dot{a}_i(t) &= b_i(t); \\ \dot{b}_i(t) &= -\omega_i^2 a_i(t) - 2\zeta_i\omega_i b_i(t) + m_i^{-1}Q_i(t). \end{aligned} \quad (4.30)$$

The above equation can be written in a matrix form

$$\dot{\mathbf{y}}_i(t) = \mathbf{B}_i \mathbf{y}_i(t) + \mathbf{b}_i Q_i(t), \quad (4.31)$$

where

$$\mathbf{y}_i(t) = \begin{Bmatrix} a_i(t) \\ b_i(t) \end{Bmatrix}; \quad \mathbf{B}_i = \begin{bmatrix} 0 & 1 \\ -\omega_i^2 & -2\zeta_i \omega_i \end{bmatrix}; \quad \mathbf{b}_i = \begin{bmatrix} 0 \\ m_i^{-1} \end{bmatrix}.$$

The solution of  $\mathbf{y}_i(t)$  can be expressed as (Meirovitch, 1997; Ogata, 2002)

$$\mathbf{y}_i(t) = \mathbf{\Psi}_i(t) \mathbf{y}_i(0) + \int_0^t \mathbf{\Psi}_i(t-\tau) \mathbf{b}_i Q_i(\tau) d\tau; \quad (4.32)$$

$$\mathbf{\Psi}_i(t) = \mathbf{I} + \sum_{k=1}^{\infty} \frac{t^k}{k!} \mathbf{B}_i^k, \quad (4.33)$$

where  $\mathbf{I}$  is the identity matrix.  $\mathbf{y}_i(0) = \mathbf{\Phi} \mathbf{x}(0)$  is the initial conditions of the  $i$ -th mode.  $\mathbf{\Psi}_i$  is known as the state transition matrix.  $\mathbf{\Psi}_i$  converges quickly with number of terms  $k$ . It has been found  $k=5$  is sufficient for an accurate solution.

For a discrete time series of  $\mathbf{y}_i(t)$  uniformly sampled with a time step  $\Delta t$ , Eq. (4.32) can be evaluated recursively (Meirovitch, 1997)

$$\mathbf{y}_i(n+1) = \mathbf{\Psi}_i(\Delta t) \mathbf{y}_i(n) + \mathbf{A}_i^{-1} [\mathbf{\Psi}_i(\Delta t) - \mathbf{I}] \mathbf{b}_i Q_i(n), \quad (4.34)$$

where  $n$  is an integer representing the index of the time step. Once the solution of  $\mathbf{y}_i(t)$  is obtained, the system response can be calculated using Eq. (4.26).

The time domain solution includes the influence of the assumed initial conditions, so the solution must be long enough for the response due to the initial conditions to be damped out. Then the true steady state solution can be obtained. Spectral information, such as PSD, of the response can be calculated in post-processing steps.

#### 4.4.2 Response in Frequency Domain

An alternate approach to directly obtain the spectral information of the steady state response is to utilize the system transfer function in the frequency domain. Rewrite Eq. (4.35) as

$$\ddot{\eta}_i(t) + 2\zeta\omega_n\dot{\eta}_i(t) + \omega_n^2\eta_i(t) = P_i(t) . \quad (4.35)$$

where  $P_i(t) = m_i^{-1}Q_i(t)$  is the normalized modal force. If  $P_i(t)$  is regarded as an ergodic random process, the response  $\eta_i(t)$  is also an ergodic random process. Generally, the modal force for two different modes may be correlated, so the cross spectral density between these modes may not be zero. Denote the spectral density matrix of the normalized modal force as  $\mathbf{S}_P$

$$\mathbf{S}_P(\omega) = \begin{bmatrix} S_{11}^P(\omega) & \cdots & S_{1M}^P(\omega) \\ \vdots & \ddots & \vdots \\ S_{M1}^P(\omega) & \cdots & S_{MM}^P(\omega) \end{bmatrix} . \quad (4.36)$$

where  $S_{ij}^P$  represents the cross spectral density of the modal forces between the  $i$ -th mode and the  $j$ -th mode

$$S_{ij}^P = \int_{-\infty}^{\infty} R_{ij}(\tau) e^{-i\omega\tau} d\tau , \quad (4.37)$$

where  $R_{ij}(\tau) = E[P_i(t)P_j(t+\tau)]$  is the crosscorrelation function between  $P_i(t)$  and  $P_j(t)$ . For an ergodic process, the value of the crosscorrelation function can be estimated on a discrete base

$$R_{ij}(l\Delta t) = \frac{1}{K} \sum_{k=1}^K P_i(k\Delta t)P_j(k\Delta t + l\Delta t) . \quad (4.38)$$

The modal response spectral density matrix is then

$$\mathbf{S}_\eta(\omega) = \text{conj}[\mathbf{G}(\omega)]\mathbf{S}_P(\omega)\mathbf{G}(\omega) , \quad (4.39)$$

where  $\mathbf{G}(\omega)$  is the system transfer function matrix and  $\text{conj}[\mathbf{G}(\omega)]$  is the complex conjugate of  $\mathbf{G}(\omega)$ .

$$\mathbf{G}(\omega) = \begin{bmatrix} G_1(\omega) & & \\ & \ddots & \\ & & G_{N_m}(\omega) \end{bmatrix} ; \quad (4.40)$$

$$G_i(\omega) = \frac{1}{\omega_i^2 - \omega^2 + i2\zeta_i\omega_i\omega}. \quad (4.41)$$

The system response spectral density matrix can then be calculated as

$$\mathbf{S}_u(\omega) = \mathbf{\Phi} \mathbf{S}_\eta(\omega) \mathbf{\Phi}^T. \quad (4.42)$$

## 4.5 Numerical Results

### 4.5.1 Modal Excitations

The modal excitation spectral density represents the joint acceptance between the fluid excitation pattern and the structural mode shape. Only those modes can be excited that the joint acceptance between the two are not zero. Figure 4.9 shows a comparison between the first 100 modes. The horizontal axis is the frequency in Hz, and the vertical axis is the value of the standard deviation of the normalized modal force. Each data point represents a mode. It can be seen that the lowest two modes and some higher frequency modes are excited. Considering Eq. (4.42), the variance of the modal response can be obtained

$$\sigma_{\eta_i}^2 = \int_{-\infty}^{\infty} S_{\eta_i}(\omega) d\omega = \int_{-\infty}^{\infty} |G_i(\omega)|^2 S_{ii}^P(\omega) d\omega = \int_{-\infty}^{\infty} \frac{S_{ii}^P(\omega)}{(\omega_i^2 - \omega^2)^2 + (2\zeta_i \omega_i \omega)^2} d\omega, \quad (4.43)$$

where  $S_{\eta_i}(\omega)$  is the power spectral density of  $\eta_i$ . Variance of the modal response decreases quickly with the increase of the natural frequency. Therefore, only low frequency responses are prominent. As far as damping, it is small for all modes except the lowest one. Table 4.1 gives the damping factor obtained using the approach described in Section 4.2.

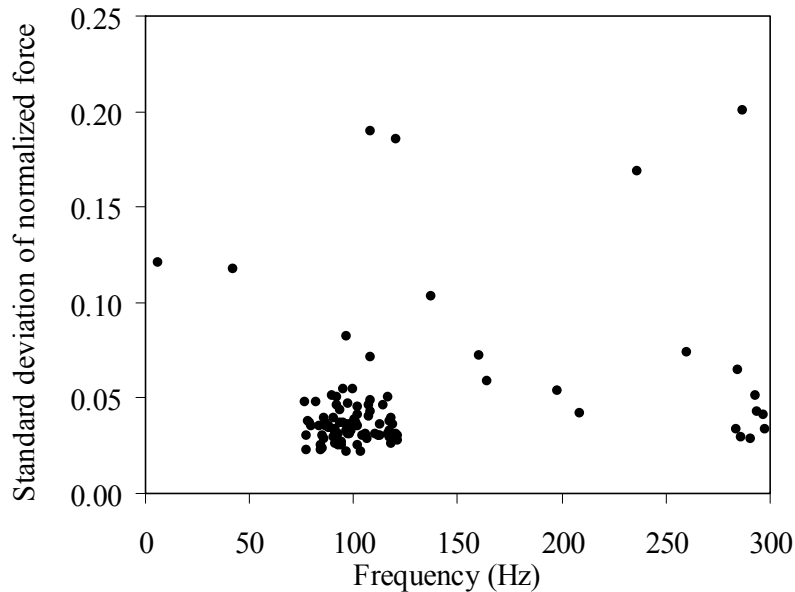


Figure 4.9 Comparison of normalized modal forces between different modes.

Table 4.1 Damping factor for the first 20 modes.

	$\zeta$		$\zeta$
1	0.02294	11	0.00178
2	0.00345	12	0.00178
3	0.00195	13	0.00177
4	0.00194	14	0.00176
5	0.00193	15	0.00174
6	0.00192	16	0.00174
7	0.00191	17	0.00174
8	0.00188	18	0.00172
9	0.00182	19	0.00165
10	0.00179	20	0.00169

#### 4.5.2 Solution in Time Domain

The solution is solved using the state transition matrix for 0.5 seconds. To compare with experimental data, the relative displacement between the transducer head and the target fuel element (R7) needs to be calculated. The location of the transducer is illustrated in Figure 4.10. The thick solid line represents the target steel plate mounted on R7. The initial gap is 0.1 mm.

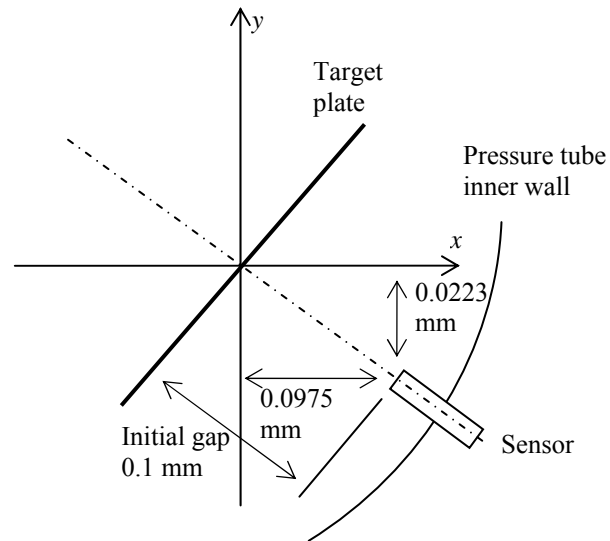


Figure 4.10 Illustration on the sensor location.

A monitored node is set in the numerical models. The monitored node locates on fuel element R7 at an axial location  $Z=36$  mm measured from the upstream endplate towards downstream. This location is pointed by the displacement transducer. The response at the monitored node is shown in Figure 4.11.

As a comparison to the experiments, the measured relative displacement between the transducer and fuel element R7 is shown in Figure 4.12. The measured signal varies from -0.055 mm to 0.055 mm with a fluctuation range of 0.11 mm. The simulation shows a similar range from -0.054 mm to 0.060 mm.

Figure 4.13 shows the power spectral density of the numerical results and the measurement result. Note that the measurement device was powered by alternating current with a frequency of 60 Hz, so the recorded signal contains noises at the harmonics of 60 Hz. The sharp spikes at 60, 120, 180 and 360 Hz in the measured power spectral density introduced by the electric noises have been removed by applying band filters. Comparison shows that the simulation result matches with measurement. The spikes around 45 Hz and 230 Hz appear in both simulation result and experimental measurement. The spike around 120 Hz in the simulation result is however not very clear in the measured record. This may be caused by the sensor location being too close to the node of the 1st beam bending mode of a fuel element.

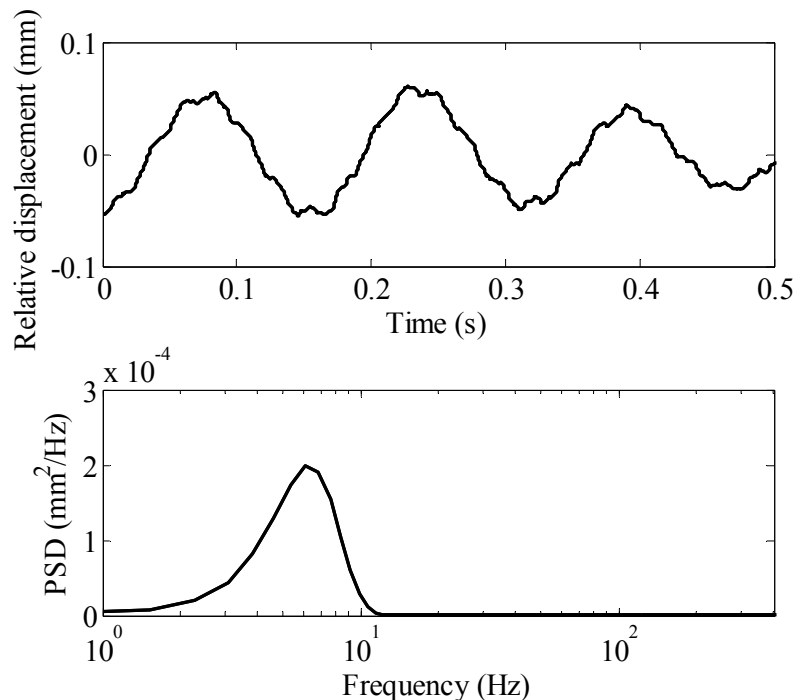


Figure 4.11 Time history and power spectral density of the relative displacement between the sensor and the monitored fuel element obtained in simulation for 0.5 s record.

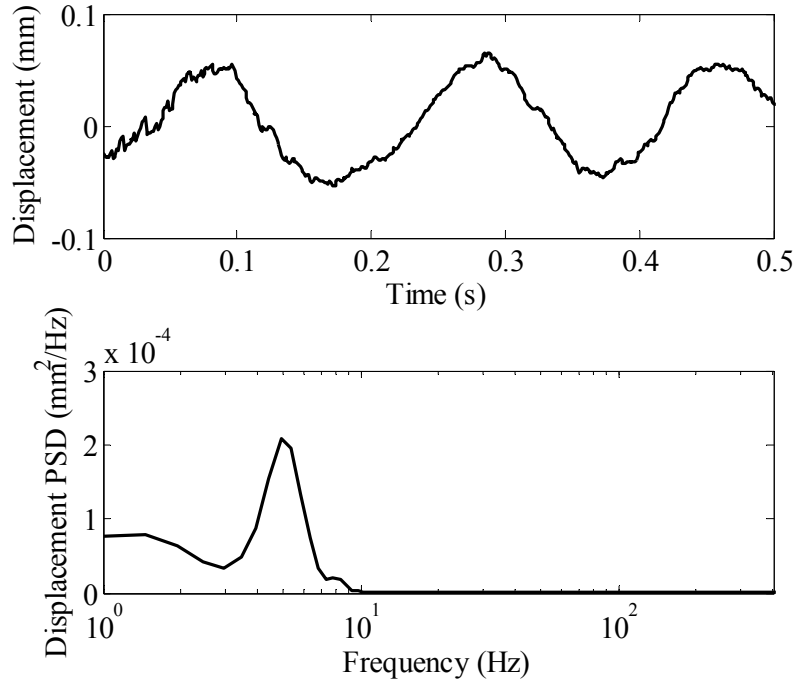


Figure 4.12 Time history and power spectral density of the relative displacement between the sensor and the monitored fuel element obtained in experiment for 0.5 s record.

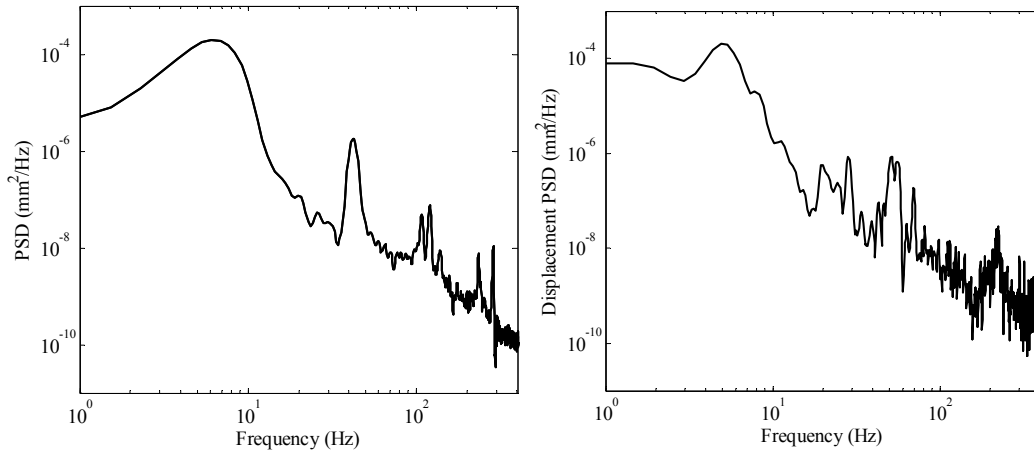


Figure 4.13 Comparison of power spectral densities of the relative displacement obtained in simulation (left) and experiment (right) in logarithmic scale.

The power spectral density of the noise of the transducer  $S_0$  can be estimated based on the resolution/repeatability of the sensor. It can be regarded as a low-pass noise process with the range of  $[-2, 2]$   $\mu\text{m}$ . Suppose the probability distribution of the error is subjected

to the normal distribution. It can be approximately regarded that 99.7% of the values are less than  $2 \mu\text{m}$  and greater than  $-2 \mu\text{m}$ . This means that  $3\sigma=2 \mu\text{m}$ , and  $\sigma=2/3 \mu\text{m}$ , where  $\sigma$  is the standard deviation of the error. The cut-off frequency of the transducer is 800 Hz, so  $\omega_{cut-off}=2\pi \times 800 \text{ rad/s}$ . According to the relationship  $\sigma^2 = S_0 \omega_{cut-off}$  (Newland, 1975), one obtains  $S_0 = \sigma^2 / \omega_c = 7.16 \times 10^{-11} \text{ mm}^2/\text{Hz}$ . This calculation shows that all the spikes in the measurement in Figure 4.13 are real vibration signals.

Figure 4.14 shows the phase plot of the  $x$ -displacement and  $y$ -displacement simulation result. The plots show that the motion is basically periodic but experiences randomness.

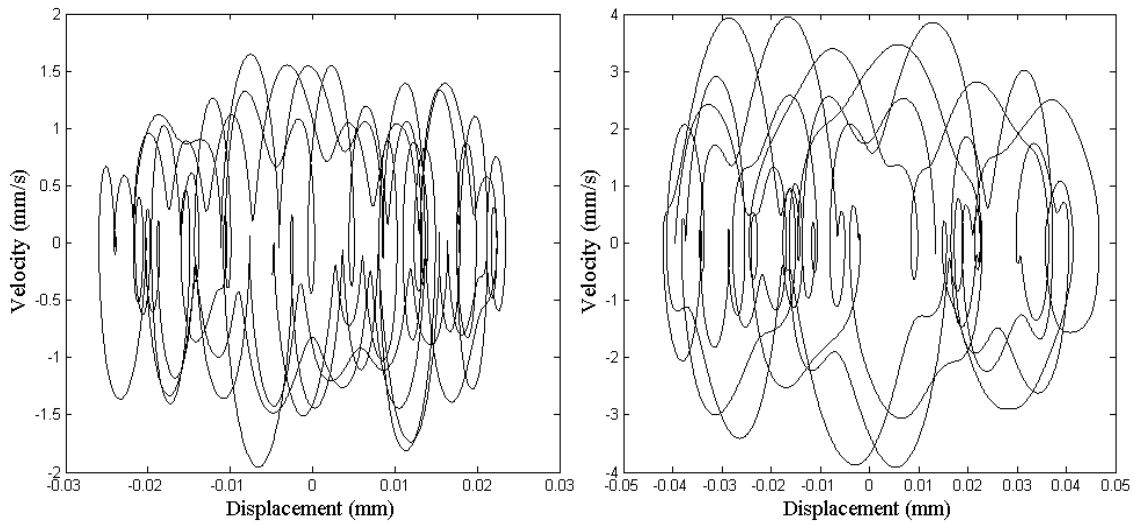


Figure 4.14 Phase plot of the  $x$ - (left) and  $y$ - (right) displacement of the monitored node.

### 4.5.3 Solution in Frequency Domain

The bundle vibration is solved using the system transfer function for a steady state solution. Figure 4.15 shows the power spectral densities for the  $x$ - and  $y$ -displacement of the monitored node obtained from simulation. It is difficult to calculate the power spectral density from simulation for the relative displacement between the sensor and fuel element R7, because the displacement is a nonlinear function of  $x$ - and  $y$ -displacement of the monitored node. However, the predicted  $x$ - and  $y$ -displacement show similar frequency distribution compared to the measured relative displacement shown in Figure 4.13.

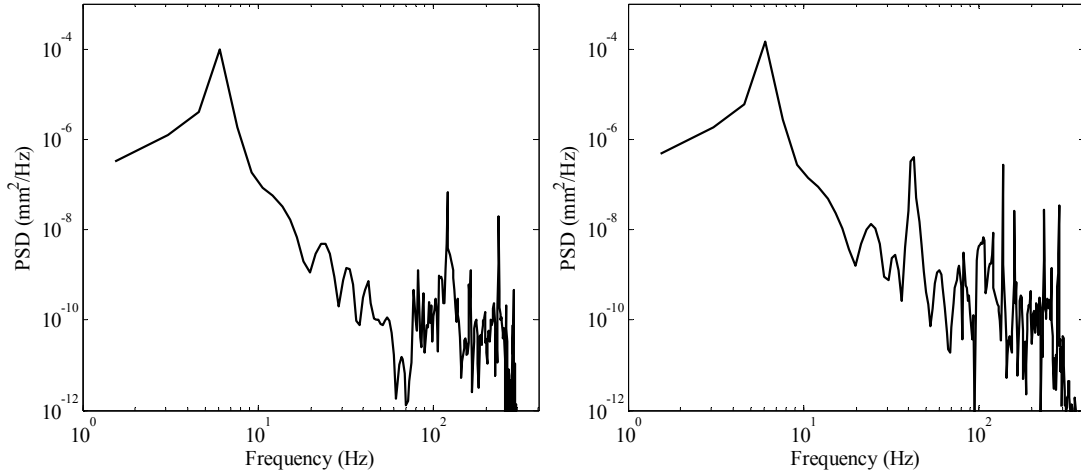


Figure 4.15 Power spectral densities for  $x$ -displacement (left) and  $y$ -displacement (right) of the monitored node obtained from the random vibration solution.

A more direct comparison can be done by plotting the standard deviation of the  $x$ - and  $y$ -displacement  $\sigma_x$ ,  $\sigma_y$ , and the relative displacement. The square value of the standard deviation (or the variance) can be calculated by integrating the power spectral density function. The standard deviations are shown in Figure 4.16. The calculated values of  $\sigma_x$  and  $\sigma_y$  are 0.0126 mm and 0.0156 mm, respectively. In comparison, the standard deviation of the relative displacement between the sensor and the target fuel element is  $\sigma_r = 0.0267$  mm. Figure 4.16 shows the range of  $\sigma_x$  and  $\sigma_y$  with dash-line boxes. The range of  $\sigma_r$  is shown as solid-line circle. The simulation prediction is smaller than the measured data. The trajectory obtained from the time domain solution is also shown in the figure.

To understand how the bundle moves, the standard deviation of all nodes at the midplane is plotted in Figure 4.17. The circles represent the initial positions of the nodes. The horizontal bars represent the standard deviation in the  $x$ -direction and the vertical bars represent the standard deviation in the  $y$ -direction. This figure clearly shows that the bundle undergoes a rocking or swing motion with large  $x$ -displacement on the top and large  $y$ -displacement on the side.

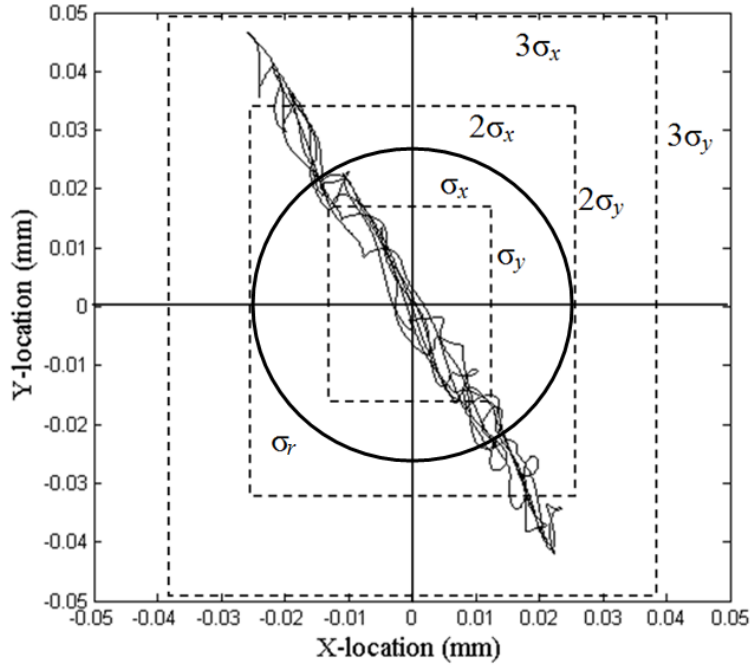


Figure 4.16 Motion range of the monitored node with trajectory.

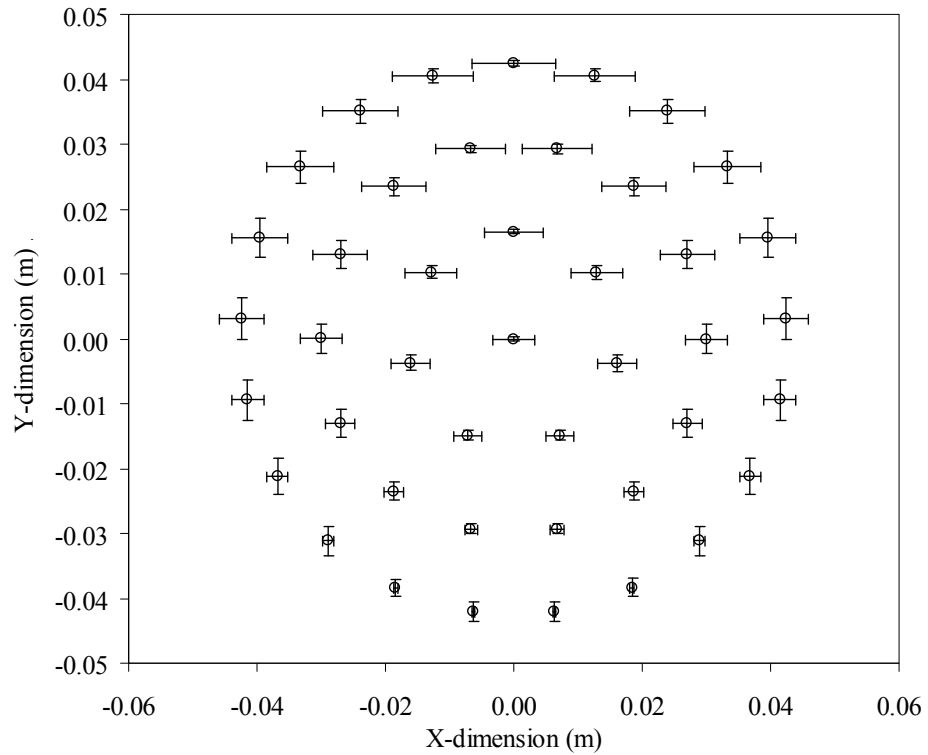


Figure 4.17 Scaled (200x) standard deviation of  $x$ - and  $y$ -displacement on selected fuel elements at the midplane.

#### 4.5.4 *Computer Code Efficiency*

A computer code has been written to calculate the flow-induced vibration of the inlet bundle using FORTRAN 90 language. The code was developed on an IBM-PC and compiled using G95<sup>‡</sup> FORTRAN compiler. The code contains a number of subprograms to provide the following functionalities: bundle geometry generation; finite element discretization; solutions for static deformation under gravity; free vibration modal solutions; time domain solutions for both formulations; and frequency domain solution.

The accuracy of the code has been validated against mature commercial and non-commercial finite element packages in the previous chapter. The efficiency of the code can be demonstrated using one example. Considering the deterministic transient solution for 6400 time steps with 100 modes retained in the modal analysis, the total time used on a 1.66 GHz computer is 19.0 minutes. Under the same condition, a frequency domain analysis that calculates the standard deviation and power spectral densities for all degrees of freedoms takes 19.5 minutes. The total number of degrees of freedom in the model, after substructuring and condensation, is 1806. In a transient solution, the computing time is largely proportional to the number of time steps; however, in a frequency domain solution, the computational effort is related to the number of points used to represent the frequency axis and the square of number of modes retained in the solution.

---

<sup>‡</sup> G95 is a free FORTRAN compiler developed by Andy Vaught ([www.g95.org](http://www.g95.org)).

## 4.6 Summary of the Chapter

This chapter presented models for the flow-induced vibration of the inlet fuel bundle. Fluid added mass, add stiffness and damping terms are incorporated into the finite element models established in the previous chapter. The equations of motion were decoupled using the modal analysis with approximations made on the damping terms. The uncoupled governing equations were solved both in time domain and in frequency domain. The numerical solutions were compared to experimental results. The predicted bundle vibration was close to that from experimental measurement. The energy distribution in the response frequency spectral matched that of the measurement.

## CHAPTER 5 CONCLUSIONS AND FUTURE WORK

### 5.1 Conclusions

Fretting wear of the pressure tube is a long-term integrity concern for CANDU nuclear reactors, because fretting reduces the service life of pressure tubes and leads to unplanned shut downs and costly replacement of core components. Sever fretting damage can be induced by acoustic resonance in a short period of time, but this type of damage can be avoided by adjusting the excitation frequencies and fuel channel acoustic natural frequencies. Flow-induced vibration of the fuel bundles is a more persistent contribution to pressure tube fretting and is an inevitable phenomenon in the fuel channels.

Flow-induced vibration of a structure can be induced by three major mechanisms: fluid-elastic instability, turbulence, and vortex shedding. Fluid-elastic instability of beams in a parallel flow was regarded as an important mechanism in the vibration of fuel element clusters in the past, but it has been proved not to be the case in the CANDU fuel bundles. The flow velocity is sub-critical in a fuel bundle and no instability occurs. Fuel element vibration due to turbulence buffeting has also been studied for the fully developed parallel flow in a fuel bundle and no significant result was obtained. All vibration models based on idealized parallel flows fail to capture the high level of vibration experienced by the fuel bundles.

To reveal the mechanism of fuel bundle vibration, the three-dimensional turbulent flow entering and passing through one and a half bundle is modeled in this research. The model includes the endplates on the upstream end of the inlet bundle and on the interface between the two bundles. A portion of upstream flow is also included to properly address the transition between a pipe flow and the bundles flow. Large eddy simulation is used to model the turbulence. Simulation results show that vortices forms after the endplate ribs and rings, especially after the juncture area of the inner ring and ribs between the inner ring and the intermediate ring. Blockage of the flow at these locations led to two consequences: i ) a swirling flow was generated in the subchannels between the inner ring and the intermediate ring; ii) large three-dimensional vortices were generated. The swirling flow is characterized with a preferred direction, which induces a net moment

about the bundle axis. The fluctuation of the velocity causes this moment to fluctuate. This swirling flow is found to be strong in terms of tangential velocity magnitude near the upstream endplate of the inlet bundle and decaying towards the downstream before disappearing after half of the bundle length. The vortices are transported down stream and the washing down of these vortices causes pressure fluctuation on the fuel element surfaces. This pressure fluctuation is much more significant than that created by turbulence.

The fluid force distribution on the inlet fuel bundle is obtained through numerical simulation. The fluid force is used as the excitation for fuel bundle response prediction. A fuel bundle vibration model based on the finite element method is developed. Weak coupling is assumed based on the fact of small amplitude vibration. The added mass and fluid damping terms are approximated by the slender body theory of parallel flow. Added stiffness terms due to parallel flow are included to investigate the influence of fluid-elasticity. Numerical solution shows that these added stiffness terms are trivial compared to the stiffness of the structure and confirms that no instability happens in a fuel bundle. However, it can be seen that some of the added stiffness terms bear negative diagonal values and may undermine the system stiffness if the flow velocity is sufficiently large.

Free vibration simulation shows that the fuel bundle bears complicated modes, but the fundamental mode is a rocking-like motion, and the second mode is a motion in which the bundle moved up and down as that happens on a mass-spring system. Higher modes include mode groups corresponding to the bending modes of the fuel elements.

Fuel bundle vibration simulation shows that significant joint acceptance exists for the 1st and the 2nd mode as well as some higher modes around 120 - 140 Hz, 230 Hz and 280 Hz. In the predicted response, vibration energy concentrates near these modes in the spectra. A similar energy distribution also exists in the measured spectra.

## 5.2 List of Contributions

The main contributions of the research reported in this thesis were:

- Developed a dynamic model of a 43-element simulated CANDU fuel bundle for the first time.
- Predicted the response of a simulated fuel bundle at the inlet of a bundle string subjected to the turbulent bundle flow in the normal operating condition and compared the simulation results to experiment measurements.
- Developed an accurate and efficient endplate model using the 3rd-order thick plate theory.
- Characterized the flow regions in the fuel channel for the first time, which is useful for guiding future studies in the field.
- Developed a computational model for the turbulent bundle flow that covers one and a half fuel bundles using large eddy simulation.
- Flow passing through the interface between fuel bundles was modeled for the first time.
- Revealed the excitation mechanism of the fuel bundle vibration using the computational fluid model. Local cross-flow induced by the endplates was found to be the main source of excitation.
- Obtained the fluid force distribution on a fuel bundle for the first time.

## 5.3 Future Work

### 5.3.1 Limitations in the Current Work

As any research, the present work is not perfect and bears limitations in some aspects.

Firstly, weak coupling between the fluid solution and the structural response is used. This approach has indeed been proven to be reasonable; however, the fluid-solid interaction forces used in the vibration model are based on the theory developed for the vibration of slender bodies in a parallel flow. This omits the interaction forces on the endplate ribs and rings produced in the cross flow passing over these components. To solve the interaction force on the endplates, the fluid field must be updated from time to time with moving solid-fluid boundaries. This is a very time-consuming task for a fluid model that contains millions of grids.

Secondly, the boundary conditions for the fuel bundle are assumed to be simply supported at the bearing pads near the bottom of the bundle. This boundary condition is not real since the bearing pads can slide and leave the supporting tube. Although the weight of the bundle and the friction between the bearing pads and the tube prevent the above motions from occurring, it is difficult to predict when these conditions are violated. The current boundary condition is more stringent than the real boundary conditions and may lead to smaller amplitude of the response. The real boundary conditions may be modeled as frictional contact which introduces nonlinearity.

Thirdly, the flow experiment is limited to the wall pressure measurement on the tube wall. The pressure fluctuations inside the bundle subchannels are of more interest because they are a direct reflect of the convection of the large vortices generated after the endplate ribs and rings. Unfortunately, the pressure transducers currently available on the market are either too big in size or too low in sensitivity. Velocity measurement in the subchannels is also difficult to conduct due to the limited space. This requires specialized velocimetry and customized fuel elements.

Finally, spacer pads are installed in a real CANDU fuel bundle but omitted in the experimental bundle and the numerical models. The spacer pad blocks the subchannel

flow and introduces swirls due to its inclined orientation with respect to the bulk flow in the subchannels. These spacer pads may be significant sources of unsteady fluid forces.

### *5.3.2 Suggestions for Future Work*

There are some suggestions for future studies on the fuel bundle vibration problem.

First, the real fluid-solid interaction may be solved without dramatically increasing the computational effort. The fluid field and the bundle vibration can be solved in an alternate manner. In each time step, the boundary conditions of the fluid field are determined from the previous structural solution. The fluid field is solved and then the pressure on the solid-fluid boundary is integrated to find the force. The force is fed to the structural model for bundle response. Due to the small amplitude of the bundle vibration, the change of the flow channel is negligible. This allows one to merely update the velocity of the fluid-solid boundary at the start of each time step without modifying the mesh. This avoids a major time-consuming process in fluid-solid interaction simulation.

Second, contact may be considered. Contact boundary condition involves the unknown contact force and the gap between a contact pair. They can be expressed in a complementary form. The equations of motion established using the finite element method can be further discretized in the time domain using a time marching method, such as the Newmark method or the Wilson-theta method. Solution of the dynamic contact problem is then converted to the sequential solutions of a quasi-static contact problem, which can be solved using Lemke's algorithm. Combination of the contact boundary condition in the flow-induced vibration of the fuel bundle is an important step towards the complete solution of the fuel bundle vibration problem, but attention must be paid at the efficiency of the computer code. It is recommended to reduce the scale of the problem with dynamic substructuring before the complementary equations are solved. Once contact forces are solved, the wear work rate can be estimated to predict the material removal rate.

Third, the endplate misalignment effect may be further investigated. The endplates between the inlet and the second bundle are perfectly aligned in the current fluid model; however, this is not always the case. The endplates can be misaligned with an arbitrary

angle. In some cases, the blockage of the flow is very significant and greatly alters the flow pattern within and after the endplate subchannels. The effect of the misalignment can be investigated by solving multiple models with each model defining a small increment on the misalignment angle from 0 to  $2\pi/7$  rad. The endplate outer ring and intermediate ring exhibit a periodicity of 7, and therefore only 1/7 of full circle needs to be studied. The inner ring webs are not important in terms of producing unbalanced forces, so they can be ignored.

Last, although the computational model is valid for out-reactor conditions, it can be easily extended to in-reactor conditions by considering heat flux at the fuel element surfaces and heat transfer in the coolant. FLUENT can be used to handle the thermal hydraulic solution. More work may be done on the structural finite element model to incorporate power generation and thermal stress.

**REFERENCES**

Abbasian, F., Yu, S.D., Cao, J. (2009). Experimental and numerical investigations of three-dimensional turbulent flow of water surrounding a CANDU simulation fuel bundle structure inside a channel. *Nuclear Engineering and Design*, 239(11): 2224-2235.

Anderson, J.D (1995). *Computational Fluid Dynamics – the Basics with Applications*. McGraw-Hill, New York, U.S..

Anselmet, F., Ternat, F., Amielh, M., Boiron, O., Boyer, P., Pietri, L. (2009). Axial development of the mean flow in the entrance region of turbulent pipe and duct flows. *Comptes rendus. Mecanique*, 337(8): 573-584.

Au-Yang, M.K., Jordan, K.B. (1980). Dynamic pressure inside a PWR - A study based on laboratory and field test data. *Nuclear Engineering and Design*, 58(1): 113-125.

Batchelor, G.K. (1967). *An Introduction to Fluid Dynamics*. Cambridge University Press. Cambridge, U.K..

Bathe, K.J. (1996). *Finite Element Procedure*, Prentice Hall, New Jersey, U.S..

Blevins, R.D. (1993). *Flow-Induced Vibration*, 2nd Edition. Krieger Publishing Company, F.L., U.S..

Bull, M.K. (1995). Wall-pressure fluctuations beneath turbulent boundary layers: some reflections on forty years of research. *Journal of Sound and Vibration*, 190(3): 299-315.

Chang, D., Tavoularis, S. (2005). Unsteady numerical simulations of turbulence and coherent structures in axial flow near a narrow gap. *Journal of Fluids Engineering*, 127(3): 458-466.

Chang, D., Tavoularis, S. (2007). Numerical Simulation of Turbulent Flow in a 37-rod Bundle. *Journal of Nuclear Engineering and Design*, 237(6): 575 - 590.

Chen, S.S., Wambsganss, M.W. (1972). Parallel-flow-induced vibration of fuel rods. *Nuclear Engineering and Design*, 18(2): 253-278.

## REFERENCES

- Chen, S.S. (1975). Vibration of nuclear fuel bundles. *Nuclear Engineering and Design*, 35(3): 399-422.
- Clinch, J.M. (1969). Measurements of the wall pressure field at the surface of a smooth-walled pipe containing turbulent water flow. *Journal of Sound and Vibration*, 9(3): 398-419.
- Cho, M.S., Sim, K.S., Suk, H.C. Chang, S.K. (2000). Static strength analysis of CANDU-6 reactor fuel bundle. *Nuclear Engineering and Design*, 200(3): 407-419.
- Curling, L.R., Paidoussis, M.P. (1992). Measurements and characterization of wall-pressure fluctuations on cylinders in a bundle in turbulent axial flow: part 1 and 2. *Journal of Sound and Vibration*, 157(3): 405-449.
- Currie, I.G. (1974). *Fundamental Mechanics of Fluids*, 2nd edition. McGraw-Hill Inc., New York, U.S..
- D'Arcy, D.F., Schenk, J.R. (1987). Axial velocity and turbulence measurements in adjacent subchannels of a 37-rod bundle. *Proceedings of 3rd International Symposium on Laser Anemometry*, Boston, U.S., pp. 277-282.
- Dennier, D., Manzer, A.M., Kohn, E. (1995). Characteristics of CANDU fuel bundles that caused pressure tube fretting at the bundle midplane. *Proceedings - Annual Conference*, Canadian Nuclear Association 2, pp. 19.
- Finnemore, E., Franzini, J. (2001). *Fluid Mechanics with Engineering Applications*, 10th edition. McGraw-Hill, New York, U.S..
- Germano, M. (1986). A proposal for a redefinition of the turbulent stress in the filtered Navier-Stokes equations. *Physics of Fluids*, 29, 2323-2324.
- Germano, M., Piomelli, U., Moin, P., Cabot, W.H. (1991). A dynamic subgrid-scale eddy viscosity model. *Physics of Fluids A*, 3(7): 1760-1765.

## REFERENCES

- Gorman, D. J. (1971). An analytical and experimental investigation of the vibration of cylindrical reactor fuel elements in two phases flow. *Nuclear Science and Engineering*, 44: 277-390.
- Hassan, Y.A., Barsamian, H.R. (1999). Turbulence simulation in tube bundle geometries using the dynamic subgrid-scale model. *Nuclear Technology*, 128(1): 58-74.
- Hoerner, S.F. (1965). *Fluid Dynamic Drag*, 2nd edition. Hoerner Fluid Dynamics, Brick Town, N.J., U.S..
- Hooper, J.D. (1980). Developed single phase turbulent flow through a square-pitch rod cluster. *Nuclear Engineering and Design*, 60(3): 365-79.
- Horhoianu, G., Ionescu, D.V. (2006). A finite element model for static strength analysis of CANDU fuel bundle. *Kerntechnik*, 71(4): 203-207.
- Johnson, K.L. (1985). *Contact Mechanics*. Cambridge University Press, London, U.K..
- Judah, J. (1992). Overview of fuel inspections at the Darlington nuclear generating station. *Annual International Conference - Canadian Nuclear Association*, pp. 3.1-22.
- Karamcheti, K. (1966). *Principles of Ideal Fluid Aerodynamics*. Wiley, New York, U.S.
- Kim, H.M, No, H.C (2004). Analysis of power spectrum density in the PWE fuel assembly using the 3-D LES turbulent model of Fluent 6. *Proceedings of the 12th International Conference on Nuclear Engineering*, Arlington, Virginia, U.S., pp. 295-303.
- Lee, K.B., Jang, H.C. (1997). A numerical prediction on the turbulent flow in closely spaced bare rod arrays by a nonlinear  $k$ - $\epsilon$  model. *Journal of Nuclear Engineering and Design*, 172(3): 351-357.
- Leonard, A. (1974). Energy cascade in large-eddy simulations of turbulent fluid flows. *Advances in Geophysics*, edited by Frankiel, F.N. and Munn, R.E.. Academic, New York, 18A, pp.237-249.
- Lighthill, M.J. (1960). Note on the swimming of slender fish. *Journal of Fluid Mechanics* 9: 305-317.

## REFERENCES

Lilly, D. K. (1992). A Proposed Modification of the Germano Subgrid-Scale Closure Model. *Physics of Fluids A*, 4(3): 633-635.

Lin W.H. (1987). Hydrodynamic Forces on Multiple Circular Cylinders Oscillating in a Viscous Incompressible Fluid. *Journal of Applied Mathematics and Mechanics/Zeitschrift fur angewandte Mathematik und Mechanik*, 67(10): 487-501.

Lindeburg, M.R., Baradar, M. (2001). *Seismic Design of Building Structures: A Professional's Introduction to Earthquake Forces and Design Details*, 8th edition. Professional Publications Inc., Belmont, CA, U.S..

Mayer, G., Pales, J., Hazi, G., (2007). Large eddy simulation of subchannels using the lattice Boltzmann method. *Annals of Nuclear Energy*, 34: 140-149.

Meirovitch, L. (1997). *Principles and Techniques of Vibrations*, Prentice-Hall, Upper Saddle River, N.J., U.S..

Meirovitch, L. (2001). *Fundamentals of Vibrations*, McGraw Hill, N.Y., U.S..

Mindlin, R.D. (1951). Influence of rotatory inertia and shear on flexural motions of isotropic, elastic plates, *Journal of Applied Mechanics*, 18: 31-38.

Misra, A., Pauls, R.E., Vijay, D.K., Teper, W., Lin, T.C., Strzelczyk, A., Liu, J., Hemraj, R. (1994). Acoustic modelling in support of fuel failure investigation in a CANDU nuclear generating station. American Society of Mechanical Engineers, Pressure Vessels and Piping Division (Publication) PVP 279: 99-118.

Newland, D. E. (1975). *An Introduction to Random Vibrations and Spectral Analysis*, Longman: London,UK.

Ni, C.C., Hansen, R.J. (1978). An experimental study of the flow-induced motions of a flexible cylinder in axial flow. *ASME Journal of Fluid Engineering*, 100: 389-394.

Norsworthy, A.G., Field, G.J., Meysner, A., Dalton, K., Crandell, A. (1994). Fuel bundle to pressure tube fretting in Bruce and Darlington reactors. *Proceedings-Annual Conference, Canadian Nuclear Association*, (2): 14.

## REFERENCES

- Norsworthy, A.G., Ditschun, A. (1995). Fuel bundle to pressure tube fretting in Bruce and Darlington. *Proceedings-Annual Conference, Canadian Nuclear Association*, (2): 16.
- Ogata, K. (2002). *Modern Control Engineering*. 4th Edition. Prentice-Hall, Inc. N.J., U.S..
- Oppenheim, A.V., Schaffer, R.W. (1975), *Digital Signal Processing*. Englewood Cliffs, N.J.: Prentice-Hall.
- Ortloff, C.R., Ives, J. (1969). On the dynamic motion of a thin flexible cylinder in a viscous stream. *Journal of Fluid Mechanics*, 38(4): 713-720.
- Paidoussis, M.P. (1966). Dynamics of flexible slender cylinders in axial flow. Part I and Part II. *Journal of Fluid Mechanics*, 26(4): 717-751.
- Paidoussis, M.P. (1973). Dynamics of cylindrical structures subjected to axial flow. *Journal of Sound and Vibration*, 29(3): 365-385.
- Paidoussis, M.P. (2004). *Fluid-structure interactions: slender structures and axial flow*, Volume 1 and Volume 2. Elsevier Academic Press, San Diego, U.S..
- Paidoussis, M.P., Chaubernard, J.P., Genadry M.R., El Barbir, K.N. (1983). Dynamics of a cluster of flexible interconnected cylinders. Part 2. In axial flow. *Journal of Applied Mechanics*, 50(2): 429-435.
- Paidoussis, M.P., Curling, L.R. (1985). An analytical model for vibration of clusters of flexible cylinders in turbulent axial flow. *Journal of Sound and Vibration*, 98(4): 493-517.
- Paidoussis, M.P., Suss, S. (1977). Stability of a cluster of flexible cylinders in bounded flow. *Journal of Applied Mechanics*, 44(3): 401-408.
- Patanka, S.V., Spalding, D.B. (1972). A calculation procedure for heat, mass and momentum transfer in three-dimensional parabolic flows. *International Journal of Heat and Mass Transfer*, 15(10): 1787-1806.
- Pettigrew, M.J. (1993). The vibration behavior of nuclear fuel under reactor conditions. *Nuclear Science and Engineering*, 114(3): 179-189.

- Pope, S.T. (2000). *Turbulent Flows*. Cambridge University Press, New York, U.S..
- Przemieniecki, J.S. (1968). *Theory of Matrix Structural Analysis*, McGraw-Hill, New York, U.S..
- Rakowski, J., Litewka, P. (2000). An efficient 3D curved beam finite element. *Computer Assisted Mechanics and Engineering Sciences*, 7(4): 707-716.
- Reddy, J.N. (1984). A simple higher-order theory for laminated composite plates. *Journal of Applied Mechanics*, 51(4): 745-752.
- Reddy, J.N. (1996). *Mechanics of Laminated Composite Plates - Theory and Analysis*, CRC Press, New York, U.S..
- Sagaut, P., 2006. *Large Eddy Simulation for Incompressible Flow*. Springer-Verlag Berlin Heidelberg, Germany.
- Schwab, A.L. and Meijaard, J.P. (2002). Small Vibrations Superimposed on a Prescribed Rigid Body Motion. *Multibody System Dynamics*, 8(1): 29-49.
- Smagorinsky, J. (1963). General Circulation Experiments with the Primitive Equations. *Monthly Weather Review*, 91(3): 99-164.
- Smith, B.A.W., Derken, D.D. (1998). Measurement of steady and unsteady hydrodynamic loads on a nuclear fuel bundle. *Journal of Fluids and Structures*, 12(4): 475-489.
- Tayal, M., Wong, B.J., Lau, J.H.K., Nicholson, A.M. (1992). Assessing the mechanical performance of a fuel bundle: beam code description. *Proceedings of Annual International Conference*, Canadian Nuclear Association, Toronto, Canada, pp. 3.37-63.
- Tennekes, H., Lumley, J.L. (1972). *A First Course in Turbulence*. The MIT Press. Massachusetts, U.S..
- Timoshenko, S.P., Goodier, J.N. (1970). *Theory of Elasticity*, 3rd, McGraw-Hill, New York, U.S..
- Timoshenko, S.P., Woinowsky-Krieger, S. (1959). *Theory of Plates and Shells*, McGraw-Hill, New York, U.S..

## REFERENCES

- Versteeg, H.K., Malalasekera, W. (1995). *An Introduction to Computational Fluid Dynamics – the Finite Volume Method*. Pearson Education Limited, Essex, England.
- Weaver, D.S., Ziada, S., Au-Yang, M.K., Chen, S.S, Pettigrew, M.J (2000). Flow-induced vibrations in power and process plant components: progress and prospects. *ASME Journal of Pressure Vessel Technology*, 122(3): 339-348.
- White, F.M. (2003). *Fluid Mechanics*, 5th edition, McGraw–Hill, New York, U.S..
- Wilmarth, W.W. (1975). Pressure fluctuations beneath turbulent boundary layers. *Annual Review of Fluid Mechanics*, 7: 13-38.
- Wilson, R.J., Jones, B.G. (1983). Turbulent pressure-velocity measurements in a fully developed concentric annular air flow. *Journal of Vibration, Acoustics, Stress, and Reliability in Design*, 105(3):345-354.
- Wirsching, P.H., Paez, T.L., Ortiz, K. (1995). *Random Vibrations: Theory and Practice*. John Wiley and Sons, Inc., N.Y., U.S..
- Xu, S., Yu, S. D., Tayal, M., & Xu, Z. (2005). Modeling contact among multiple CANDU fuel elements in a bundle, *Proc. of the 18th International Conference on Structural Mechanics in Reactor Technology*, Beijing, China, August 7-12, SMiRT18-C02-3.
- Yang, S.Y and Sin, H.C. (1995). Curvature-based beam elements for the analysis of Timoshenko and shear-deformable curved beams. *Journal of Sound and Vibration*, 187(4): 569-584.
- Yetisir, M., Fisher, N.J. (1997). Prediction of pressure tube fretting-wear damage due to fuel vibration. *Nuclear Engineering and Design*, 176(3): 261-271.
- Yu, S.D., Wen, D.C., (2007). An efficient plate finite element and its application to three-dimensional deformations of CANDU fuel endplate rings. *Nuclear Engineering and Design*, 237 (4): 342-352.

## REFERENCES

Zhang, X., Yu, S.D. (2008). Experimental studies of a simulation CANDU fuel bundle structure in confined axial flow. *Proceedings of FIV2008*, Prague, Czech.

Zhang, X., Yu, S.D. (2010a). A thick plate model for bending and twisting of CANDU fuel endplates. *Nuclear Engineering and Design*, 240, 1565-1570.

Zhang, X., Yu, S.D. (2010b). Theoretical and experimental investigations of oscillatory rolling motion of a rod bundle inside a tube. *Proceedings of 11th Pan-American Congress of Applied Mechanics*, Foz de Iguassu, PR, Brazil.

Zhu, Z.H., Meguid, S.A. (2004). Analysis of three-dimensional locking-free curved beam element. *International Journal of Computational Engineering Science*, 5(3): 535-556.

## APPENDIX

### Nine-Node Thick Plate Element

According to the third-order shear deformation plate theory developed by Reddy (1984), the displacements of a material point are related to the five field variables as follows

$$\begin{aligned}
 u_x &= u(x, y) + \left( z - \frac{4z^3}{3h^2} \right) \psi_x(x, y) - \frac{4z^3}{3h^2} \frac{\partial w(x, y)}{\partial x}; \\
 u_y &= v(x, y) + \left( z - \frac{4z^3}{3h^2} \right) \psi_y(x, y) - \frac{4z^3}{3h^2} \frac{\partial w(x, y)}{\partial y}; \\
 u_z &= w(x, y),
 \end{aligned} \tag{A.1}$$

where  $u$ ,  $v$  and  $w$  are the displacements of material points on the plate mid-plane in the three coordinate directions, respectively;  $\psi_x$  and  $\psi_y$  are transverse shear angles at the mid-plane.

The five non-zero strains can be expressed as

$$\begin{aligned}
 \varepsilon_{xx} &= \left[ \begin{array}{ccc} 1 & z - \frac{4z^3}{3h^2} & -\frac{4z^3}{3h^2} \end{array} \right] \left\{ \begin{array}{c} u_{,x} \\ \psi_{x,x} \\ w_{,xx} \end{array} \right\}; \\
 \varepsilon_{yy} &= \left[ \begin{array}{ccc} 1 & z - \frac{4z^3}{3h^2} & -\frac{4z^3}{3h^2} \end{array} \right] \left\{ \begin{array}{c} v_{,y} \\ \psi_{y,y} \\ w_{,yy} \end{array} \right\}; \\
 \gamma_{yz} &= \left[ \begin{array}{cc} 1 - \frac{4z^2}{h^2} & 1 - \frac{4z^2}{h^2} \end{array} \right] \left\{ \begin{array}{c} \psi_y \\ w_{,y} \end{array} \right\}; \\
 \gamma_{zx} &= \left[ \begin{array}{cc} 1 - \frac{4z^2}{h^2} & 1 - \frac{4z^2}{h^2} \end{array} \right] \left\{ \begin{array}{c} \psi_x \\ w_{,x} \end{array} \right\}; \\
 \gamma_{xy} &= \left[ \begin{array}{ccccc} 1 & 1 & z - \frac{4z^3}{3h^2} & z - \frac{4z^3}{3h^2} & -\frac{8z^3}{3h^2} \end{array} \right] \left\{ \begin{array}{c} u_{,y} \\ v_{,x} \\ \psi_{x,y} \\ \psi_{y,x} \\ w_{,xy} \end{array} \right\},
 \end{aligned} \tag{A.2}$$

where subscript “ $_{,\alpha}$ ” represents the first derivative with respect to  $\alpha$  ( $\alpha = x, y$ ); subscript “ $_{,\alpha\beta}$ ” represents the second derivative with respect to  $\alpha\beta$  ( $\alpha, \beta = x, y$ ). The simplified stress-strain relationships may be written as

$$\begin{Bmatrix} \sigma_{xx} \\ \sigma_{yy} \\ \sigma_{yz} \\ \sigma_{zx} \\ \sigma_{xy} \end{Bmatrix} = \begin{bmatrix} E^* & E^* \nu & 0 & 0 & 0 \\ E^* \nu & E^* & 0 & 0 & 0 \\ 0 & 0 & G & 0 & 0 \\ 0 & 0 & 0 & G & 0 \\ 0 & 0 & 0 & 0 & G \end{bmatrix} \begin{Bmatrix} \varepsilon_{xx} \\ \varepsilon_{yy} \\ \gamma_{yz} \\ \gamma_{zx} \\ \gamma_{xy} \end{Bmatrix} \text{ or } \{\sigma\} = [Q]\{\varepsilon\}, \quad (\text{A.3})$$

where  $E^* = E/(1-\nu^2)$  and  $G = E/[2(1+\nu)]$ , where  $E$  is Young’s modulus, and  $\nu$  is Poisson’s ratio.

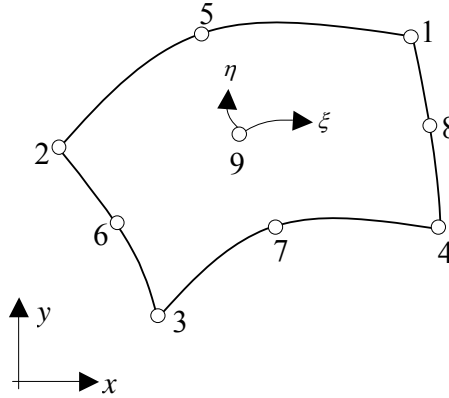


Figure A.1 Nine-node thick plate element.

As shown in Figure A.1, the isoperimetric thick plate element has nine nodes. Each node has five degrees of freedom including three translational and two rotational displacements. Within a plate finite element, all five field variables and the corresponding coordinates,  $x$  and  $y$ , are interpolated in terms of the following shape function in the following manner

$$g(x, y) = [N(\xi, \eta)]\{\bar{g}\}_e; \quad x = [N(\xi, \eta)]\{\bar{x}\}_e; \quad y = [N(\xi, \eta)]\{\bar{y}\}_e, \quad (\text{A.4})$$

where  $g$  represents one of the displacement field variables;  $\{\bar{g}\}_e^T = \{\bar{g}_1 \quad \bar{g}_2 \quad \dots \quad \bar{g}_9\}$  is the element nodal vector of variable  $g$ ;  $\{\bar{x}\}_e$  and  $\{\bar{y}\}_e$  are the nodal coordinate vectors; the

shape function matrix is  $[N] = [N_1(\xi, \eta) \ N_2(\xi, \eta) \ \cdots \ N_9(\xi, \eta)]$ ;  $N_k(\xi, \eta)$ ,  $k = 1, 2, \dots, 9$ , are identical to those for a two-dimensional nine-node Lagrangian element (Bathe, 1996).

Using the above equations the strain energy in an element can be expressed in terms of the nodal displacement vector  $\{\bar{q}\}_e = \{\bar{u}, \bar{v}, \bar{\psi}_x, \bar{\psi}_y, \bar{w}\}^T$

$$\begin{aligned} V_e &= \frac{1}{2} \int_A \int_{-h/2}^{h/2} \left( E^* \varepsilon_{xx}^2 + 2E^* \nu \varepsilon_{xx} \varepsilon_{yy} + E^* \varepsilon_{yy}^2 + G\gamma_{yz}^2 + G\gamma_{zx}^2 + G\gamma_{xy}^2 \right) dz dA \\ &= \frac{1}{2} \{\bar{q}\}_e^T [k]_e \{\bar{q}\}_e. \end{aligned} \quad (\text{A.5})$$

The element stiffness matrix  $[k]_e$  can be obtained from the following integral

$$[k]_e = \underbrace{\left[ \begin{array}{c} \vdots \\ \cdots \int_{-1}^1 \int_{-1}^1 [B]_i^T [K_z]_{ij} [B]_j |J_1| d\xi d\eta \cdots \\ \vdots \end{array} \right]}_{i, j=1,2,3,4,5}, \quad (\text{A.6})$$

where

$$[B]_1 = [B]_2 = \begin{bmatrix} N_{,x} \\ N_{,y} \end{bmatrix}, [B]_3 = [B]_4 = \begin{bmatrix} N \\ N_{,x} \\ N_{,y} \end{bmatrix}, [B]_5 = \begin{bmatrix} N_{,x} \\ N_{,y} \\ N_{,xx} \\ N_{,xy} \\ N_{,yy} \end{bmatrix} \quad \text{and} \quad [J]_1 = \begin{bmatrix} [N_{,\xi}] \{\bar{x}\}_e & [N_{,\xi}] \{\bar{y}\}_e \\ [N_{,\eta}] \{\bar{x}\}_e & [N_{,\eta}] \{\bar{y}\}_e \end{bmatrix}$$